Development of Magnetic Bond-Order Potentials for Mn and Fe-Mn

John F. Drain
St. Anne's College, University of Oxford

Supervisors:
Prof. D. G. Pettifor CBE FRS, Prof. R. Drautz

Thesis submitted for the degree of
Doctor of Philosophy
at the University of Oxford
Trinity Term, 2013

Abstract

While group VII $4d$ Tc and $5d$ Re have hexagonally close-packed (hcp) ground states, $3d$ Mn adopts the complex χ-phase which exhibits non-collinear magnetism. Density functional theory (DFT) calculations have shown that without magnetism the χ-phase remains the ground state of Mn implying that magnetism is not the critical factor, as is commonly believed, in driving the anomalous stability of the χ-phase over hcp. Using a tight-binding (TB) model it is found that while harder potentials stabilise close-packed hcp, a softer potential stabilises the more open χ-phase. By analogy with the structural trend from open to close-packed phases down the group IV elements, the anomalous stability of the χ-phase in Mn is shown to be due to $3d$ valent Mn lacking d states in the core which leads to an effectively softer atomic repulsion between the atoms than in $4d$ Tc and $5d$ Re.

Subsequently an analytic Bond-Order Potential (BOP) is developed to investigate the structural and magnetic properties of elemental Mn at 0 K. It is derived within BOP theory directly from a new short-ranged orthogonal d-valent TB model of Mn, the parameters of which are fitted to reproduce the DFT binding energy curves of the five experimentally observed phases of Mn, α, β, γ, δ, and ϵ-Mn. Not only does the BOP reproduce qualitatively DFT binding energy curves of the five different structure types, it also predicts the complex collinear antiferromagnetic (AFM) ordering in α-Mn, the ferrimagnetic (FiM) ordering in β-Mn and the AFM ordering in the other phases that are found by DFT. A BOP expansion including 14 moments is sufficiently converged to reproduce most of the properties of the TB model with the exception of the elastic shear constants which require further moments.

Magnetic analytic BOPs are also developed for Fe and Fe-Mn. The Fe model correctly reproduces trends in the structural stabilities of the common metallic structures except that AFM hcp is overstabilised. Reproduction of the elastic constants with a 9-moment BOP is reasonable although as is found for the Mn BOP the elastic shear constants require more moments to converge. Vacancy formation energies are close to those determined by experiment and DFT and the relative stabilities of self-interstitial atom (SIA) defects in ferromagnetic bcc Fe are correctly reproduced. The SIA formation energies are found to be better than those calculated with existing BOP models.

The Fe-Mn TB and BOP models were challenging to fit and nonmagnetic face-centred cubic (fcc) structures are overstabilised. Furthermore within BOP an incorrect magnetic solution is predicted for one fcc structure resulting in poor reproduction of the DFT stacking fault energies. Refitting the bond integrals might help to better reproduce the nonmagnetic hcp-fcc energy differences while an environment-dependent Stoner parameter could help provide the flexibility needed to correctly capture the magnetic energy differences.

Acknowledgements

First and foremost I would like to thank my supervisors David Pettifor and Ralf Drautz. Without their ideas, vision and dedication this project would not have happened. I am immensely grateful for the time and effort that they have invested in helping me over the past four years and, more recently, for reading and giving, as ever, insightful feedback on my work. I have learned so much from them during my time in Oxford and feel quite privileged to have had the chance to work with them.

I would also like to thank the members of the MML in Oxford including Michael Ford, Jan Gehrmann, Paul Kamenski, and Bernhard Seiser. Particular thanks must go to Michael, with whom I worked closely at various points of our respective projects, and Jan, whose emails were often a source of mirth and encouragement. Thanks also to Eunan McEniry, Georg Madsen and everyone in Ralf's group at ICAMS who were always so welcoming and generous during my visits to Bochum.

I would also like to extend my thanks to the many wonderful people who I have had the pleasure to get to know during my time in Oxford. St. Anne's College formed the bedrock of my life here and I feel indebted to the staff and students who have made these past four years arguably the most enjoyable and productive of my life. To name but a few my thanks must go to Chelsea and Keian, the Film Aesthetics Crew (Tara, Gavin, Kelse, Rachems and Becky), the PGCE and Dance With Me Colin crew (Clarkey, WBW, Quigsley, Joel, Champers, Meg), Will and Morag Murphey, Stephen Henry Hussy, George Taylor, John Halstead, and Jaya & Jem.

Furthermore I would like to thank Elle who has made the past three years so meaningful and enjoyable. I am grateful to have been able to share my time here with her and am thankful for her patience, her support and her love. She has been the person to have borne the brunt of my bad moods, my idiosyncrasies and my late nights and long days in the office, but who has brought the most happiness to my life during my time here.

Finally I would like to express my appreciation of and gratitude to my family, my father, my mother, my sister and my grandparents, without whom, in so many different ways, I would not have had the chance to do this DPhil. My parents, Grahame and Sandra, have always been incredibly supportive and encouraging of everything I have chosen to do in life even when, on occasion, my decisions may appear to run against their better judgement! I am particularly thankful for having been able to celebrate finishing this DPhil. with my grandmother, Sylvia.

Contents

1 Introduction **1**

2 Elemental Iron **7**
2.1 Introduction 7
2.2 Modelling Magnetism in Transition Metals 8
2.2.1 The Stoner Model of Magnetism 11
2.2.2 Extensions of the Stoner Model 14
2.3 Summary 16

3 Elemental Manganese **17**
3.1 Introduction 17
3.2 Allotropes of Manganese 18
3.2.1 α-Mn 18
3.2.2 β-Mn 22
3.2.3 γ-Mn 23
3.2.4 δ-Mn 23
3.2.5 ϵ-Mn 23
3.3 Tight-Binding Models for Manganese 24
3.4 Interatomic Potentials for Manganese 25
3.4.1 Introduction to Interatomic Potentials 25
3.4.2 Magnetic Interatomic Potentials 28
3.4.3 Existing Interatomic Potentials for Mn 29
3.5 Summary 29

4 Manganese-containing Steels **31**
4.1 Introduction to Steels 31
4.2 Mn-containing Steels 33
4.2.1 Transformation-Induced Plasticity (TRIP) and Twinning-Induced Plasticity (TWIP) 35
4.3 Binary Fe-Mn 44
4.3.1 Fe-Mn Phase Diagram 44
4.3.2 Modelling of Fe-Mn 44
4.4 Summary 49

5 Methodology **51**
5.1 Introduction . . . 51
5.2 Density Functional Theory (DFT) . . . 51
5.2.1 The Time-Independent Schrödinger Equation . . . 52
5.2.2 Born-Oppenheimer Approximation . . . 52
5.2.3 The Variational Principle . . . 53
5.2.4 The Hohenberg-Kohn Theorems . . . 53
5.2.5 The Kohn-Sham Equations . . . 54
5.2.6 Spin-Density Functional Theory . . . 55
5.2.7 Exchange Correlation Functionals . . . 56
5.2.8 Computational Details . . . 56
5.3 The Tight-Binding (TB) Approximation . . . 57
5.3.1 Derivation of nonmagnetic TB Binding Energy . . . 57
5.3.2 Derivation of Magnetic TB Binding Energy . . . 66
5.3.3 Computational Details . . . 68
5.4 Bond-Order Potentials (BOP) . . . 68
5.4.1 Introduction . . . 68
5.4.2 Moments Theorem . . . 70
5.4.3 The Recursion Method . . . 71
5.4.4 Atom-Based Analytic BOP . . . 76
5.4.5 Extensions of Analytic BOP . . . 79
5.4.6 Computational Details . . . 84
5.5 Summary . . . 85

6 Origin of the Ground State Structural Trend from χ to hcp down Group VII **87**
6.1 Introduction . . . 87
6.2 Electronic Structure and Internal Coordinates . . . 88
6.2.1 Electronic Structure . . . 88
6.2.2 Internal Coordinates . . . 93
6.3 Effective Atomic Repulsion . . . 94
6.4 Summary . . . 98

7 Magnetic Analytic BOP for Mn **100**
7.1 Introduction . . . 100
7.2 Model Parameters . . . 100
7.3 Relative Structural Stabilities of the Nonmagnetic Phases of Mn . . . 104
7.4 Relative Structural Stabilities of the Magnetic Phases of Mn . . . 111
7.5 Elastic Constants . . . 116
7.6 Vacancy Formation Energies . . . 121
7.7 Summary . . . 126

8 Magnetic Analytic BOP for Fe-Mn **128**
8.1 Introduction 128
8.2 Magnetic Analytic BOP for Fe 128
8.2.1 Model Parameters 130
8.2.2 Binding Energies 131
8.2.3 Elastic Constants 133
8.2.4 Defect Energy Calculations 134
8.2.5 Summary 136
8.3 Magnetic Analytic BOP for Fe-Mn 137
8.3.1 Lowest Energy Fe-Mn Structures 137
8.3.2 Model Parameters 138
8.3.3 Formation Energy of Fe-Mn 139
8.3.4 Elastic Constants 143
8.3.5 Vacancy Formation Energies 144
8.3.6 Stacking Fault Energy 146
8.3.7 Summary 148

9 Conclusions **150**

Bibliography **153**

List of Figures

1.1 A hierarchy of multiscale modelling 4

2.1 The experimental and theoretical temperature-pressure phase diagram of iron. 8
2.2 The ground state crystal structures of the 3d, 4d and 5d transition metal elements. 9
2.3 Up and down spin density of states for the rectangular d band model. 11

3.1 Illustration of the relaxed local coordination polyhedra that surround each of the 4 inequivalent atoms in α-Mn. 19

4.1 Ductility-strength relationship of high strength steels (HSS). 34
4.2 Microstructures of dual phase (DP) and transformation-induced plasticity (TRIP) steels. 37
4.3 Stress-strain diagram of transformation-induced plasticity (TRIP) and twinning-induced plasticity (TWIP) steels. 38
4.4 Experimental stacking fault energies for Fe-Mn. 41
4.5 Relation between the predominance of plasticity mechanisms in high-Mn steels and the stacking fault energy (SFE). 43
4.6 The phase diagram of binary Fe-Mn 45

5.1 Illustration of the recursion chain. 72
5.2 Comparison of BOP density of states (DOS) with and without explicitly positive DOS 83

6.1 DFT structural energy differences for the nonmagnetic phases of the group VII elements Mn, Tc and Re 88
6.2 Comparison of DFT total DOS for NM χ-phase, hcp and fcc for Mn, Tc and Re. 89
6.3 Comparison of DFT local DOS at the four inequivalent sites of the NM χ-phase for Mn, Tc and Re. 90
6.4 DFT total DOS as a function of band filling for the χ-phase, fcc, bcc and hcp structures for Mn, Tc and Re 91
6.5 Band structure, normalised by the bandwidth, of the fcc primitive cell for Mn, Tc and Re, plotted at their respective equilibrium volumes. 92
6.6 DFT structural energy differences for the 3d and 5d transition metals. 95

6.7 Contour plot of the difference in bonding energy of the hcp and χ-phase structures as calculated with the canonical TB model. 97

7.1 Binding energy curves for the α, β, γ, δ and ϵ phases of Mn as calculated using DFT, TB and BOP. 105
7.2 Comparison of the electronic DOS in nonmagnetic γ-Mn, ϵ-Mn and α-Mn, as calculated using DFT, TB and BOP. 107
7.3 Convergence of BOP binding energies to TB energies for Mn. 108
7.4 Densities of states for NM and AFM γ-Mn as calculated with TB and 14-, 16- and 18-moment BOP. 109
7.5 Structural energy differences as a function of band filling - DFT $3d$ and $5d$ series, canonical TB model and Mn TB model. 111
7.6 Structural energy differences as a function of band filling - Mn TB, 20-moment BOP, 14-moment BOP. 112
7.7 Convergence of BOP elastic constants to TB values for up to 34 exact moments - fcc γ-Mn 119
7.8 Densities of states for unstrained NM γ-Mn and with C' and C_{44} strains applied, as calculated with TB and BOP. 120
7.9 Change in local magnetic moments on nearest neighbours about a relaxed vacancy in an AFM α-Mn - DFT, TB, BOP 123

8.1 Binding energy curves for bcc, hcp and fcc Fe as calculated using DFT, TB and BOP. 132
8.2 Formation energies for low energy Fe-Mn structures as calculated using DFT, TB and BOP. 141
8.3 Stacking fault energies for binary Fe-Mn as calculated using DFT, TB and BOP. 147

Chapter 1

Introduction

In contrast to the other group VII elements, 4d Tc and 5d Re, which adopt non-magnetic hexagonally close-packed (hcp) ground state structures, at room temperature 3d Mn has a paramagnetic ground state which has a complex 58 atom cubic unit cell with 4 inequivalent atomic sites[1]. This structure, termed α-Mn, is isomorphic with the χ-phase of alloys such as $Fe_{36}Cr_{12}Mo_{10}$ and the binary Sc_5Re_{24}, and below a Néel temperature of T_N = 95 K has been found to exhibit complex non-collinear anti-ferromagnetic ordering[2,3]. The reason for the anomalous stability of the χ-phase for Mn has commonly been attributed to the presence of magnetism[4,5], just as ferromagnetic ordering stabilises the body-centred cubic (bcc) structure over hexagonally close-packed (hcp) in group VIII Fe. However recent density functional theory calculations[6] have predicted that without magnetism the χ-phase would still be the ground state of Mn and a viable justification of why this is so has yet to be proposed. With increasing temperature, up to a melting temperature of 1517 K, a further three phases are stabilised: complex 20 atom β-Mn, fcc γ-Mn and bcc δ-Mn[7]. Relatively little is known of the interplay between these competing structure types particularly at higher temperatures, and in comparison to other 3d metals there is a scarcity of data and theoretical models for Mn.

Additionally a better understanding of elemental Mn would be useful to model Fe-Mn alloys, the phase diagram of which is complicated by the effects of magnetism in both Fe and Mn[8,9]. Mn is a very important alloying element and Fe-Mn alloys are of scientific and industrial interest due to the occurrence of the shape memory effect[10,11] and of Invar and anti-Invar effects[12]. Furthermore high-Mn steels with extraordinary properties, the so-called transformation induced plasticity (TRIP)[13] and twinning induced plasticity (TWIP)[14] steels, have been discovered over the past 10-15 years[15,16]. Because of their high strength and high ductility[17,18] the automotive industry are keen to use TRIP and TWIP steels to lighten vehicle weights, thus improving fuel efficiency and reducing vehicle emissions, as well as improving safety features in vehicles. However there remain a number of issues with respect to the manufacture of these steels, and a number of questions regarding how and why these properties arise and what factors influence them. Stacking faults, which are planar imperfections in the normal stacking of the fcc lattice can increase the rate of work hardening by hindering the movement of dislocations[19] and the stacking fault energy strongly influences deformation mechanisms and mechanical properties[20]. Whether the TRIP or TWIP mechanisms occur in a given steel, and if so which dominates, has been shown to depend sensitively on the stacking fault energy (SFE)[16,21]. but experimental investigation of the stacking fault energy is challenging[22] and so insight from computational models is valuable. However zero temperature DFT calculations for Fe-Mn predict values of the stacking fault energy of the wrong sign[23] indicating that local magnetic fluctuations play a critical role in phase stabilisation in Fe-Mn alloys by stabilising fcc over hcp at high temperatures, just as Hasegawa and Pettifor found in the Fe phase diagram[24]. One approach to investigate such temperature-dependent phase transformations is to use interatomic potentials to drive large-scale atomistic simulations.

In the first half of the 20$^{\text{th}}$ century, work by metallurgists such as Hume-Rothery,

Cottrell and Raynor[13] led to a deeper understanding of the structure of metals and alloys and of what factors influence their microstructures. Their work has been expanded upon by many others since and, combined with the development of computer modelling methods, the modelling of metallic alloys is now well established and used to rationalise experimental observations and guide research into, for example, improving existing or developing novel steels. With the increasing power of computers modelling has become fast and cost-effective, and can be used to explore metastable states or systems under extreme conditions which are simply not accessible via experiment. A wide range of modelling techniques are available now including electronic structure calculations, atomistic simulations, microstructural models and macroscale continuum models. Individually these are able to account for phenomena that occur at length scales of nanometres to metres, and over time scales of picoseconds to hours. This hierarchy of different modelling techniques is illustrated in Fig. 1.1. The ambition of so-called multiscale modelling is to be able to explain physical and chemical processes operating at each length and time scale and qualify their effect on macroscopic, observable properties. To do this the difference between the length and time scales of the electronic structure and the macroscopic properties of a material must be bridged.

Over the past 50 years, the development of quantum mechanical *ab initio* density-functional theory (DFT) has allowed phase stabilities, defect behaviour and thermodynamic data to be calculated and even predicted. However while DFT is accurate, robust and largely free of empirical parameters, calculations are relatively computationally expensive. They tend, therefore, to be limited to studying small static systems of hundreds or thousands of atoms, or dynamically over short time scales (picoseconds), although linear-scaling DFT[25,26] and methods which combine quantum-mechanical embedding in classical molecular dynamics simulations[27] have been developed in recent years. Simple but fast interatomic potentials, which are appli-

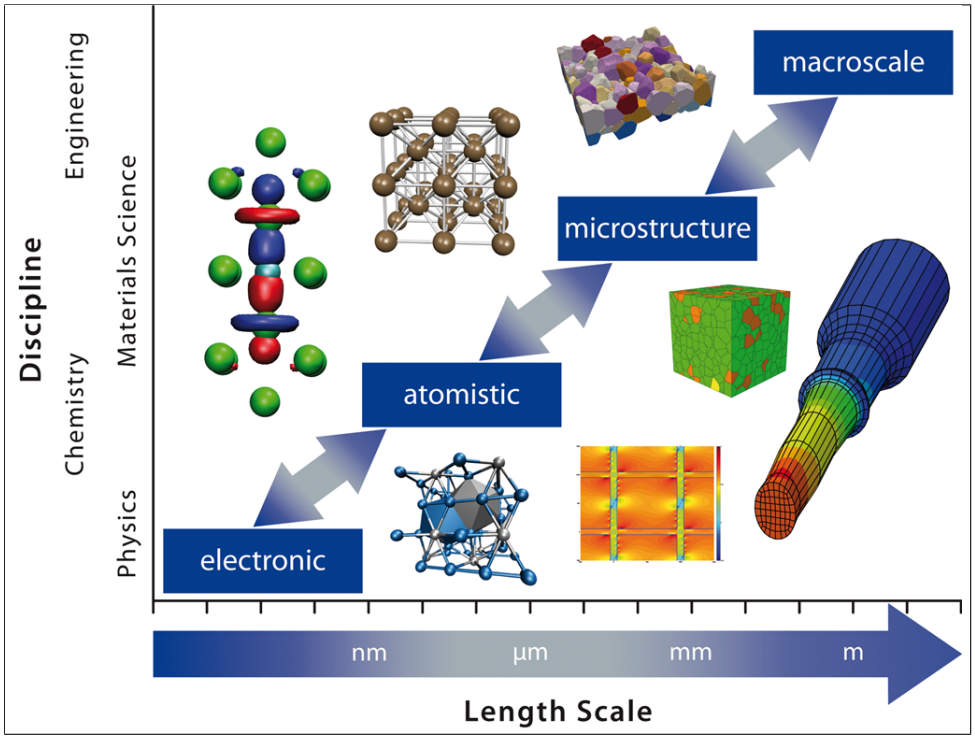

Figure 1.1: A hierarchy of multiscale modelling. For a seamless integration of different modelling techniques, which operate at different length and time scales, into one coherent multi-scale modelling framework the borders between the distinct disciplines must be bridged. Used with kind permission from the Interdisciplinary Centre for Advanced Materials Simulation (ICAMS), Ruhr-Universität Bochum, Germany.

cable to many millions of atoms, can still capture the key physics and chemistry of a system and can therefore be used to drive large-scale simulations, such as molecular dynamics (MD) or Monte Carlo (MC) simulations, in order to investigate dynamic processes at the atomic-scale like temperature-dependent phase transformations, defect migration and clustering in alloys. The output from MD and MC simulations can then be used as the input of microstructural models, thus linking two of the regimes in the multiscale modelling hierarchy. Two closely related interatomic potentials that have been used widely in the past to model metallic systems are the embedded-atom method (EAM)[28] and the Finnis-Sinclair (FS) potential[29]. However these are not well-equipped to describe transition metal bonding and lack

transferability. Another issue with classical interatomic potentials is that they fail to describe the effects of magnetism, a quantum mechanical effect, on the formation of chemical bonds. Given the crucial importance of magnetic fluctuations to temperature dependent phase stabilities of transition metals, and therefore steels, if the temperature dependent phase stabilities of magnetic Mn and Fe-Mn are to be investigated, then a potential that explicitly considers magnetism is required.

Conversely analytic bond-order potential (BOP) theory, which can be derived systematically from DFT via the tight-binding approximation (TB)[30,31], explicitly includes the valence dependence of bond formation and, as a result, can account for cohesion in transition metals, charge transfer and magnetism in a physically intuitive and transparent way[32,33,34]. BOP calculations scale linearly with the system size and within analytic BOP a Hellmann-Feynman-like term is used to evaluate the exact atomic forces. Analytic BOPs therefore offer the possibility of bridging the gap in complexity between electronic structure methods and current interatomic potentials and could be used to perform large-scale dynamic simulations, for example to model the local magnetic fluctuations with temperature that may be responsible for stabilising the different phases of Mn at high temperatures.

The outline of this thesis is as follows. In Chapter 2 an introduction to elemental iron, the major component of steel, and magnetism will be given. The role that magnetism plays in bucking structural trends across the transition metal series will be discussed and the importance of developing interatomic potentials that include magnetism highlighted. In Chapter 3 the experimentally observed allotropes of elemental Mn, and the magnetic ordering which they exhibit, will be introduced and the extent of previous experimental and theoretical investigations into elemental Mn will be reviewed. In Chapter 4 steels will be introduced and an overview of the extraordinary properties of Transformation Induced Plasticity (TRIP) and Twinning Induced Plasticity (TWIP) steels, will be given. Existing work on binary Fe-Mn,

commonly used as a proxy to investigate such steels, will be reviewed. In Chapter 5 the three modelling methods used in this project, namely DFT, tight-binding (TB) and BOP, will be described and details of the settings employed for each will be given.

Chapters 6, 7 and 8 will detail the results obtained within this project. Chapter 6 will discuss the driving force behind the anomalous ground state of Mn and a new theory of why the χ-phase is stabilised over hcp will be set out. Chapter 7 will present details of a new TB and BOP model for Mn and of the reproduction of structural energy differences, elastic constants and vacancy formation energies in comparison to reference DFT calculations. Chapter 8 will present details of new TB and BOP models for Fe and for Fe-Mn which will also be tested and compared with reference DFT calculations. In Chapter 9 the conclusions of the project will be stated.

Chapter 2

Elemental Iron

2.1 Introduction

The ground state of Fe, α-Fe (ferrite), has a ferromagnetic bcc crystal structure and is stable at ambient pressure (below 110 Kbar) and temperatures below 1185 K. It has a Curie temperature of 1043 K. From the experimental temperature-pressure phase diagram of iron[24], shown inset in Fig. 2.1, it can be seen that Fe also adopts the other two common metallic crystal structures at different temperatures and pressures. The fcc γ-Fe (austenite) is stable at ambient pressure between 1185-1667 K, while hcp ϵ-Fe (hexaferrum) can be formed at high pressures. It has been shown that the ferrite to hexaferrum transformation is martensitic, i.e. it is a sudden diffusionless shear process which takes place without atom diffusion or composition change[35]. Bcc δ-Fe, which is structurally identical to α-Fe, forms at temperatures above 1667 K. The $\alpha \rightarrow \gamma \rightarrow \delta$ transition is exploited in steel manufacturing processes but its origins remained controversial until just 30 years ago. One proposal[36] was that the γ-phase stability is stabilised by a vibrational contribution to the free energy while another[37] suggested that a magnetic contribution was responsible. Calculations by Hasegawa and Pettifor[24] were the first to be capable of theoreti-

cally calculating an accurate Fe temperature-pressure phase diagram, as shown in Fig. 2.1. Their work used an itinerant electron theory of band magnetism to show that the phase stabilities and transitions in iron are, in fact, driven by magnetic contributions to the entropy.

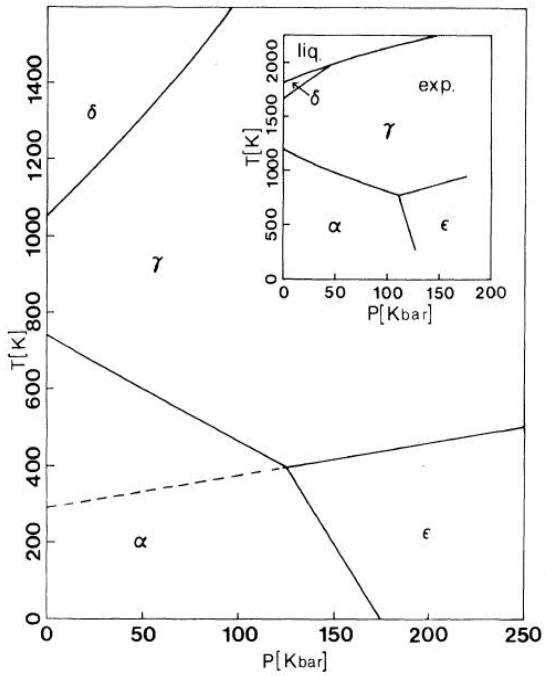

Figure 2.1: The theoretical and, inset, experimental temperature-pressure phase diagram of iron. The dashed line gives the metastable ϵ-γ boundary. The theoretical phase diagram was calculated by Hasegawa and Pettifor using a TB functional integral method. Taken from Ref. 24.

2.2 Modelling Magnetism in Transition Metals

Across the periodic table a trend accounts for the crystal structure adopted by the ground states of each group of the elements. As is shown in Fig. 2.2, for the $4d$ and $5d$ elements hcp structures are favoured for the first two transition metal groups, then bcc, then hcp again and finally fcc for the final three groups. Transition metals have wide s- and p-bands which overlaps a narrow d-band, the electrons in which

dominate states close to the Fermi level. While s-d hybridisation can be considerable, and indeed affect cohesive energies, for example in Ni[5], the trends described above have been shown to be driven by the filling with electrons of the d-band[38,39]. According to this trend Fe should have an hcp ground state like its 4d Ru and 5d Os counterparts. However it is found to have a bcc structure which is stabilised by the presence of ferromagnetism. The other two elements with anomalous structures, 3d Mn and 3d Co, also exhibit magnetism.

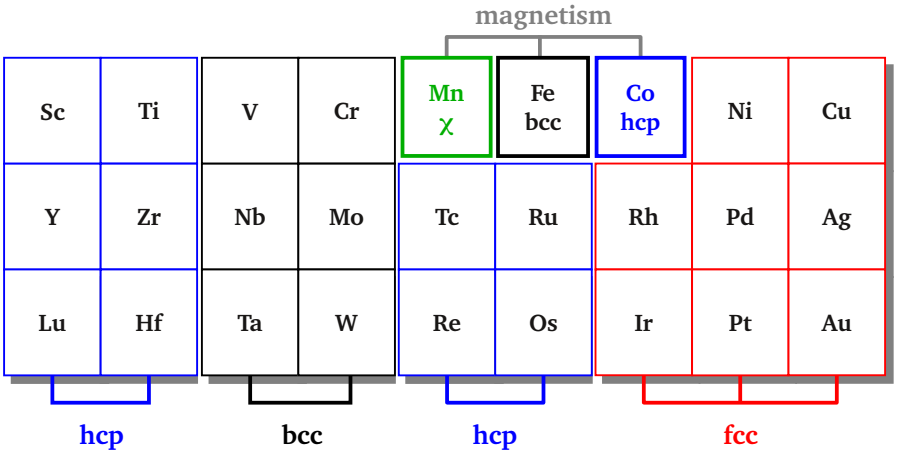

Figure 2.2: The ground state crystal structures of the 3d, 4d and 5d transition metal elements. Moving across the periodic table the trend for hcp $\rightarrow$ bcc $\rightarrow$ hcp $\rightarrow$ fcc ground states is observed. With respect to this trend the 3d elements Mn, Fe and Co have anomalous ground state structures taking the χ-phase, bcc and hcp respectively. The ground state structures of these three elements display magnetism.

In some cases magnetism can be seen to originate from magnetic moments at localised atomic sites while in other cases it is a result of the magnetic polarisation associated with a delocalised, itinerant 'sea' of conduction electrons. Local moments models of magnetism choose to stress localisation. For the simplest case, a free atom, the local magnetic moment of the atom which is integer-valued, is given by the difference in the up- and down-spin electrons in the valence shell. Examples

include the mean-field Weiss theory[40], the Heisenberg model, the Ising model[41] and the Landau model[42]. The Heisenberg model was used extensively to model metals but is limited to considering magnetic moments with integral-only values and does not account for the strong dependence of the magnetic moment on local environment and the type of magnetic ordering[43,44].

Alternatively, band theories of magnetism stress the itinerant character of the valence electrons[45]. A band model of magnetism based on the local spin-density functional (LSDF) theory of Hohenberg, Kohn and Sham[46,47,48] has been widely used within *ab initio* methods and produces qualitatively good ground state magnetic properties for transition metals without the need for any input parameters[49,50,51]. Applying a second-order expansion with respect to magnetism, the LSDF can be shown to reduce to another theory of magnetism, the Stoner model[52,51,53,54] which was originally developed phenomenologically in the 1930s. The key features of the Stoner model are its itinerant description of electrons, originally assumed to be in a parabolic band, and the introduction of an exchange energy, proportional to the magnetisation squared.

Within the transition metals, the valence d-electrons, which govern the cohesive energy and structural trends, are neither completely localized nor completely itinerant and, for example, Fe has been shown experimentally to exhibit both local moments and band magnetism[55,56]. However weight was given to the band magnetism interpretation by the work of Lonzarich and Gold[57] who demonstrated in low temperature studies that the electronic structure of ferromagnetic Fe could be decomposed into a superposition of two rigidly-shifted spin bands. They additionally showed that exchange splitting is large for d-like states but small for s- and p-states indicating that use of the Stoner model within a simple d band model is a reasonable approximation.

2.2.1 The Stoner Model of Magnetism

A nonmagnetic system has equal numbers of electrons in its spin-up $\uparrow$ and spin-down $\downarrow$ bands and the two spin bands therefore have identical electronic density of states (DOS). This is illustrated using the rectangular d-band model in Fig. 2.3.

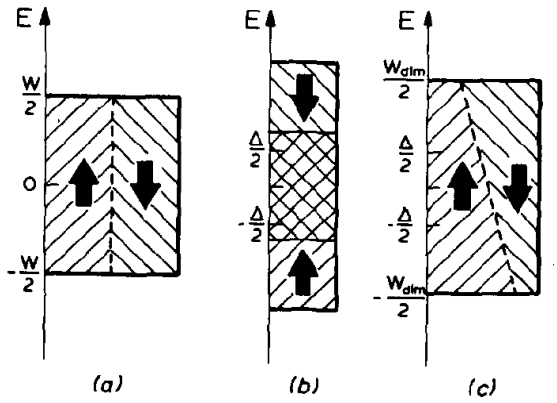

Figure 2.3: The up and down spin density of states associated with a given atom of the (a) nonmagnetic, (b) ferromagnetic and (c) antiferromagnetic states within the rectangular d band model. Taken from Ref. 58.

A net magnetic moment m_i may be created on an atom if electrons near the nonmagnetic Fermi level flip from one band to the other resulting in unequal occupancy of the two bands. This process has two associated effects on the total energy of the system, both of which can be quantified in terms of the magnetic moment, equal to the difference between the number of up-spin and down-spin electrons $N_d^{\uparrow} - N_d^{\downarrow}$, and the nonmagnetic DOS. Firstly, the presence of the magnetic moment is associated with a stabilising local exchange splitting Δ_i given by

$$\Delta_i = I m_i, \tag{2.1}$$

where the constant of proportionality, the Stoner parameter I, can be obtained from

DFT calculations or experiment. In LSDF calculations I has been shown to be $\sim$1 eV for ferromagnetic $3d$ metals[51,50,49]. Secondly, there is an increase in kinetic energy due to the flipped electron occupying a state higher in energy than its unflipped counterpart. A nonmagnetic system will become magnetic if the decrease in exchange energy due to the alignment of electron spins more than compensates for the increase in kinetic energy ΔT. The change in total energy is given by

$$\Delta U = \Delta T - \frac{1}{4} I m_i^2. \tag{2.2}$$

The Stoner Model of Ferromagnetism

If all the atomic magnetic moments are aligned ferromagnetically, that is in the same direction, then the atomic energy levels are seen to be shifted by $+\frac{1}{2}\Delta$ for up-spin electrons and $-\frac{1}{2}\Delta$ for down-spin electrons. As a result the DOS of the two spin bands are shifted rigidly apart by Δ, as may be seen in Fig. 2.3b. The associated increase in kinetic energy is equal to the number of electrons flipped, $\frac{1}{2}m$, multiplied by the energy change associated with each flip and can be expressed, to second-order, as

$$\Delta T = \left(\frac{m}{2}\right)\left(\frac{m}{2}\frac{1}{n(E_F)}\right) = \frac{m^2}{4}\frac{1}{n(E_F)} \tag{2.3}$$

where $n(E_F)$ is the DOS at the nonmagnetic Fermi level. Thus the overall change in energy is given by

$$\Delta U = \frac{m^2}{4}\left(\frac{1}{n(E_F)} - I\right), \tag{2.4}$$

and it follows that the simple criterion for instability with respect to ferromagnetic ordering is

$$I n(E_F) > 1. \tag{2.5}$$

Hence a larger nonmagnetic DOS at the Fermi level leads to a greater tendency towards the stabilisation of ferromagnetism. For bcc Fe the nonmagnetic DOS at

E_F is large enough to satisfy the criterion in Eq. 2.5 and FM bcc is the observed ground state.

The Stoner Model of Antiferromagnetism

The case for electrons flipping into an antiferromagnetic spin alignment results in a more complex expression for the exchange energy on account of a non-rigid band splitting. If all the atomic magnetic moments are aligned antiferromagnetically, then half the atoms have magnetic moments aligned upwards and the other half downwards. As a result the up-spin electrons see two types of atomic sites with energies shifted by $\pm\frac{1}{2}\Delta$, as do the down-spin electrons. Within the rectangular d-band model this corresponds to a skewing of the nonmagnetic DOS as may be seen in Fig. 2.3. The energy change upon antiferromagnetic ordering may be obtained by summing the band energies and subtracting off the exchange energy that has been double-counted[5] which gives

$$\Delta U = -\frac{1}{20}(W_{AFM} - W)N_d(10 - N_d) - \left(-\frac{1}{4}Im_i^2\right), \tag{2.6}$$

where the bandwidth of the antiferromagnetic band W_{AFM} is given in terms of the nonmagnetic bandwidth W as

$$W_{AFM} = \sqrt{1 + 3(\Delta/W)^2}W. \tag{2.7}$$

Using a Taylor series to expand Eq. 2.7 to second-order and then combining and re-arranging Eq. 2.1 and Eq. 2.6, the criterion for nonmagnetic instability with respect to antiferromagnetic ordering may be given by

$$I/W > \left[\frac{3}{10}N_d(10 - N_d)\right]^{-1} \tag{2.8}$$

This is equivalent to the exact second-order result, namely

$$I\chi_{\mathbf{q}}(E_F) > 1, \tag{2.9}$$

where $\chi_{\mathbf{q}}(E_F)$ is the response function corresponding to $\mathbf{q}$, the antiferromagnetic ordering wave vector[5].

2.2.2 Extensions of the Stoner Model

Despite its simplicity the Stoner model has been used to analyse a wide range of magnetic features in different metals[51,58,59]. For example it was the Stoner model that provided the first theoretical support[60] of Weiss' hypothesis[61] that there existed two stable magnetic states of fcc iron. One drawback of the Stoner model is that it has limited accuracy at temperatures above 0 K, for example above the Curie temperature T_C exchange splitting collapses completely making local moments impossible in the paramagnetic state. In contrast it has been observed experimentally that local moments with short-range order persist in the paramagnetic phases which occur above T_C in itinerant magnets[62,63,64]. To develop a more comprehensive theory of itinerant magnetism, suitable for modelling phase transitions in magnetic materials, a number of approaches have extended the Stoner model to include the possibility of local spin fluctuations at finite temperatures.

One approach to this is to characterise the paramagnetic state by persistent short-range magnetic order in which the direction of magnetisation is assumed to change relatively slowly from atom to atom[53]. The band structure may then be determined locally across a few nearest neighbours and therefore remains largely unaffected by the magnetic transition. As a result, the local exchange splitting, and hence magnetic moments, persist in the paramagnetic regime.

An alternative approach involves neglecting the short-range magnetic order and

treating the paramagnetic state as a collection of disordered local moments (DLM)[65,66,67,58]. Individual moments are then allowed to point either up or down, cf. the Ising model, and experience a local exchange field but the averaged exchange field is kept zero by ensuring that equal numbers of moments point up and down. In this way the system may be considered as a disordered binary alloy and treated within the coherent potential approximation (CPA)[68]. In contrast to the Ising and Heisenberg models, this approach pioneered by Hasegawa[67,69] and Hubbard[70] has local exchange fields which change in magnitude as they become thermally populated, allowing the amplitude of the local moments to fluctuate with temperature. Hasegawa applied this approach to Fe and showed why it exhibits both itinerant and localised moment behaviour[67] and it also lead to the demonstration of the occurrence of temperature-induced local moments in Fe fcc and hcp lattices[71]. Furthermore, Pettifor[58] used it to explain the trends in magnetic stability across the 3d transition metals and Hasegawa and Pettifor used it to calculate the Fe phase diagram and to show that phase transitions in Fe are driven by magnetic contributions to the free energy[24]. More recently Lavrentiev *et al.*[72] used a Magnetic Cluster Expansion to extend this approach to include non-collinear magnetic spins and vibrational effects and were able to predict both the Curie temperature of ferromagnetic bcc Fe and the Néel temperature of antiferromagnetic fcc Fe in good agreement with experiment.

A third approach is to use the Stoner model in conjunction with the Ginzburg-Landau model[73], the simplest known model for magnetic phase transitions, which allows a more accurate functional representation for the magnetic part of the many-body interatomic potential to be derived[74].

2.3 Summary

According to trends based on electronic band filling Fe should have an hcp ground state structure in line with other group VIII elements. However Fe is anomalous in this respect and adopts a ferromagnetic bcc structure. $3d$ Mn and Co also have anomalous ground state structures which exhibit magnetism. Magnetism in Fe, and other transition metals, is well described by the band theory of magnetism and within a simple d-valent model the phenomenological Stoner model can be used to describe both ferromagnetism and antiferromagnetism. Magnetic contributions to the free energy have been found to play a role in influencing the high-temperature $\gamma \rightarrow \delta$ phase transition in Fe and it is necessary to include these in order to correctly reproduce the pressure-temperature phase diagram for Fe.

Chapter 3

Elemental Manganese

3.1 Introduction

In contrast to the other group VII elements, $4d$ Tc and $5d$ Re which adopt hcp ground state structures, under ambient conditions the ground state of Mn is the paramagnetic χ-phase α-Mn[1]. In addition to α-Mn four other allotropes of Mn have been experimentally observed as a function of temperature and pressure namely β-Mn, γ-Mn, δ-Mn and ϵ-Mn. Both α-Mn and β-Mn have been shown to exhibit complex non-collinear magnetism.

From the perspective of developing models for Mn further complexity is added by the most stable allotropes being very closely spaced in energy at their equilibrium volumes. In contrast to Fe where, at 0 K, the magnetic energy stabilising the ferromagnetic (FM) bcc structure over nonmagnetic (NM) bcc is $\sim$500 meV/atom, in Mn the magnetic energy stabilising the antiferromagnetic (AFM) α-Mn structure over NM α-Mn was found in recent DFT calculations[6] to be around 40 meV/atom with a number of magnetic and nonmagnetic structures all lying within just 70 meV of the ground state.

3.2 Allotropes of Manganese

3.2.1 α-Mn

The room temperature ground state structure for Mn, paramagnetic α-Mn[1], has a 58 atom cubic unit cell (Structure Report symbol A12, Pearson symbol cI58, space group $T_d^3 - I\bar{4}3m$) which is comprised of four crystallographically inequivalent sites, I, II, III and IV, with relative population 2:8:24:24. These sites are surrounded by coordination polyhedra with 16, 16, 13 and 12 atoms, respectively. (We will see later in Sec. 3.2.1 that below a Néel temperature of 95 K a slight tetragonal distortion splits both site III and IV into two further sub-groups.) These local coordination polyhedra are illustrated in Fig. 3.1. Each site I atom (Fig. 3.1a) is surrounded by a Z16 Frank-Kasper coordination polyhedron[75,76] comprised of 12 Mn IV atoms arranged as four triangles on the faces of a tetrahedron formed by 4 Mn II atoms. This coordination polyhedra can therefore be denoted as [0:4:0:12]. The second nearest-neighbour shell of the Mn I atoms consists of 24 Mn III atoms. The 8 site II Mn atoms (Fig. 3.1b) are also surrounded by Z16 coordination polyhedra comprised of atoms [1:0:6:9]. The site III atoms (Fig. 3.1c) are surrounded by Z13 coordination polyhedra comprised of atoms [0:2:7:4]. The Z13 coordination polyhedra are not Frank-Kasper polyhedra because they contain one non-triangular, four-sided, face. The site IV atoms (Fig. 3.1d) are surrounded by icosahedral Z12 coordination polyhedra [1:3:5:3]. Although the α-Mn structure is not strictly a topologically close-packed (TCP) phase because it contains the Z13 polyhedra, χ-phase structures like α-Mn are often considered analogous to TCP phases because they share some of the same features, namely that they can be represented by stacking local coordination polyhedra of different radii, typically with larger atoms occupying the highest coordination sites and smaller atoms occupying lower coordination sites. A number of χ-phase binary alloys are formed between group VII $4d$ Tc and $5d$

(a) Site I, 2 atoms in cubic unit cell, Z16 coordination polyhedron

(b) Site II, 8 atoms in cubic unit cell, Z16 coordination polyhedron

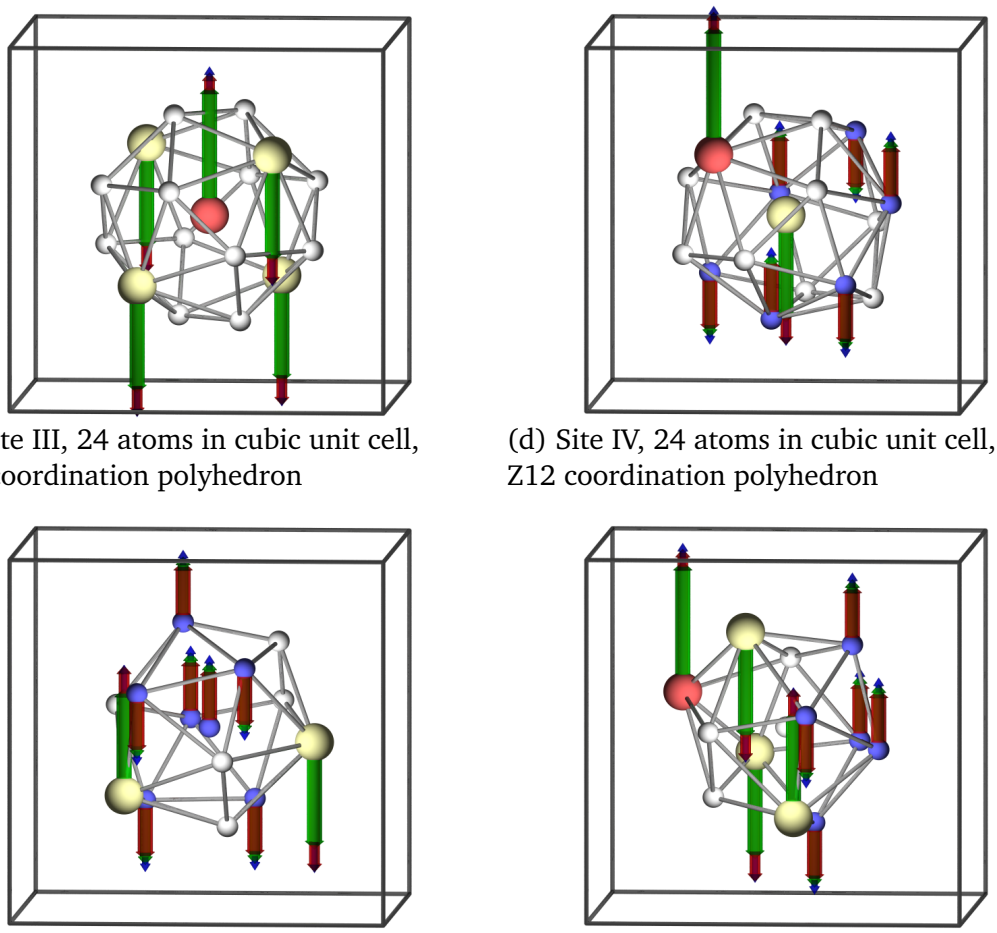

(c) Site III, 24 atoms in cubic unit cell, Z13 coordination polyhedron

(d) Site IV, 24 atoms in cubic unit cell, Z12 coordination polyhedron

Figure 3.1: Illustration of the relaxed local coordination polyhedra that surround each of the 4 inequivalent atoms in α-Mn. Atoms at each site are indicated by spheres of the following colour; site I - dark red; site II - pale yellow; site III - dark blue; site IV - white. The atomic coordinates plotted are taken from the DFT-calculated equilibrium volume of AFM α-Mn and the DFT magnetic moments are illustrated with green arrows. For comparison the magnetic moments from TB (red arrows) and 14-moment BOP (blue arrows) calculations, as described in Chapter 7, using the DFT-relaxed internal coordinates, are also included. For each atom the arrows for the three calculation methods are plotted concentrically with the smallest moment having the widest arrow diameter and the largest moment having the smallest arrow diameter.

Re with transition elements to their left in the periodic table, such as $Nb_{0.25}Tc_{0.75}$, $Zr_{0.14}Tc_{0.86}$, $Ta_{0.25}Re_{0.75}$ and $Hf_{0.14}Re_{0.86}$[5]. In these binary structures the 16-fold coordinated sites are typically found to contain the larger atoms of the minority alloying

elements while the 12- and 13-fold coordinated sites typically contain the smaller Tc or Re atoms. One common interpretation of the α-Mn structure is that atoms at the different sites behave as if of different sizes[4] with the site I and II atoms, which occupy the higher coordination sites, able, as we will see, to support large magnetic moments and the site III and IV atoms, which occupy lower coordination sites, able to support only small magnetic moments. In this way α-Mn has been termed a self-intermetallic compound[77] by analogy with common intermetallic χ-phase structures. Thus it has been generally thought that the presence of magnetism allows elemental Mn to behave like a binary χ-phase compound which is stabilised by the atomic size difference between the constituent atoms for favourable electron-per-atom ratios of band filling, and it is this behaviour that drives the stability of the χ-phase over hcp in contrast to elemental Tc and Re. Importantly, however, we will find in Section 6 that DFT predicts that α-Mn is still the most stable phase even when it is nonmagnetic, so that magnetism is not the critical factor in stabilising this complex crystal structure.

α-Mn also takes a complex magnetic ground state. Analysis of neutron diffraction data[77,3] has found that it is not only antiferromagnetic, as is expected for a $3d$ element in the middle of the transition metal series (see Fig. 8.1 of Ref. 5) but also that it has magnetic moments that are aligned non-collinearly. In particular below a Néel temperature of T_N = 95 K[2,3] non-collinear AFM α-Mn has large magnetic moments at sites I and II, with moments on each Mn I atom, approximately, antiparallel to both those of its Mn II nearest neighbours and its closest Mn I neighbours, and much smaller, but canted, moments at sites III and IV. The phase transition below the Néel temperature has also been found to be coupled to a slight tetragonal distortion which splits the site III and IV atoms into 2 further sub-groups, leading to a total of 6 inequivalent sites[77,78].

In DFT calculations, Hobbs *et al.*[6] managed to converge non-collinear AFM so-

lutions but these only became more stable than the collinear AFM ground state structure at atomic volumes expanded above 13 Å^3/atom, $\sim$18% above the calculated equilibrium volume of collinear AFM α-Mn of 11.08 Å^3/atom. This was attributed to the overbinding caused by the DFT exchange-correlation functional that they used, the GGA, which results in an equilibrium volume 7 % smaller than that observed experimentally. They concluded that the onset of non-collinear antiferromagnetism was driven by the frustration of the AFM exchange interaction of the 12-fold coordinated Mn IV atoms that are arranged in triangular motifs on the faces of the Z16 coordination polyhedra which surround the Mn I atoms. Above 13 Å^3/atom, the Mn IV magnetic moments grew larger and, within each triangular motif, ordered roughly 120° to each other, similar to the arrangement of nearest neighbour spins in the Néel phase of a frustrated triangular antiferromagnet. The resultant coupling drove the Mn III moments to rotate out of collinearity with the Mn I and Mn II atoms, and a very minor canting of the Mn II spins. Below 13 Å^3/atom, the local moments on the Mn IV atoms collapsed completely, which was sufficient to reduce the frustration and hence stabilise the collinear AFM magnetic structure. At atomic volumes greater than 14 Å^3/atom, it was also shown that the increased frustration in the collinear AFM α-Mn structure could be stabilised, not by the canting of spins, but by a structural distortion.

DFT investigations into collinear AFM α-Mn structures[79,80,81] have not all agreed on the size and alignment of the magnetic moments at each of the Mn sites. However recent consensus[6], in agreement with experimental findings, indicates the presence, firstly, of large moments on each Mn I atom that are oriented antiparallel to slightly smaller moments on its Mn II nearest neighbours, and, secondly, significantly smaller moments on sites III and IV. In the case of site IV atoms, the magnetic moments are virtually zero. A crystal can reduce the kinetic energy cost of magnetic ordering by undergoing a lattice expansion[82] which leads to a reduction

of the bandwidth. Hence crystals with a decreased packing density, such as the site I and II atoms which are surrounded by Z16 polyhedra, are able to support larger local magnetic moments while those with an increased packing density, such as the site III and IV atoms which are surrounded by the more closely packed Z13 and Z12 polyhedra, will have a broader d-band and, as a result, smaller local magnetic moments. For the 12-coordinated site IV atoms this increased local packing density completely quenches magnetism.

As DFT calculations[6] find only collinear AFM α-Mn to be stable around the equilibrium volume, non-collinear AFM α-Mn has not been studied in this work.

3.2.2 β-Mn

β-Mn is stable between 1000-1368 K and has a 20 atom cubic unit cell with A13 (cP20, $P4_132-O^6$) symmetry[83] consisting of two inequivalent sites, I (8 atoms) and II (12 atoms). The structure is more closely packed around the site I atoms which are surrounded by distorted icosahedra comprised of 3 Mn I and 9 Mn II atoms. The site II atoms are surrounded by Frank-Kasper Z14 polyhedra comprised of 6 Mn I and 8 Mn II atoms. Most examples of the A13 structural symmetry occur as binary alloys e.g. Fe_2Re_3 and Mg_3Ru_2[84].

Between 1000-1368 K β-Mn is paramagnetic and although it remains paramagnetic down to very low temperatures it has been shown to exhibit strong spin fluctuations[85,86] and NMR data[87] has been interpreted as showing that the site I atoms are approximately NM but that the site II atoms carry small paramagnetic moments. β-Mn has been considered as a spin-liquid, on account of structural frustration leading to a quenching of magnetism[88], but addition of a range of dopants has been found to drive a transition from the spin-liquid state to a spin-glass structure[87,89]. Consistent with the experimentally observed spin-liquid behaviour, DFT calculations[90] have predicted that at equilibrium volume a NM structure and an

almost ferrimagnetic (FiM) structure (with site I moments almost zero) are energetically degenerate. However at expanded volumes FiM structures[79,90] and even a non-collinear magnetic structure[81] have been predicted.

3.2.3 γ-Mn

Fcc γ-Mn is stable between 1368-1406 K. γ-Mn can be quenched to room temperature transforming via a magnetically induced transition[91] to a tetragonally distorted face-centred tetragonal (A5) structure below a Néel temperature of $T_N = 500$ K[92,93]. With the addition of 5 % Cu this reverts back to the fcc structure. Type-1 AFM ordering, which consists of successive z-planes ferromagnetically polarised with alternating signs from one plane to the next, has been found to be the lowest energy magnetic configuration of the fcc structure. From experimental data extrapolated to 0 K, magnetic moments of 2.1μ_B have been reported for such a structure[94].

3.2.4 δ-Mn

Bcc δ-Mn is stable between 1406-1517 K. DFT calculations have predicted magnetic ordering to be type-2 AFM (AFM2) with a transition to a type-1 AFM structure at atomic volumes greater than 14 Å^3/atom[90]. In type-2 AFM ordering, spins within a given [111] plane are parallel and spins on neighbouring [111] planes are antiparallel. The melting temperature of Mn is 1517 K.

3.2.5 ϵ-Mn

In x-ray powder-diffraction tests, under pressures of 158-165 GPa α-Mn has been found to transform to a phase interpreted as being either bcc, fcc or hcp[95]. From DFT data, Hafner *et al.*[90] predict that this phase is hcp in line with the stable crystal structures of the nonmagnetic group VII metals Tc and Re. Their results also

predict hcp to be nonmagnetic at equilibrium volume in contrast to fcc which is antiferromagnetic.

3.3 Tight-Binding Models for Manganese

The tight-binding approximation, which is a second-order expansion of the Kohn-Sham total energy in DFT with respect to charge and magnetic fluctuations[30,31,96,34], is significantly less computationally demanding than DFT. Despite its simplicity, it offers remarkable accuracy and an intuitive physical description of chemical bonding in molecules and cohesion in solids. Furthermore the tight-binding approximation can be coarse-grained to simpler interatomic potentials. TB models have been applied successfully to metallic systems, semiconducting systems and strongly covalent systems[97]. However, while a range of TB models exist for Fe relatively few for elemental Mn can be found in the literature, and those that can have restricted scope and application, highlighting the challenges faced in trying to reproduce its complex characteristics within a relatively simple model.

Mehl *et al.*[98] developed a non-orthogonal TB model for Mn but its scope was restricted to nonmagnetic structures. Süss and Krey[99] used an orthogonal TB model with a Hubbard-type exchange Hamiltonian to model antiferromagnetic α-Mn and fcc γ-Mn. However they were not able to obtain magnetic moments consistent with experiment unless they used a different value of the Hubbard U parameter for each of these two structure types, nor did they provide a comparison of the predicted relative stabilities. They attempted to calculate an antiferromagnetic α-Mn structure with non-collinearly ordered magnetic moments but this failed to converge self-consistently with respect to the energy and the spin polarisation. More recently McEniry *et al.* developed an orthogonal d-valent magnetic TB model and used it to study a number of nonmagnetic phases[100]. This model correctly predicts an α-

Mn ground state but it fails to reproduce the relative stabilities of a number of the other phases and it severely underestimates the nonmagnetic fcc-hcp energy difference. The results presented in Fig. 5 of Ref. 100 are for unrelaxed structures but having tested the model further we find that, firstly, the nonmagnetic and antiferromagnetic α-Mn structures do not undergo correct relaxation of their internal coordinates for atomic volumes greater than $\sim$11 Å^3/atom, and, secondly, that the β- and δ-Mn phases exhibit mechanical instability, with a negative C' for ferrimagnetic β-Mn and a negative C_{44} for antiferromagnetic δ-Mn.

3.4 Interatomic Potentials for Manganese

3.4.1 Introduction to Interatomic Potentials

Compared to DFT and TB, interatomic potentials are less accurate but far simpler and less computationally demanding. Within an interatomic potential the potential energy of a system of atoms is written as a function of the atomic coordinates from which the forces acting on a given atom may be determined by differentiation of the energy with respect to the coordinates. The forces can be minimised and the relaxed atomic structures of, for example, surfaces or defects may be investigated. Because evaluating the energy and forces within an interatomic potential is quick, they may be used to drive large-scale atomistic simulations, such as molecular dynamics (MD) or Monte Carlo (MC) simulations, in order to investigate phenomena such as temperature-dependent phase transitions. The accuracy and scope of any such simulations is clearly heavily dependent on the accuracy and scope of the underlying interatomic potential. Despite their relative simplicity an interatomic potential should describe cohesion and, where present, magnetism sufficiently well to reproduce reliable energies, atomic forces, structural properties, elastic constants, thermal properties, defect behaviour and surface characteristics.

Two simple, empirical, many-body interatomic potentials that have been used widely in the past to model nonmagnetic metallic systems are the embedded-atom method (EAM)[28] and the Finnis-Sinclair (FS) potential[29]. Although they are derived in slightly different ways their form and the level of physics that they include is comparable. EAM potentials are the most reduced form of the effective medium theory (EMT)[101] class of empirical potentials, while the FS potential uses the second-moment approximation[102,103], which is the simplest level of approximation within the tight-binding framework. Their functional form comprises two parts. A simple repulsive pair potential $\Phi(R_{ij})$ represents the electrostatic interaction and overlap repulsion between neighbouring atoms, while an attractive many-body embedding function $F(\rho_i)$, dependent on the atomic positions and the local atomic charge densities, represents the energy of embedding an atom at site i in the local charge ρ_i which arises from the tails of the atomic charge clouds ρ_{atom} on neighbouring sites j[5]. It is the embedding function which accounts for the unsaturated nature of metallic bonds. The energy can therefore be written as

$$U = \frac{1}{2}\sum_{i,j}\Phi(R_{ij}) + F(\rho_i), \tag{3.1}$$

where

$$\rho_i = \sum_j \rho_{atom}(R_{ij}). \tag{3.2}$$

Within a Finnis-Sinclair potential the embedding term is given by

$$F_{FS}(\rho_i) = -A\sqrt{\rho_i}, \tag{3.3}$$

and $\rho_{atom}(R_{ij})$ is interpreted as a sum of squares of overlap integrals[29]. Both the EAM and the Finnis-Sinclair potentials have been used successfully to produce good results for simulations of point defects, grain boundaries, surfaces and amorphisa-

tion transitions for, amongst other things, metals and alloys[104,105,106,107,108]. However while both potentials effectively include information about the tight-binding DOS up to the second moment, it is generally accepted that the energy differences between the common metallic structure-types, bcc, fcc and hcp adopted by most transition metals, are driven by higher than second-order moments[5,102]. Additionally the local atomic charge densities are spherically averaged and for this reason both potentials neglect the directional character of the covalent d-bonds found in transition metals. Furthermore they lack explicit valence dependence which can further restrict their transferability and lack an explicit treatment of magnetism.

A number of approaches have been taken to improve upon these potentials. For example, Lee and Baskes refined the EAM model to produce the more transferable modified embedded-atom method (MEAM)[109,110,111] which includes some directional bonding character by considering the atomic charge density as a sum of angularly-dependent partial charge densities. However MEAM models still do not explicitly include magnetism or consider the electronic structure and their functional forms tend to be fairly arbitrary[96]. Starting from the second-moment approximation, interatomic potentials which include contributions of the fourth moment have been developed variously by Carlsson[112] and Foiles[113] amongst others. However these potentials still cannot be easily extended to include contributions from higher moments nor do they account for the band-filling which drives the structural trends across the periodic table. Tersoff-Brenner potentials[114,115,116] are empirical many-body interatomic potentials which are based on the quantum-mechanical concept of bond-order[117]. These do include explicit angular dependence by involving nearest-neighbour bond angles, but their analytic form is empirical, with many unknown parameters which require fitting, and they account for only a single bond-order term the angular dependence of which reflects only that of an sp-valent σ bond[118].

An alternative approach based on DFT, known as generalised pseudopotential theory (GPT)[119], has been developed by Moriarty *et al.*[120,121,122] to produce a class of potentials known as model generalised pseudopotential theory (MGPT) potentials. These combine a volume-dependent energy term with explicit two-body, three-body and four-body terms which take directional bonding into account. They have been used to study a number of nonmagnetic bcc transition metals investigating features such as structural phase diagrams, high-pressure elastic moduli, ideal shear strength, vacancy and self-interstitial formation and migration, grain-boundary atomic structure, and dislocation core structure and mobility[123]. However these models have not been extended to include the effects of magnetism.

3.4.2 Magnetic Interatomic Potentials

One issue with classical interatomic potentials outlined above is that they fail to describe the effects of magnetism, a quantum mechanical effect, on the formation of chemical bonds. Given the crucial importance of magnetism in Mn, a potential that explicitly considers magnetism is required if its properties, and those of Fe-Mn, are to be investigated. Some EAM-type interatomic potentials for transition metals which do include an explicit treatment of magnetism have been developed. For example, Ackland *et al.*[124] described the total energy per atom as a sum of the up- and down-spin band energies and an additional exchange term, where the band energies were calculated within the second-moment approximation to the tight-binding model by a Finnis-Sinclair-type expression. Dudarev and Derlet[125] extended this approach further using an energy derived from the Stoner theory of magnetism[52] and mean-field Ginzburg-Landau theory. In both cases the potentials were fitted for use with ferritic Fe and capture volume-dependent changes in the magnetic moments in this particular structure type. However the lack of information about the shape of the DOS near the Fermi level means that they are unable to describe the

subtle structural dependence of the magnetic energy and are therefore unsuitable for modelling phase transformations. Indeed it has been shown that fourth, fifth, sixth, and higher, moment contributions to the local DOS are important for modelling defect energies as well as the phase diagram of iron[34].

3.4.3 Existing Interatomic Potentials for Mn

The availability of interatomic potentials for Mn, as for TB models, is somewhat scarce and only two semi-empirical Mn potentials could be found in the literature. For use in simulations of surface alloying and mixing at an Mn/Fe(001) interface, Torelli *et al.*[126] parameterised an MEAM model to reproduce a number of properties of α-Mn. However they gave no indication of the transferability of the model to other structure types. Kim *et al.*[127] parameterised an MEAM model for pure Mn, the 14 independent parameters of which were fitted to reproduce DFT relative stabilities (taken from Ref. 6 and 90) of α-, β-, γ-, δ- and ϵ-Mn at T = 0 K, elastic constants and the vacancy formation energy. However their model both severely underestimated the energy differences separating a number of the phases at T = 0 K and failed to yield any of the $\alpha \rightarrow \beta \rightarrow \gamma \rightarrow \delta$ phase transformations which are experimentally observed with increasing temperature. Despite the fact that both MEAM models were fitted to reproduce values of the elastic constants, they do so poorly.

3.5 Summary

$3d$ Mn has a complex χ-phase ground state in contrast to the other group VII elements $4d$ Tc and $5d$ Re which are hcp. The χ-phase has a 58 atom cubic unit cell and ground state α-Mn has been found to exhibit complex non-collinear magnetism. With increasing temperature three other allotropes of Mn have been experimentally

observed, all of which also exhibit magnetism. These include the complex cubic β-Mn which has a spin-liquid magnetic structure, fcc γ-Mn and bcc δ-Mn. A high pressure phase ϵ-Mn, thought to be hcp, has also been observed.

The research landscape of Mn, both theoretically and experimentally, is relatively sparse. Equally until recently there was limited consensus on what the magnetic configuration of α-Mn was, with a number of experimental results and DFT investigations predicting different magnetic states. Only three TB models for Mn could be found of which two have been used only to study nonmagnetic structures. Similarly only two interatomic potentials could be found both of which lack an explicit treatment of magnetism. One of these was only tested on α-Mn, while the other failed to reproduce any of the experimentally observed phase transitions. Just as for Fe it is anticipated that magnetic contributions to the free energy could play an important role in stabilising different Mn phases and therefore that the inclusion of temperature-dependent spin fluctuations is necessary in order to model magnetic phase transitions. With existing interatomic potentials lacking the ability to do this the development of a magnetic analytic BOP for Mn, which as we will see can, is desirable.

Chapter 4

Manganese-containing Steels

4.1 Introduction to Steels

Iron is one of the most abundant elements on earth and in its alloyed form comprises one of the most important groups of materials known to man, steels. Steels have been used for several millennia, examples of artefacts which are thought to be 4000 years old have been discovered[128], and on account of, amongst other things, their inherent strength and ductility have become one of the most commonly used and most cost-effective materials at mankind's disposal[129]. During the 16th and 17th Centuries efficient methods for its manufacture were developed and it started to become a more commonplace material, while large-scale production of relatively inexpensive steel became possible with the invention of the Bessemer process in the 1850s[130]. This was superseded in the 1950s by the Linz-Donawitz basic oxygen process[131] which, with some refinements, is still the method by which steel is manufactured today.

In the first half of the 20th century work by metallurgists such as Hume-Rothery, Cottrell and Raynor[13] led to a more comprehensive understanding of how factors such as the valence electron per atom ratio, microstructures, and heating and cool-

ing processes affect the final structure and properties of iron and steels. Since then the development of novel types of steel, which had until then always been an empirical process, has been influenced and guided by theoretical work.

While iron and carbon form the basis of steels, it is the addition of further alloying elements and choice of processing methods which give rise to such a wide variety of desirable microstructures and mechanical properties. Carbon contents are normally between 0.2 and 2 wt. % (henceforth, all constituent percentages are given as a weight % unless otherwise stated) while additions of other elements can range from a thousandth of a percent up to perhaps 30 %. Common alloying elements include Mn, Cr, Al, Si, Ni, Mo and B. Typically, additions of elements of less than 5 % are made to enhance, for example, strength and ductility, while additions of more than 5% are made to give special properties such as corrosion resistance or extreme temperature stability[132]. One way in which alloying elements can affect the properties of a steel is by stabilising particular microstructures. For example additions of Si, Al or Mn can help stabilise austenite, that is the fcc γ Fe structure, at room temperature and prevent the precipitation of brittle cementite (Fe_3C) which normally forms. The resultant austenitic steels are prized for their strength, ductility, wear resistance and corrosion resistance. The size of a C or B atom is small relative to an Fe atom so they enter α Fe and γ Fe lattices as interstitial solute atoms. In contrast, elements such as Al, Cr and Mn have similar atomic radii to Fe and therefore form substitutional solid solutions with Fe[129].

Steels may be perceived as unglamorous or old-fashioned materials yet they continue to be sought after for use in the most cutting edge of technologies as novel steels with improved strength, ductility, hardness, corrosion resistance and radiation resistance, continue to be developed. There now exist over 3,500 different grades of steel with different physical and chemical properties, approximately 75% of which have been developed in the last 20 years[133]. The extent of improvements

made in modern steels is pleasantly illustrated by the estimate that if the Eiffel Tower, built in 1889, were to be reconstructed today, it would require only one-third of the amount of steel originally used[133].

Steel remains the material of choice for the manufacture of car chassis, with an estimated 99 % of all passenger cars having a steel body and steel-based components accounting for 60-70 % of the weight of an average car[134]. With demands for increased safety, performance, reliability and comfort the weight of cars has increased markedly, for example the weight of a midsize passenger car in the EU increased by ∼80 % from ∼800 to 1400 kg over the period 1970-2010[134]. As such the development of light-weight advanced high-strength steels (AHSS) is currently of great interest to the automotive industry and lighter-weight steels could dramatically reduce the total mass of vehicles improving fuel economy and reducing emissions of CO_2 . If these steels have additional properties such as high energy absorption, impact strength and energy dissipation, then improvements in car safety can be made. The so-called Transformation-Induced Plasticity (TRIP) and Twinning-Induced Plasticity (TWIP) assisted properties of Mn-containing steels have been identified as highly promising candidates for this purpose. An illustration of their extraordinary strength and ductility in relation to other steel types is given in Fig. 4.1.

4.2 Mn-containing Steels

Manganese is the fourth most used metal in terms of tonnage and approximately 90 % of global Mn demand is for use as an alloying element in steels[136]. Mn is used as a minority alloying component in steels because it prevents liquid iron sulphide forming at grain boundaries preventing cracking and improving the workability of steels at high temperatures[19], and because it has deoxidising properties, thus

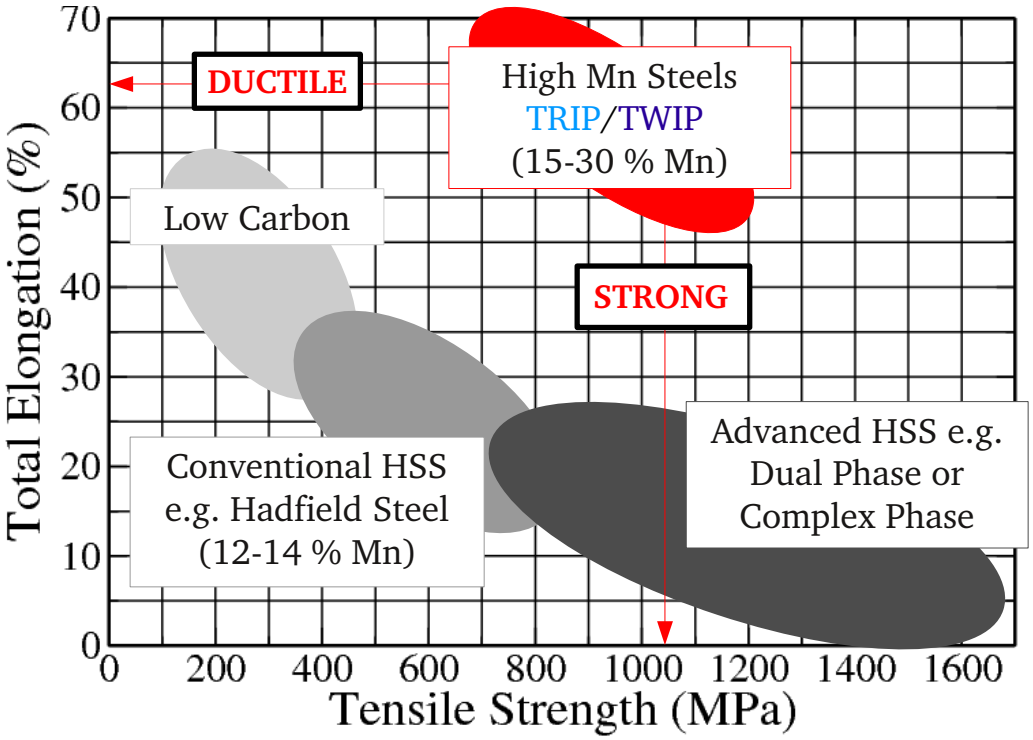

Figure 4.1: The ductility-strength relationship of some classes of high strength steels (HSS) including high-Mn TRIP and TWIP steels. Data taken from Ref. 135.

forming an integral part of many low-cost stainless steels. Mn is also one of the alloying elements that stabilises austenite at room temperature.

Steels with ~4 -8 % Mn can be brittle but high-Mn steels, that is those with more than 8 % Mn, are characterised by having excellent tensile strength, hardenability, impact toughness and wear resistance, and by having attractive deformation properties. Developed in the 19th Century by Sir Robert Hadfield, Hadfield steel typically contains 12-14 % Mn and 1 % carbon and was used to make the Brodie helmet used by British soldiers during the first World War[137]. It is still used today in the manufacture of tank tracks and blades for hydraulic cutting equipment.

4.2.1 Transformation-Induced Plasticity (TRIP) and Twinning-Induced Plasticity (TWIP)

Most conventional steels have microstructures that remain stable upon elastic or plastic deformation. However, recently, steels with higher manganese contents, $\sim$15-30 %, have been developed which, by virtue of being metastable with respect to deformation, possess extraordinary mechanical properties including high strength, high ductility, and exceptional plasticity[15,16]. Steels with such properties offer the possibility of vehicle components that are thinner, and therefore lighter, not only because they have the strength and energy absorption necessary to meet, or supersede, requirements of safety but also because they have the ductility to withstand highly deformative manufacturing processes such as stamping. Because Mn is a relatively cheap and abundant alloying element these steels may also be more economical to produce than existing materials used in vehicle manufacture. The high-Mn steels have been classified into two categories depending on the plasticity mechanism responsible for their properties. Transformation-Induced Plasticity (TRIP)-assisted steels involve a local martensitic phase transformations while Twinning-Induced Plasticity (TWIP)-assisted steels involve mechanical twin formation[16].

High-Mn steels may display both TRIP and TWIP character[138] and which of the two plasticity mechanisms predominates has been shown to depend sensitively on the stacking fault energy (SFE)[16,21]. The intrinsic SFE Γ_{fcc} is the Gibbs free energy required to create a platelet of hcp ϵ martensite of a thickness of only two atomic layers[18]. It is therefore a measure of the structural mismatch between the cubic γ austenite and hexagonal ϵ martensite phases and an increase in the SFE corresponds to an increase in the stability of the fcc austenite phase.

Although TRIP steels are now well established with major applications within the automotive industry there are issues relating to the processing of TRIP and

TWIP steels. For example, precisely because of their enhanced ductility they can be difficult to process and shape[139], and TWIP steels can be difficult to manufacture because of the high partial pressure of Mn required during melting and casting, and because of the tendency to form strong oxide scales during hot rolling which can lead to cracking. Additionally their high strength means that conventional steel-making equipment may not be strong enough to cold-roll such steels[140]. Attempting to understand and solve these problems has motivated an increase in both experimental and theoretical work on Fe-Mn alloys in recent years. The presence of Invar and anti-Invar effects in Fe-Mn alloys[12] which result in anomalous magnetisation, thermal expansion, heat capacity and elastic properties, and of the shape memory effect in Fe-Mn-Si alloys[10,11] has further driven interest in high-Mn steels. Additionally attention has been focused on binary Fe-Mn because the magnetic ground state of fcc γ Fe-Mn is still disputed[94,141,142,143,144,145].

Transformation-Induced Plasticity (TRIP) Steels

TRIP steels have a microstructure which includes retained austenite (γ) phases, typically more than 5 % volume, embedded in a matrix of ferrite, with smaller regions of martensite and bainite[135]. This microstructure is illustrated in Figure 4.2 alongside that of a commonly used high strength steel, dual phase (DP) steel, which like TRIP steels has small regions of strong but brittle martensite embedded in a ferrite matrix, but unlike TRIP steels contains no austenite or bainite. Under deformation the TRIP mechanism transforms regions of fcc austenite to regions of bcc and/or hcp martensite in a sudden diffusionless shear process. This can take place via one of two possible transformation pathways, $\gamma_{fcc} \rightarrow \epsilon_{hcp}^{Ms} \rightarrow \alpha_{bcc}^{Ms}$ or $\gamma_{fcc} \rightarrow \alpha_{bcc}^{Ms}$[146], the onset of which occurs at the martensite start temperature, Ms. Because the austenite is dispersed finely in the ferrite matrix the strength of the resulting martensite phases is preserved but the steel is not brittle.

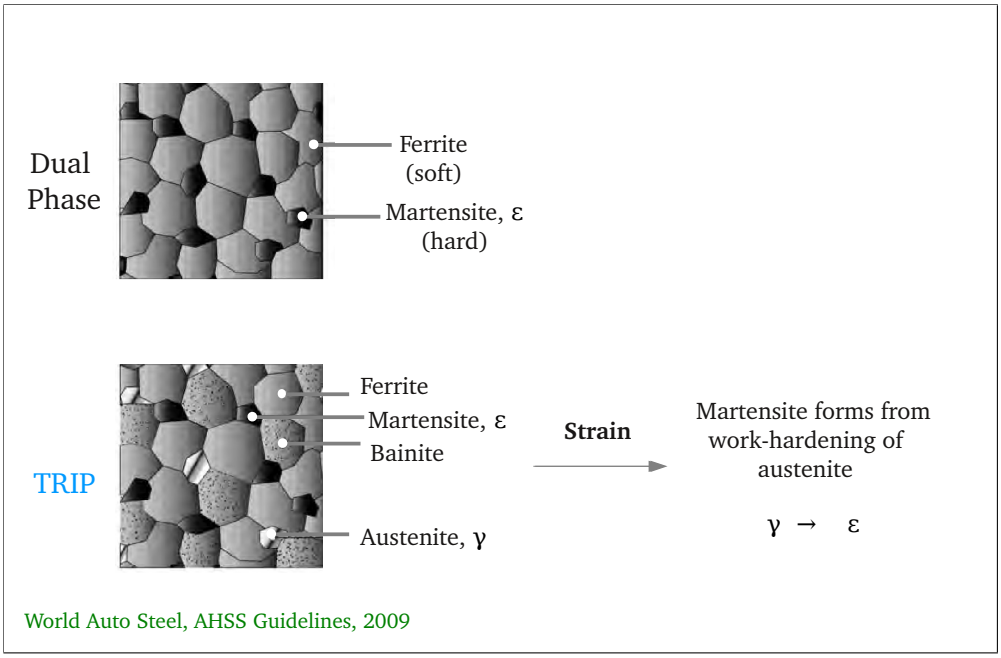

Figure 4.2: Microstructures of dual phase (DP) and TRIP steels. Illustrations taken from Ref. 135.

The phase transformation occurs in the austenite phase at martensite nucleation sites, known as shear bands, where local necking would normally take place. The local necking is retarded and hence the uniform elongation limit of the steel is improved[147]. Concurrently, local strain-hardening propagates through the steel increasing its strength. As a result, TRIP steels are characterised by having high strain-hardening rates, excellent formability, high tensile strength and improved elongation to failure compared to conventional steels. The high work-hardening is also a result of the dual phase nature of TRIP steels: the mixture of soft ferrite and hard bainite allows deformation of the ferrite while retaining a high tensile strength. The stress-strain curve of a typical TRIP steel is illustrated in Figure 4.3.

TRIP steels typically have a manganese content of up to 20 % although Cotes *et al.*[148] reported the $\gamma \rightarrow \epsilon$ phase transformation regime in steels with up to 30 % Mn. Frommeyer *et al.*[17] observed multiple martensitic $\gamma_{fcc} \rightarrow \epsilon^{Ms}_{hcp} \rightarrow \alpha^{Ms}_{bcc}$ transformations across a range of temperatures and strain rates in the TRIP steel Fe-

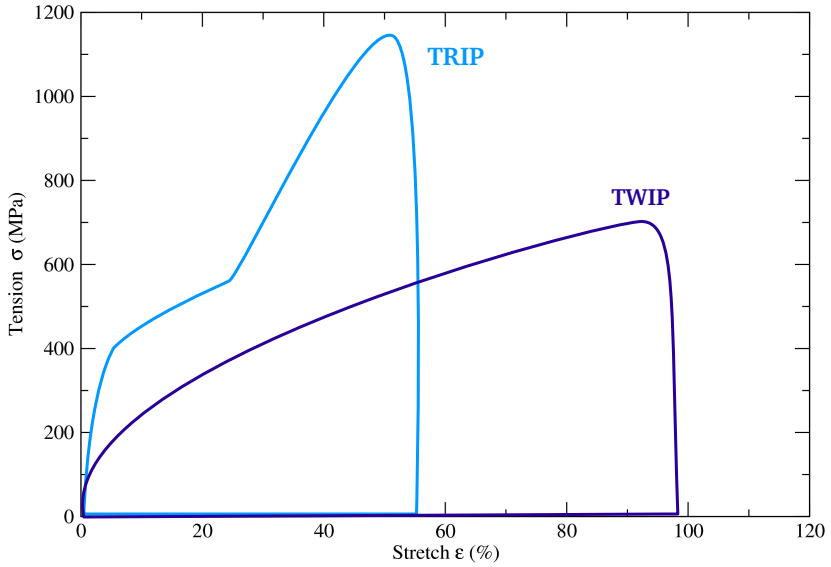

Figure 4.3: A stress-strain diagram comparing TRIP and TWIP steels. TRIP steels can resist high stresses without deforming while TWIP steels deforms with lower stresses but do not break until strain reaches around 90 % .

15Mn-3Al-3Si. This exhibited tensile strengths of more than 1000 MPa, elongation to failure of more than 55 % and extraordinary strain-hardening. Another point of interest associated with the $\gamma_{fcc} \rightarrow \epsilon_{hcp}^{Ms}$ transformation is the phenomenon of the shape memory effect in Fe-Mn-Si alloys[10,11].

Twinning-Induced Plasticity (TWIP) steels

TWIP steels have been developed over the past 10 years with the aims of providing improved ductility and energy absorption while maintaining strength and stability[16,17]. In contrast to TRIP steels, TWIP steels have a higher manganese content typically with ∼17-24 %, although TWIP steels with Mn concentrations as high as 33 % have been reported[138], and they are fully austenitic at ambient temperatures[135]. TWIP steels are typically less strong but more ductile than TRIP steels, as illustrated in Figure 4.3, and have a higher reserve ductility, that is their deforma-

bility is exhausted less rapidly because they have lower hardening rates.

The enhanced ductility found in TWIP steels is primarily a result of the formation of twins, $\gamma_{fcc} \rightarrow \gamma_{fcc'_T}$, caused by stacking faults in the crystal lattice. Twinning faults, which consist of mirrored sections of crystal lattice, occur if adjacent atomic layers within the lattice stack directly on top of one another in a way that disrupts the periodic stacking formation. Under deformation, an increased volume fraction of twinning leads to increased local strain-hardening which causes deformations to be absorbed through the surrounding area. As the SFE decreases it causes the distance between partial dislocations to become wider and imposes additional restrictions on their motion[149], which hinders their glide and reduces the probability of cross-slip. The increased ductility of TWIP relative to TRIP steels may also be due to the uniformly austenitic microstructure of TWIP steels and the resultant absence of any martensite phases which can cause nucleation of cracks.

Frommeyer *et al.*[17] observed extensive twin formation when a TWIP steel, Fe-25Mn-3Al-3Si, was deformed at low temperature (150 °C) at both high and low strain rates. This exhibited tensile strengths of more than 650 MPa and elongation to failure, ϵ_f, of ∼80-95 %. Frommeyer also reported the same TWIP steel had a specific energy absorption, E_{spec} of 0.5 J/mm^3, while conventional deep drawing steels typically have E_{spec} of just 0.16-0.25 J/mm^3[15]. Allain *et al.* have reported TWIP steels with tensile strengths as high as 1200 MPa and elongation to failure of ∼70 %[150,18].

The Stacking Fault Energy

While the extent of austenite to martensite phase transformations and twin formation can be measured in a quite straightforward manner via, for example, optical microscopy, X-ray diffraction, scanning electron microscopy (SEM) and transmission electron microscopy (TEM)[16] the factors that drive the predominance of the

TRIP or TWIP mechanisms, namely the SFE and the Gibbs free energy, cannot.

A perfect fcc crystal has close packed layers arranged in an ABCABCAB... stacking sequence. A stacking fault, the most commonly found fault in fcc metals, is produced by shearing which introduces an irregularity into the overall stacking sequence such that it becomes ABCACABC.... The SFE of an extended stacking fault under ambient pressure is defined as the excess free energy per unit area

$$\Gamma = \frac{(G^{def} - G)}{A_{int}}, \tag{4.1}$$

where G^{def} and G are the free energies of the system with and without the stacking fault, respectively, and A_{int} is the area of the stacking fault[151]. The SFE can be determined experimentally by using transmission electron microscopy (TEM) to directly observe and measure the configuration of dislocations in thin foils[152]. However this can be challenging, time consuming and inaccurate[22,153,154,155] and there are only a few examples found in the literature for Fe-Mn steels. Remy *et al.*[154,155] demonstrated that for a number of transition metal alloys, including a high-Mn steel, there is a marked increase of the SFE with increasing temperature. The two experimental SFE measurements for Fe-Mn alloys that can be found in the literature are shown in Fig. 4.4. These are the results of work by Schumann *et al.*[156] and Volosevich *et al.*[157] who both concluded that the SFE decreases with increasing Mn concentration for Mn concentrations less than $\sim$ 15 %, reaches a minimum and then increases with increasing Mn concentration. However the Volosevich results often are treated, quite rightly, with a little wariness due to vagueness and ambiguity in their description of what was actually tested and how.

In practice both TRIP and TWIP steels are made with small additions of Si and Al[15], typically in the region of 2-4 %, and C, less than 0.5 %, and these have been shown to influence the SFE. In dilatometric tests Ishida *et al.*[159] showed that ad-

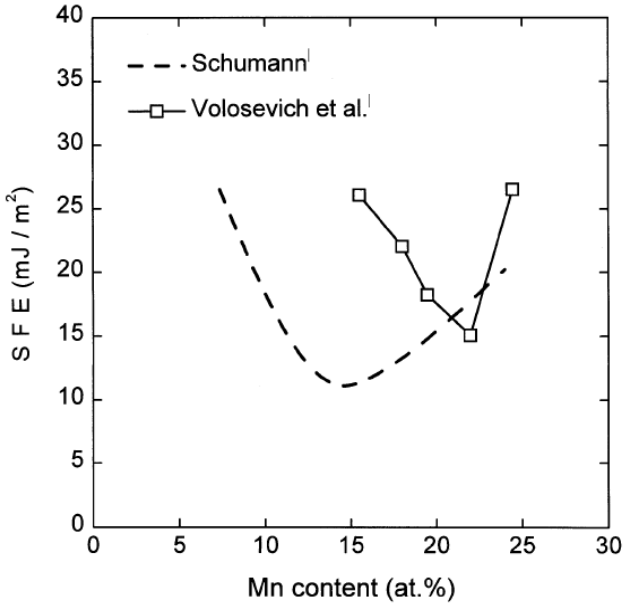

Figure 4.4: Experimental stacking fault energies for Fe-Mn determined by Schumann[156] and Volosevich[157]. Figure taken from Ref. 158.

ditions of Al increase the SFE of the austenite and suppress the martensitic transformation, $\gamma_{fcc} \rightarrow \epsilon_{hcp}^{Ms}$, thus favouring TWIP behaviour. In contrast, using X-ray diffraction the addition of Si was shown by Schramm and Reed *et al.* to decrease the SFE and sustain the martensitic phase transformation, thus favouring TRIP behaviour[160].

Given that the experimental evaluation of the SFE and Gibbs free energy is not trivial, insight from theoretical Fe-Mn models is highly valuable. Until recently most evaluations in the literature of $\Delta G^{\gamma \rightarrow \epsilon}$ and the SFE have made use of continuum models, such as the regular solution model (RSM) originally proposed by Hirth[161], to calculate $\Delta G^{\gamma \rightarrow \epsilon}$ and then the Olson and Cohen model[162] to calculate the SFE. The Gibbs free energy is dependent on chemical composition and temperature, and the SFE is directly proportional to $\Delta G^{\gamma \rightarrow \epsilon}$. The calculation of the Gibbs free energy uses thermodynamic data as its input which is taken from either experimental re-

sults[163,158,164], for example from measurements of partial dislocations which form a stacking fault.

Using continuum models the effects of a number of factors on the SFE have been evaluated, most widely the effect of the increasing concentration of Mn in Fe-rich Fe-Mn alloys[163,165,166,158,167,168]. For example, RSM calculations by Lee *et al.*[158] found, in qualitative agreement with experiment[157,156], that the SFE decreases with increasing Mn concentration at low Mn concentrations, reaches a minimum and then increases with increasing Mn concentration. The minimum SFE of $\sim$4 mJ/m^2 was found to occur at $\sim$12 % Mn. Similarly Nakano[168] predicts a SFE with a minimum of $\sim$13 mJ/m^2 at around 5 % Mn. However Saeed-Akbari *et al.*[167] predicted all SFE to be negative with the minimum, of -13 mJ/m^2, at around 12 % Mn. Trends in the effects on SFE upon the addition of Si and Al have also in some cases been reproduced[169,165,166] and the effects of grain size[158] and temperature[18] have also been investigated. For example for the ternary alloy Fe-22Mn-0.6C, Allain *et al.*[18] predicted the SFE to be 10 mJ/m^2 at 77 K, favouring TRIP, 19 mJ/m^2 at 293 K, favouring TWIP, and 80 mJ/m^2 at 673 K, thus favouring dislocation gliding.

In summary, investigations into the SFE and the Gibbs free energy using continuum models have suggested that the TRIP mechanism requires a small SFE, < 18 mJ/m^2 and a negative $\Delta G^{\gamma\rightarrow\epsilon}$. That is the hcp martensite phase must be thermodynamically more stable than the fcc austenite[18]. In contrast the TWIP mechanism requires a higher SFE compared to TRIP, $\sim$12-35 mJ/m^2[18], and a positive $\Delta G^{\gamma\rightarrow\epsilon}$ ($\sim$110-250 J/mol) because the twinning occurs within the austenite phase. The prevalence of each plasticity mechanism as a function of SFE is illustrated in Figure 4.5. The SFE for both TRIP and TWIP steels are small relative to the SFE found in other metals. For example, Gallagher[170], gives a review of SFE obtained from various experimental methods and finds a consensus value for the SFE in Cu is 55 mJ/m^2, in Al is 200 mJ/m^2 and for a range of stainless steels is 20-60 mJ/m^2.

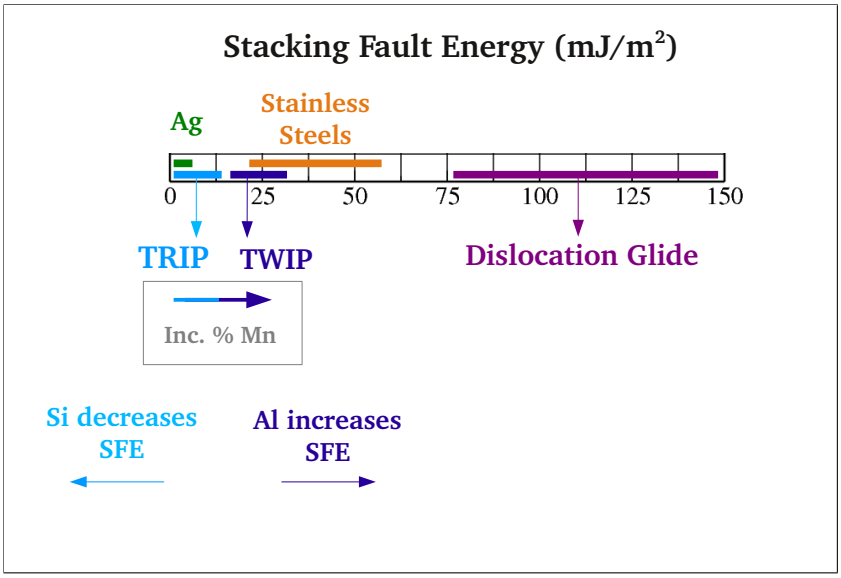

Figure 4.5: Illustration of the relation between the predominance of plasticity mechanisms in high-Mn steels and the stacking fault energy (SFE). The SFE for various common metals are also given

However while continuum models allow the SFE and Gibbs free energy to be estimated as a function of chemical composition they cannot account for configurational effects, atomic interactions or vibrational contributions. Thus whilst providing important insight into qualitative trends they are not capable of studying the physical mechanisms involved in stacking fault formation or the effects of local chemical or magnetic ordering. In contrast to the continuum approach, electronic and atomistic models are able to evaluate these effects and atomistic models in particular, because they can be used to study large systems dynamically, offer the possibility of insight into the formation and evolution of stacking faults and therefore the TRIP and TWIP plasticity mechanisms. The starting point for studying high-Mn steels with electronic and atomistic modelling methods is the binary Fe-Mn system.

4.3 Binary Fe-Mn

4.3.1 Fe-Mn Phase Diagram

The phase diagram of binary Fe-Mn is illustrated in Figure 4.6. The symbols indicate the results of experimental work while the solid and dashed lines indicate the results of CALPHAD (CALculation of PHAse Diagrams)[171] assessments[172,9]. There exist five major stable phases: liquid, α Mn, β Mn, Fe-rich bcc and intermetallic γ Fe-Mn (fcc). As is found for elemental Fe and Mn the presence of magnetism complicates the picture further[8,9]. Neutron scattering experiments by Endoh *et al.*[94], at temperatures ranging from 1.5-500°K, found there to be three distinct regimes of spin alignment; an AFM γ-Mn structure for concentrations up to 30 at. % Fe; a non-collinear structure for 40 to 80 at. % Fe; and a FM γ-Fe type structure above 80 at. % Fe. Furthermore they proposed a non-collinear, multiple-spin-density wave (cf. the ground state of Cr) to exist at $\sim$50 at. % Fe. (Structures with less than 40 % Fe were stabilised with 5 % Cu and those with more than 85 % Fe with small additions of 4 % C.) Conversely room temperature elastic and inelastic neutron scattering experiments by Bisanti *et al.*[173] supported a collinear AFM structure for γ $Fe_{66}Mn_{34}$.

4.3.2 Modelling of Fe-Mn

Density Functional Theory Calculations for Fe-Mn

The first theoretical calculations on γ-Fe-Mn were by Asano and Yamashita[174] who used a rigid-band model to obtain the DOS and magnetic moments for an antiferromagnetic structure. Kübler *et al.*[175] and Fujii *et al.*[176] subsequently performed total energy band calculations on a number of non-collinear γ-$Fe_{50}Mn_{50}$ structures based on the $L1_0$ CuAu crystal type, but neither of them were able to predict the spin-density wave magnetic configuration observed experimentally by Endoh[94]. More

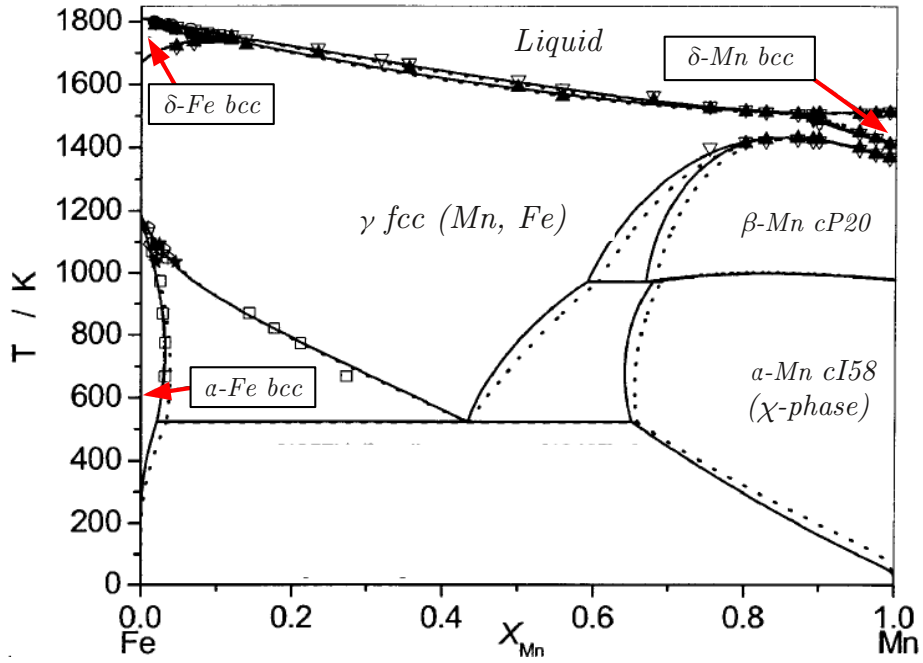

Figure 4.6: The phase diagram of binary Fe-Mn taken from Ref. 9. Symbols indicate experimental data points while the solid[9] and dashed[172] lines indicate the results of CALPHAD calculations. Compositions are given in weight percent.

recently *ab initio* calculations have predicted non-collinear ground state magnetic configurations but there is still considerable debate as to what the true ground state magnetic configurations for ordered and disordered γ-Fe_{50}-Mn_{50} are[141,142,143,144,145].

Recently *ab initio* methods have been used to calculate thermodynamic properties of Fe-Mn. For example, Dick, Hickel, Neugebauer *et al.*[177,23] used the axial next-nearest-neighbour Ising (ANNNI) model[178] to calculate the SFE. To first order this assumes that the SFE is given by the difference between the total energies of idealised fcc and hcp crystals making it a very simple way of evaluating the SFE. Using nonmagnetic phases and ordered structures they predicted a linear increase of the SFE with increasing Mn concentration. By including compositional disorder using special quasirandom structures (SQS)[179] they were able to reproduce the parabolic behaviour of the SFE observed in experiments[156] with a minimum predicted for a Mn concentration of ~25 %. However these SFE were all negative

implying that hcp is more stable than fcc at all compositions. Using a disordered local moments (DLM)[65,66,67,58] picture they simulated the SFE of paramagnetic phases the dependence of which on Mn concentration was also parabolic with a minimum predicted for a much higher Mn concentration of $\sim$40 %. The SFE of the paramagnetic phases were also all negative but less so, particularly for the Fe-rich structures. These results suggest that magnetism plays an important role in phase stabilisation in Fe-Mn alloys by stabilising fcc over hcp, and therefore in determining the SFE of a given Fe-Mn alloy.

Gebhardt *et al.*[180] have also reported 0 K DFT calculations detailing the relative stabilities of fcc and hcp phases for Fe-Mn random alloys focusing on Fe-rich structures with 15-40 % Mn. They considered fcc alloys with disordered magnetic moments, corresponding to the paramagnetic phase above the Néel temperature, and an ordered collinear antiferromagnetic ordering corresponding to a room temperature structure. The hcp alloys were always treated as having disordered magnetic moments. The coherent potential approximation (CPA)[68] was used to treat substitutional disorder while the disordered local moments (DLM)[65,66,67,58] model was used to simulate the paramagnetic phases. For paramagnetic fcc and hcp they calculated that the enthalpy difference ΔH between the hcp and fcc phases was negative and that an increase in Mn concentration decreased ΔH, i.e. the hcp phase was more stable than fcc at all concentrations and became more stable as the Mn concentration was increased. This was in contrast to Gebhardt's[180] CALPHAD results which predicted, for paramagnetic fcc and hcp, a ΔH that was negative for all concentrations but which became less negative as the Mn concentration was increased. For the collinear AFM fcc structure their DFT results predicted a ΔH which was negative at 15 % Mn but which increased with increasing Mn concentration and became positive ΔH at a Mn concentration of $\sim$25 %. These results were in better agreement with their CALPHAD calculations. Their results however do not show

any parabolic behaviour of ΔH as a function of Mn concentration, which would be expected given the trends in SFE observed experimentally[156] and reproduced in a number of continuum models[158,168]. Nevertheless, these results highlight the strong influence that magnetism plays in stabilising Fe-Mn alloy structures and that the AFM ordering strongly stabilises the fcc phase over a range of Mn concentrations. The same group extended their calculations to analyse the effects of the addition of Al and Si on the lattice stabilities of hcp and fcc[181]. They performed sets of calculations using two different *ab initio* methods and again used disordered and ordered magnetic structures for the fcc structures but treated the hcp structures as nonmagnetic. They found that additions of Al strongly stabilised fcc independent of the magnetic state and of the calculation method used. For Si however the results were less clear and for the AFM ordered fcc the two calculation methods produced qualitatively conflicting results. Additionally, over the whole Mn concentration range studied, in contrast to the results of the first calculation method, the second *ab initio* method predicted hcp to be more stable than fcc. Again no parabolic behaviour was observed.

Lintzen *et al.*[182] recently produced an Fe-Mn phase diagram, for bcc-, fcc-, and hcp-based structures from DFT calculations and compared it with an analogous plot obtained using the CALPHAD method[172]. However the two phase diagrams show quite different behaviour with the DFT approach predicting bcc $\rightarrow$ hcp $\rightarrow$ fcc and the CALPHAD approach predicting bcc $\rightarrow$ fcc $\rightarrow$ hcp as a function of increasing Mn content. A significant source of this disagreement is likely to be that the phase diagrams are valid at different temperatures, 0 K (DFT) and 298 K (CALPHAD).

Tight-Binding Models for Fe-Mn

Süss and Krey[99] developed a TB model for Fe-Mn and applied it to ordered γ-$Fe_{0.5}Mn_{0.5}$ alloys with collinear spins. However their model failed to reach self-

consistent convergence and did not obtain a magnetic structure. The TB model for Mn developed by Mehl *et al.*[98] was not extended to an Fe-Mn system. McEniry *et al.*[100] developed an Fe-Mn TB model which was shown to reproduce the qualitative features of a DFT enthalpy of formation plot for nonmagnetic structures including bcc, fcc and hcp. However this makes use of an elemental model for Mn referred to in Sec. 3.3 with which a number of issues were found notably an underestimation of the nonmagnetic fcc-hcp energy difference, negative elastic constants and incorrect structural relaxations at large atomic volumes.

Atomistic Simulations and Interatomic Potentials

Kakehashi *et al.*[183] used semi-classical MD simulations to simulate disordered fcc Fe-Mn alloys with non-collinear magnetic spin configurations. Using 100 atom unit cells, periodic boundary conditions and an MD temperature of 25 K they predicted a number of spin configuration regimes some of which match the three regimes observed experimentally by Endoh[94]. However they focused solely on the fcc structure and did not explore the relative stabilities of other structure types. No MD simulations of SFE in Fe-Mn could be found in the literature but Yamakov *et al.*[184] used MC and MD to assess the effects of the SFE on deformation behaviour by comparing the calculated SFE of a hypothetical low-SFE transition metal (Pd, modelled using an EAM potential) and a high-SFE transition metal (Al, modelled using an Ercolessi and Adams potential[185]).

The semi-empirical MEAM developed by Kim *et al.* for Mn was extended to Fe-Mn[186,127] and used to calculate the SFE as a function of Mn concentration using two approaches, firstly using simple static energy calculations and secondly using MC simulations to include the effects of compositional disorder. Importantly they 'set' the SFE of pure Fe to zero so it is not obvious whether the SFE that they calculated are actually positive or negative. Within the simple energy calculations they predict

that the SFE increases with increasing Mn concentration with the minimum value predicted for pure Fe. With the inclusion of compositional disorder they predict a similar trend but with a minimum SFE for an Fe-Mn alloy with ∼5 % Mn, which is in closer agreement with the results of experiment, RSM models and the *ab initio* results of Dick *et al.*[23]. However in addition to it not being clear whether they have predicted positive or negative SFE, within both approaches the magnitudes of the SFE are an order of magnitude smaller than those from experiment or the RSM approach, and two orders of magnitude smaller than those predicted by Dick *et al.*[23].

Neural network models have also been developed to investigate the mechanical properties of FeMn TRIP and TWIP steels[187] but these lack the transparency and intuitive description of bonding found in conventional interatomic potentials.

4.4 Summary

Steels are a very important class of materials and can, by tailoring their composition and microstructure, have a highly varied range of properties. Mn has long been used as an alloying element in steels but recently two classes of high-Mn steels, the so-called transformation-induced plasticity (TRIP) and twinning-induced plasticity (TWIP) steels, have been developed which combine exceptional strength and ductility. These are of great interest to the automotive industry but there exist a number of issues with their manufacture and a deeper understanding of how and why they possess their extraordinary properties is desirable. The presence of one or both of the plasticity mechanisms has been found to be dependent on the stacking fault energy (SFE) which is in turn dependent on Mn concentration, the presence of alloying elements, grain size and temperature. TRIP steels require a small SFE while TWIP steels require a slightly larger SFE. The SFE is difficult to measure by exper-

iment and so continuum models have traditionally been used to assess it. These models however cannot account for configurational effects, atomic interactions or vibrational contributions. More recently therefore DFT calculations have been used to investigate Fe-Mn alloys and the important influence of magnetism and configurational disorder on the SFE have been highlighted. However 0 K DFT calculations predicted negative SFE in contrast to experimental evidence suggesting that the effects of temperature should also be considered. Interatomic potentials can be used to drive large-scale atomistic simulations and investigate the effects of temperature on the SFE but currently there exist no Fe-Mn interatomic potentials that explicitly include the effects of magnetism.

Chapter 5

Methodology

5.1 Introduction

The results presented in this thesis have been calculated using density functional theory and tight-binding and bond-order potential models. The tight-binding method, which can be systematically derived from DFT, provides the starting point from which BOP theory is derived. The following sections outline the key feature of each of the three methods.

5.2 Density Functional Theory (DFT)

DFT is an efficient and reliable method for computing the ground state energetics of a wide variety of materials from first principles (*ab initio*)[188]. By elevating the particle density $\rho(\mathbf{r})$ from one of many observables to the key variable, carefully approximated solutions to the Schrödinger equation can be found and electronic properties can be calculated.

5.2.1 The Time-Independent Schrödinger Equation

Within quantum mechanics the energy E of a system of n interacting particles may be calculated, neglecting relativistic effects, by solving the time-independent Schrödinger equation,

$$\hat{H}\Psi(\mathbf{r}_1, \mathbf{r}_2, \mathbf{r}_3, \ldots, \mathbf{r}_n) = E\Psi(\mathbf{r}_1, \mathbf{r}_2, \mathbf{r}_3, \ldots, \mathbf{r}_n) \tag{5.1}$$

where $\hat{H}$ is the Hamiltonian operator and Ψ is the many-body wavefunction of the particular system. For a solid, Ψ is a function of the coordinates **r** of the atomic nuclei and electrons, and the Hamiltonian operator contains terms for the kinetic energy for all electrons, the kinetic energy for all nuclei, the interelectronic repulsion energy, the internuclear repulsion energy, and the energy for Coulombic interactions between electrons and nuclei. However while the Schrödinger equation can be solved exactly for the one-electron hydrogen atom, for more complex systems approximations must be made.

5.2.2 Born-Oppenheimer Approximation

One important approximation made is the Born-Oppenheimer approximation[189] which supposes that nuclei are essentially static over the period of time that electrons move around them. This allows the nuclear and electronic degrees of freedom to be separated such that the wavefunction is factorised into two parts; one a function of the position of the nuclei, and the other a function of the position of the electrons. In principal, the Born-Oppenheimer approximation allows one to calculate the electronic wavefunction and subsequent energy for all possible fixed locations of the nuclei.

5.2.3 The Variational Principle

Evaluations of the energy and wavefunction of the system may be made using the variational principle which states that the average total energy $E[\Psi_{approx}]$ for any initial guess of the wavefunction, Ψ_{approx}, will be greater than or equal to the true ground state energy, that is

$$E[\Psi_{approx}] \geq E_0. \tag{5.2}$$

Introducing parameters on which the wavefunction is dependent, and varying them to give the minimum energy, thus gives the best approximate wavefunction.

5.2.4 The Hohenberg-Kohn Theorems

In 1964 Hohenburg and Kohn[46] proposed the two Hohenburg-Kohn theorems which relate the ground state properties of a many-electron system to the electron density $\rho(\mathbf{r})$. This allows the many-body problem of N electrons with $3N$ spatial coordinates to be reduced to a problem of just 3 spatial coordinates. The first theorem states that the ground state electron density uniquely determines the external potential and vice versa, demonstrating that $\rho(\mathbf{r})$ uniquely determines the Hamiltonian. Thus, given a ground state density, $\rho_0(\mathbf{r})$, it is possible, in principle, to calculate the corresponding ground state wavefunction $\Psi_0(\mathbf{r}_1, \mathbf{r}_2 \ldots \mathbf{r}_n)$. The second theorem is an expression of the variational principle and states that given a positive trial density $\rho_t(\mathbf{r})$, subject to the constraint that $\int \rho_t(\mathbf{r}) d\mathbf{r} = N$, that $E[\rho_t] \geq E_0$. Taken together, these two theorems lead to the fundamental statement of density functional theory, namely

$$\frac{\delta}{\delta\rho(\mathbf{r})}\left[E[\rho] - \mu\left(\int \rho(\mathbf{r}) d\mathbf{r} - N\right)\right] = 0, \tag{5.3}$$

where μ is a Lagrange multiplier and corresponds to the increase in energy of the system on adding one more electron to it. When the system is in its ground state this is a constant, independent of $\mathbf{r}$. $E[\rho(\mathbf{r})]$ is a universal functional i.e. independent of

the external potential of the particular system, but its form remains unknown.

5.2.5 The Kohn-Sham Equations

In order to evaluate the energy functional, Kohn and Sham showed that the system of N interacting electrons in a static external potential can be represented by a system of N non-interacting electrons, which have a density ρ, moving in an effective potential[47]. The exact ground state energy functional can then be represented by the sum of the different contributions to the energy of the system

$$E^{KS}[\rho(\mathbf{r})] = T_{KS}[\rho(\mathbf{r})] + E_H[\rho(\mathbf{r})] + E_{ext}[\rho(\mathbf{r})] + E_{XC}[\rho(\mathbf{r})], \tag{5.4}$$

where $T_{KS}[\rho(\mathbf{r})]$ is the kinetic energy of the reference system of non-interacting electrons, $E_{ext}[\rho(\mathbf{r})]$ is the energy due to the interaction of electrons with the external potential and $E_H[\rho(\mathbf{r})]$ is the Hartree energy. $E_{XC}[\rho(\mathbf{r})]$, the only unknown, is the exchange-correlation functional which is the sum of a small component of unknown kinetic energy, i.e. the difference between the true kinetic energy and the kinetic energy of the system of non-interacting electrons, and the exchange-correlation energy potential. The ground state may then be found by minimising the functional derivative of the Kohn-Sham energy functional in accordance with the constraint of the second Hohenberg-Kohn theorem, namely

$$\frac{\delta E^{KS}}{\delta \rho(\mathbf{r})} = \frac{\delta T_{KS}}{\delta \rho(\mathbf{r})} + V_H(\mathbf{r}) + V_{ext}(\mathbf{r}) + V_{XC}(\mathbf{r}) = \mu, \tag{5.5}$$

where $V_{XC}(\mathbf{r})$ is the derivative of $E_{XC}[\rho(\mathbf{r})]$. This is done by solving the effective one-electron Schrödinger equation

$$\left[-\frac{\hbar}{2m}\nabla^2\psi(\mathbf{r}) + V(\mathbf{r})\right]\psi_n(\mathbf{r}) = \epsilon_n\psi_n(\mathbf{r}), \tag{5.6}$$

where

$$V(\mathbf{r}) = V_H(\mathbf{r}) + V_{ext}(\mathbf{r}) + V_{XC}(\mathbf{r}). \tag{5.7}$$

This yields orbitals that reproduce the charge density $\rho(\mathbf{r})$ of the original interacting system via

$$\rho(\mathbf{r}) = \sum_{n}^{occ} |\psi_n(\mathbf{r})|^2. \tag{5.8}$$

Thus the problem of solving the original Schrödinger equation or of minimising $E[\rho(\mathbf{r})]$ is reduced to approximating the form of $V_{XC}(r)$ and solving a set of non-interacting equations, the Kohn-Sham equations 5.6-5.8, until the self-consistent ground state density is found. The Hellmann-Feynman[190,191] theorem can then be used to calculate forces from the derivative of the total energy with respect to the nuclear coordinates.

5.2.6 Spin-Density Functional Theory

Spin-density functional theory[192,46,47] extends the DFT formalism to include the electron spins by expressing the electron wavefunction as a spinor, a 2×1 vector, with entries for the up- and down-spin states

$$\psi_n = \begin{pmatrix} \psi_{n\uparrow}(\mathbf{r}) \\ \psi_{n\downarrow}(\mathbf{r}) \end{pmatrix}. \tag{5.9}$$

The electron density is then given by

$$n(\mathbf{r}) = \sum_{n,\nu}^{occ} |\psi_{n\nu}(r)|^2, \tag{5.10}$$

and the 2×2 spin density matrix

$$\rho_{\nu\nu'}(\mathbf{r}) = \sum_{n}^{occ} \psi_{n\nu}(\mathbf{r})\psi^*_{n\nu'}(\mathbf{r}), \tag{5.11}$$

becomes the central quantity to be solved self-consistently.

5.2.7 Exchange Correlation Functionals

The reliability of DFT calculations is heavily dependent on the approximation of the exchange-correlation functional used. The simplest approximation is the local-density approximation (LDA) [193,192,194,195,196], in which the exchange-correlation functional for a real inhomogoenous system is approximated using the exchange energy density, ε_{XC}, from a homogeneous free electron gas with comparable density such that

$$E_{XC}[\rho] \approx \int \rho(\mathbf{r})\varepsilon_{XC}\rho(\mathbf{r})d\mathbf{r} \tag{5.12}$$

This approximation was implemented by a number of different groups [193,192,194] producing similar results and the resulting functionals are known collectively as the LDA functionals. The LDA tends to overestimate the correlation energy and underestimate the exchange energy but these two errors typically cancel each other. It does however tend to predict closer-packed structures to be more stable as a result of favouring metallic bonding over ionic bonding which can lead to the underestimation of lattice parameters and the overestimation of cohesive energies, phonon frequencies, and elastic moduli. Improving upon the LDA is non-trivial but various types of generalised gradient approximations (GGA) have been developed [197,198,199] which take into account the density and its gradient. One such example is the PBE functional [200].

5.2.8 Computational Details

DFT calculations were performed with the plane wave Vienna *ab-initio* simulation package (VASP) [201,202] using the all-electron projector-augmented wave (PAW) method. For spin-polarised exchange and correlation potentials the Perdew-Burke-

Ernzerhof (PBE)[200] parameterisation of the generalised gradient approximation (GGA) was used. The Brillouin zone was sampled using the Monkhorst-Pack scheme[203] and the tetrahedron integration method[204]. *k*-point grids were chosen such that a convergence in the total energy of at least 1 meV/atom was achieved. The cut-off energy for the plane wave expansion was fixed at 350 eV for all calculations. For relaxation of the internal coordinates the forces were converged to at least 1 meV/Å.

5.3 The Tight-Binding (TB) Approximation

The tight-binding approximation provides a first step in coarse-graining *ab initio* DFT to interatomic potentials such as BOPs. The assumption is made that electrons are tightly bound to each atom and are only weakly influenced by the surrounding atoms. Each one-electron wavefunction is therefore assumed to be similar to the atomic orbital of the free atom to which the electron belongs, and electrons are allowed to hop between these atomic-like orbitals. In this way the electronic wavefunction is expanded using the linear combination of atomic orbitals (LCAO)[205] approach. The tight-binding approximation is valid for covalently-bonded materials and the transition metals with valence d electrons in which electrons are strongly localised and the bandwidth is small.

5.3.1 Derivation of nonmagnetic TB Binding Energy

A systematic procedure for formulating a tight-binding model was given by Slater and Koster in 1954[205] whereby the wavefunction for a periodic lattice of N atoms is written using the LCAO approach, and following Bloch's Theorem for periodic

materials[206], as

$$\psi_{\mathbf{k}}^{(n)}(\mathbf{r}) = N^{-1} \sum_{\mathbf{R}} \sum_{i\alpha} c_{i\alpha}^{(n)} e^{i\mathbf{k}.\mathbf{R}_i} \psi_\alpha(\mathbf{r} - \mathbf{R}_i - \mathbf{R}), \tag{5.13}$$

where the atomic-like orbitals α positioned at atomic sites i are defined by spatial coordinates with respect to a fixed origin, (**r** - $\mathbf{R}_i$), $c_{i\alpha}^{(n)}$ are expansion coefficients, **k** are the wavevectors of the wavefunction and **R** is a lattice vector of the crystal. Correspondingly, the k-space Schrödinger equation is written as

$$\hat{H}\psi_{\mathbf{k}}^{(n)}(\mathbf{r}) = E_{\mathbf{k}}^{(n)}(\mathbf{r})\psi_{\mathbf{k}}^{(n)}(\mathbf{r}), \tag{5.14}$$

and the Fourier transformed k-space Hamiltonian matrix elements and overlap matrix elements may be written, respectively, as

$$H_{i\alpha j\beta}(\mathbf{k}) = \sum_{\mathbf{R}} H_{i\alpha j\beta}(\mathbf{R}_i - \mathbf{R}_j - \mathbf{R}) e^{i\mathbf{k}.\mathbf{R}} \tag{5.15}$$

and

$$S_{i\alpha j\beta}(\mathbf{k}) = \sum_{\mathbf{R}} S_{i\alpha j\beta}(\mathbf{R}_i - \mathbf{R}_j - \mathbf{R}) e^{i\mathbf{k}.\mathbf{R}}. \tag{5.16}$$

The TB secular equation, to be solved self-consistently, is then

$$\sum_{i\alpha} \left[H_{i\alpha j\beta}(\mathbf{k}) - E^{(n)}(\mathbf{k}) S_{i\alpha j\beta}(\mathbf{k}) \right] c_{i\alpha}^{(n)}(\mathbf{k}) = 0. \tag{5.17}$$

The eigenvalue solutions of this form the TB band structure which can be integrated to find the band energy, the electronic energy of all the occupied bands of the system, for a particular band-filling.

The Slater-Koster Approximations

At the heart of the TB approximation is the process of constructing simplified Hamiltonian and overlap matrices which makes solving the secular equation easier. Each Hamiltonian matrix elements describes the interaction between three components: a potential and two orbitals. The assumption is made that the most important interactions for a given atom are with other nearby atoms. The two-centre approximation is made such that three-centre terms, that is elements in which the potential and orbitals are centred on three different atomic sites, are ignored. This is a reasonable assumption because the leading three-centre correction terms to the energy are of second-order in the overlap matrix[207]. Additionally a nearest neighbour approximation can be made in which two-centre terms between atomic sites which are beyond, for example, first, second or third nearest neighbours are disregarded. The resulting Hamiltonian matrix is composed of one-centre on-site matrix elements, along its diagonal, and two-centre off-diagonal matrix elements, the hopping integrals, so-called because they are related to the probability of an electron hopping from one orbital to another. Furthermore the on-site matrix elements can be approximated as atomic quantities by ignoring their dependence on the crystal field i.e. the presence of all the other atoms in the system. A further assumption often made is to neglect the non-orthogonality of the atomic basis set because the leading corrections to the energy are also second-order in the overlap matrix elements $S_{i\alpha j\beta}$[207]. Within an orthogonal TB model the overlap matrix elements are taken to be 1 for $i\alpha = j\beta$ and 0 otherwise, i.e. the overlap matrix **S** becomes the unit matrix.

Cohesion within the transition metals is dominated by the electrons within the narrow d-band, while in contrast the sp-band is wide and the free-electron-like s and p electrons do not contribute significantly to structural differences. In TB models for transition metals the s and p electrons are therefore typically neglected. With 5 d orbitals on each site it would therefore be expected that there are 25 hopping

integrals to be described in a d-valent model. However within the two-centre approximation Slater and Koster[205] showed that this number can be reduced to just 3 special hopping integrals, the bond integrals $\beta_\lambda(\mathbf{r})$, by considerations of symmetry, rotating the coordinate system such that the z-axis lies along the direction of the bond in order to preserve angular momentum about the bond axis. Therefore instead of being calculated explicitly the Hamlitonian matrix elements are calculated from the parameterised bond integrals, dependent on the distance between atoms, and a set of cosine functions which describe the angular variation of the hopping integrals between different combinations of orbitals. The bond integrals are typically parameterised with respect to data taken from DFT calculations. The functional form of the bond integrals used in the TB models in this thesis and an overview of the parameterisation process is given in Sec. 7.2.

Formulation Of The Binding Energy

There are two types of TB model, one in which the binding energy is given in terms of the bond energy and another in which it is given in terms of the band energy[30]. Notably Sutton *et al.*[30] and Foulkes[31] showed that the TB bond model may be derived as a second-order expansion of DFT with respect to charge and magnetic fluctuations. The TB bond model is used in this work for a number of reasons. Firstly the traditional TB band model does not fulfil a variational principle and as a result it violates the frozen potential force theorem[208,209], which states that there must be no contribution to the force on an atom arising from the self-consistent redistribution of electronic charge concomitant with a virtual atomic displacement[96]. In contrast because the TB bond model is derived from a second-order expansion of the Kohn-Sham total energy in DFT it does fulfil a variational principle and therefore is consistent with the force theorem in the approximation that self-consistency is adequately described by local charge neutrality (LCN)[30].

Secondly within the TB bond model the binding energy can be written in a more intuitive and transparent form in which the various energy contributions have clear physical meanings and may be analysed separately with regards to their role in the formation of chemical bonds. These contributions are defined with respect to nonmagnetic free atoms the energy of which is given by

$$U_{at} = \sum_{i\alpha} E_{i\alpha}^{(at)} N_{i\alpha}^{(0)} - \frac{1}{2} \sum_{i\alpha j\beta} J_{i\alpha j\beta} N_{i\alpha}^{(0)} N_{j\beta}^{(0)}, \tag{5.18}$$

in which the second term is the double-counting Coulomb energy of the free atom. The binding energy within the TB bond model for a nonmagnetic system may then be written as

$$U_B^{TBBM} = U_{bond} + U_{trans} + U_{rep} + U_C + U_{ext}, \tag{5.19}$$

where U_{bond} is the bonding energy, U_{trans} is the electron transfer energy, U_{rep} is the repulsive energy, U_C is the Coulomb energy and U_{ext} is the external potential[34].

Bond energy

The bond energy can be expressed in two ways which are equivalent but which offer differing perspectives on the formation of chemical bonds. The onsite representation requires the local DOS at each atom, $n_{i\alpha}(E)$ while the intersite representation is expressed in terms of the bond order $\Theta_{i\alpha j\beta}$, or the density matrix $\rho_{i\alpha j\beta}$, which measure the strength of the bond between $i\alpha$ and $j\beta$. The bond order and density matrix are related by a factor of two and are given by the sum over all occupied states

$$\Theta_{i\alpha j\beta} = 2\rho_{i\alpha j\beta} = 2 \sum_{n}^{occ} c_{i\alpha}^{*(n)} c_{j\beta}^{(n)}. \tag{5.20}$$

Within the intersite representation the band energy is given as a sum over all pairs of atoms of the product of the bond order, or density matrix, with the Hamil-

tonian

$$U_{band}^{intersite} = \sum_{i\alpha j\beta} \Theta_{i\alpha j\beta} \mathbf{H}_{j\beta i\alpha} = \sum_{i\alpha j\beta} 2\rho_{i\alpha j\beta} \mathbf{H}_{j\beta i\alpha}. \tag{5.21}$$

The bond energy may then be given, using only the off-diagonal elements of the bond order, or density matrix, and the relevant hopping integral from the Hamiltonian, by

$$U_{bond}^{intersite} = \sum_{i\alpha j\beta, j\neq i} \Theta_{i\alpha j\beta} \mathbf{H}_{j\beta i\alpha} = \sum_{i\alpha j\beta, j\neq i} 2\rho_{i\alpha j\beta} \mathbf{H}_{j\beta i\alpha}. \tag{5.22}$$

Alternatively, within the onsite representation the local DOS

$$n_{i\alpha}(E) = \sum_{n} |c_{i\alpha}^{(n)}|^2 \delta(E - \epsilon_n), \tag{5.23}$$

is used to rewrite the band energy as

$$U_{band}^{onsite} = 2 \sum_{i\alpha} \int^{E_F} E n_{i\alpha}(E) dE. \tag{5.24}$$

The bond energy is then expressed by subtracting off the diagonal elements of the Hamiltonian, the on-site levels, from the band energy as

$$U_{bond}^{onsite} = 2 \sum_{i\alpha} \int^{E_F} (E - E_{i\alpha}) n_{i\alpha}(E) dE, \tag{5.25}$$

where $E_{i\alpha}$ is used to denote the on-site levels $H_{i\alpha i\alpha}$ and the prefactor 2 accounts for spin degeneracy. The local DOS depends on the crystal structure and the Fermi level E_F depends on the number of valence electrons. The onsite representation of the bond energy forms the basis of the bond-order potential expansion of the bond energy which will be discussed in Section 5.4.

Electron transfer energy

The electron transfer energy U_{trans} is the energy associated with the transfer of electrons from their reference state, the nonmagnetic free atoms, to their actual occupations. It is given by

$$U_{trans} = \sum_{i\alpha} E^{(0)}_{i\alpha} q_{i\alpha}, \tag{5.26}$$

where $q_{i\alpha}$ is the charge associated with orbital $|i\alpha\rangle$. For neutral systems this contribution is just the conventional promotion energy required to form hybrid orbitals from free atomic states. Within a d-valent TB model the 5 d-orbitals are energetically degenerate and the promotion energy is therefore zero.

Preparation energy

The preparation energy, the energy required to prepare the atomic-like orbitals from the nonmagnetic free atoms, is be given by

$$U_{prep} = \sum_{i\alpha} (E^{(0)}_{i\alpha} - E^{(at)}_{i\alpha}) N^{(0)}_{i\alpha}. \tag{5.27}$$

This preparation energy is contributed to by two effects, a shift of the atomic levels due to the overlap of atomic orbitals and a shift due to the renormalisation of the atomic-like local orbitals[207,210]. For transition metals the latter term tends to be larger because d-orbital overlap tends to be small[34]. In practice the preparation energy will be included within the repulsive energy U_{rep}.

External Potential Energy

The nonmagnetic external energy is given by

$$U_{ext} = \sum_{i\alpha} V_{i\alpha} N_{i\alpha} \tag{5.28}$$

where it is assumed that

$$V_{i\alpha}^{i'\alpha'} = V_{i\alpha}\delta_{i\alpha i'\alpha'} \tag{5.29}$$

Within the simple model developed in this work the external potential is set to zero.

Repulsive energy

The repulsive energy U_{rep} is included to account for energy contributions due not only to crystal field effects and overlap repulsion but also exchange-correlation and nuclear-nuclear electrostatic effects which are neglected within the TB Hamiltonian. It is independent of the electronic state of the system and is therefore a function only of the atomic positions. It is often approximated by a simple pairwise function and some justification for modelling these electrostatic and exchange-correlation terms with a pair potential has been given[96]. More complex many-body forms can also be used if quantitative predictions of defect behaviour are required[211,212,213]. The functional form of U_{rep} used in the models presented in this thesis is discussed in Sec. 7.2.

Local Charge Neutrality

For metals the assumption of local charge neutrality (LCN) is reasonable given that the screening of atoms is very efficient with any excess charge associated with an atom being neutralised[214]. The assumption of charge neutrality also leads to an internally consistent picture of the heats of formation of transition metal alloys[207]. Within a locally charge neutral model the Coulomb energy U_C is zero and the onsite levels $E_{i\alpha}$ are adjusted self-consistently[97] such that

$$\sum_{\alpha} q_{i\alpha} = 0, \tag{5.30}$$

for all atoms i. Furthermore within a locally charge neutral system the electron transfer energy U_{trans} reduces to the conventional promotion energy given by

$$U_{prom} = \sum_{i\alpha} E^{(0)}_{i\alpha} q_{i\alpha}. \tag{5.31}$$

Within the d-valent, two-centre, orthogonal TB bond model[30], and with the on-site levels adjusted to fulfil the condition of local charge neutrality the NM binding energy therefore reduces to

$$U_B = U_{bond} + U_{emb} + U_{rep}, \tag{5.32}$$

where U_{emb} is an attractive embedding energy introduced to account for the contribution of the s electrons and sd hybridisation that are neglected in the d-valent model.

Self-Consistency

Because the TB bond model is derived from a second-order expansion of DFT and therefore fulfils a variational principle, the self-consistent state may be obtained by minimising the binding energy with respect to the onsite energy levels

$$\frac{\partial U_B}{\partial E_{i\alpha}} = 0. \tag{5.33}$$

Forces

The forces acting on an atom l in, for example, the z-direction can be obtained by differentiating the binding energy with respect to the z-coordinate of atom l, z_l. Calculating the derivative of the repulsive energy is trivial and for the bonding energy, once the onsite levels have been calculated self-consistently, the force on

atom l may be calculated using the Hellman-Feynman Theorem[190,191] as

$$\mathbf{F}_l^{Bond} = \sum_{i\alpha j\beta, i\neq j} \Theta_{i\alpha j\beta} \nabla_l H_{j\beta i\alpha}. \tag{5.34}$$

5.3.2 Derivation of Magnetic TB Binding Energy

The Stoner model, which has been shown to work well for $3d$ transition metals[215,216], can be used to extend the TB approximation to include magnetism[215,51,34]. In collinear magnetic systems electrons may have their spins ν aligned parallel $\uparrow$ or anti-parallel $\downarrow$ to the local magnetic moment. The Stoner model introduces magnetism by adjusting the local on-site energies such that atoms with electrons with spins parallel to the local moment have their on-site energies lowered while atoms with electrons with spins anti-parallel to the local moment have their on-site energies raised. That is

$$E_{i\alpha\nu} = E_{i\alpha}^{(0)} \pm \frac{1}{2} I_d m_i, \tag{5.35}$$

where ν is the electron spin, m_i is the magnetic moment on atom i and I_d is the Stoner integral. The magnetic moment, m_i, is given by the difference in the number of $\uparrow$ and $\downarrow$ spin electrons on site i. The exchange energy U_X is then given by

$$U_X = -\frac{1}{4} \sum_i I_d m_i^2. \tag{5.36}$$

where the assumption that only the onsite Stoner integrals are non-zero has been made such that $I_d \mathbf{m}_i \mathbf{m}_j = 0$ for $i \neq j$. The assumption that the Stoner integral is independent of volume[51,215] and crystal structure is also made.

Within the d-valent, two-centre, orthogonal TB bond model[30], and with the onsite levels adjusted to fulfil the condition of local charge neutrality the magnetic

binding energy functional can therefore be written as

$$U_B = U_{bond} + U_{emb} + U_{rep} + U_X. \tag{5.37}$$

Within the magnetic TB formalism a local coordinate system is chosen for each atom and orbital to lie parallel to the direction of the magnetic moment such that

$$\mathbf{e}_z = \mathbf{s}_{i\alpha} \tag{5.38}$$

with

$$\mathbf{s}_{i\alpha} = \frac{\mathbf{m}_{i\alpha}}{m_{i\alpha}}. \tag{5.39}$$

The local magnetic moment may then be obtained from the local DOS as

$$\mathbf{m}_{i\alpha} = (N_{i\alpha\uparrow} - N_{i\alpha\downarrow})\mathbf{s}_{i\alpha} = m_{i\alpha}\mathbf{s}_{i\alpha} \tag{5.40}$$

The bonding energy is written as the sum of the bonding energies of the two spin bands namely

$$U_{bond} = \sum_{i\alpha} \int^{E_F} (E - E_{i\alpha\uparrow}) n_{i\alpha\uparrow}(E) dE + \sum_{i\alpha} \int^{E_F} (E - E_{i\alpha\downarrow}) n_{i\alpha\downarrow}(E) dE, \tag{5.41}$$

where $E_{i\alpha\uparrow} = E_{i\alpha\uparrow\uparrow}$ and $E_{i\alpha\downarrow} = E_{i\alpha\downarrow\downarrow}$

With the inclusion of the exchange energy it can be seen that an increase in magnetic moment leads to a lowering of the binding energy if the change in U_X is larger than the corresponding decrease in the bonding energy caused by the associated increase of the kinetic energy of the electrons. This model can also be extended to include non-collinear magnetic systems[217,58,34].

5.3.3 Computational Details

Details of the form of the bond integrals, the repulsive energy function and the TB model parameters are given in Chapters 7 and 8. TB calculations were performed using the BOPfox code[218]. The Brillouin zone was sampled using the Monkhorst-Pack scheme (such that a convergence in the binding energy of at least 1 meV/atom was achieved) and integrated using the tetrahedron method[204]. Local Charge Neutrality (LCN) was enforced such that the magnetic moments were found self-consistently under the constraint that the final atomic charges were numerically zero.

5.4 Bond-Order Potentials (BOP)

5.4.1 Introduction

The computationally most demanding part of a TB calculation is the diagonalisation of the Hamiltonian matrix. To circumvent this step, the TB electronic structure can be coarse-grained via the moments theorem[219] and the Lanczos algorithm[220] used to reconstruct the local DOS $n_{i\alpha}(E)$ from its moments. The moments are functions of the positions and types of atoms close to atom i and in this way a direct connection between the electronic structure and the local topology and coordination of the system is made. This process forms the basis of a number of different, closely related, real-space linear-scaling methods notably the recursion method for solving the TB approximation[221,222], in which the local DOS is approximated as a continued fraction, and numerical BOP[32,223,97] which extends the recursion method such that the forces may be evaluated approximately. More recently the analytic BOP[33,34] method has been derived from a moments-based perturbation expansion of the continued fraction approximation in terms of Chebyshev polynomials of the second kind. While the recursion method and numerical BOP rely on numerical in-

tegration of the local DOS, which is computationally slow, within analytic BOP the bond energy may be integrated analytically and the forces calculated exactly. Analytic BOP can be considered to be a systematic extension of the Finnis-Sinclair[29] (FS) potential to include higher moments which sample the crystal structure, and therefore bonding, further out into a material. BOPs retain the quantum mechanical character of the TB model and have a number of features which make them advantageous over other semi-empirical potentials such as the FS, EAM and MEAM potentials. For example they explicitly include the valence dependence of bond formation and, as a result, they can account for charge transfer and magnetism in a physically transparent way[32,33,34]. Furthermore, the angular characteristic of bonding is retained within the BOP formalism. Recent developments have included a method for guaranteeing a strictly positive DOS[224] and the first non-collinear magnetic analytic BOP calculations[225].

Within a BOP calculation the most computationally expensive process is the evaluation of the moments. Therefore it is desirable for the important properties of a given system, such as the DOS, binding energy and magnetic moments, to converge as a function of the number of moments as quickly as possible. Fortunately it has been shown that relatively few moments are required to capture important structural trends across the periodic table. For example, with respect to the unsaturated bonds in close-packed transition metals, the subtle bcc-fcc energy difference can be captured by expansions which include at least the 4^{th} moment[120] while the fcc and hcp structure types may be distinguished by expansions which include at least the 6^{th} moment[102,5]. Furthermore, it has been shown that an analytic BOP with 6-moments is able to predict the different ferromagnetic moments of the bcc, fcc and hcp phases of $3d$ Fe[33] and, more recently, Ford *et al.*[226] showed that a 9-moment magnetic analytic BOP was capable of reproducing the behaviour of the local magnetic moments in Fe defect structures. A numerical BOP with 9 moments

was applied by Mrovec *et al.*[227] to provide an accurate description of the electronic and magnetic structure of Fe at 0 K. This reproduced the behaviour of lattice defects such as dislocations, which induce changes in bond lengths, bond angles and local magnetic moments. While Seiser *et al.* showed that 6 moments are sufficient to reproduce the subtle trend from $A15 \rightarrow \sigma \rightarrow \chi$ for TCP phases across the 4d and 5d periods it was found that 12 moments or more are required to resolve very small energy differences that distinguish some structures[228]. The convergence of elastic constants may require more than 30 moments[229].

5.4.2 Moments Theorem

The moments of the local TB DOS may be written as

$$\mu_{i\alpha\nu}^{(n)} = \int E^n n_{i\alpha\nu}(E) dE. \tag{5.42}$$

The lower order moments have intuitive physical meanings, for example,

$$\begin{aligned}
\mu^{(0)} &= \text{total number of states} \\
\mu^{(1)}/\mu^{(0)} &= \text{the centre of gravity of the DOS} \\
\mu^{(2)}/\mu^{(0)} &= \text{root mean squared width of the DOS} \\
\mu^{(3)}/\mu^{(0)} &= \text{a reflection of the skewness of the DOS} \\
\mu^{(4)}/\mu^{(0)} &= \text{a reflection of the bimodality of the DOS.}
\end{aligned} \tag{5.43}$$

For an orthonormal basis the moments of the local DOS may be evaluated without explicit knowledge of the DOS by making use of Cyrot-Lackmann's moments theorem[219] which relates the moment of order n to the self-returning electronic

hopping paths of length n that start and end on orbital $|i\alpha\rangle$,

$$\begin{aligned} \mu_{i\alpha\nu}^{(n)} &= \langle i\alpha| \hat{H}^n |i\alpha\rangle \\ &= \sum_{j\beta\nu k\gamma\nu,\ldots} \hat{H}_{i\alpha\nu j\beta\nu}\hat{H}_{j\beta\nu k\gamma\nu}\hat{H}_{k\gamma\nu\ldots}\ldots\hat{H}_{\ldots i\alpha\nu}, \end{aligned} \tag{5.44}$$

where $H_{i\alpha j\beta}$ is the TB Hamiltonian matrix element $\langle i\alpha| \hat{H} |j\beta\rangle$ between orbitals $i\alpha$ and $j\beta$.

The moments theorem therefore relates the local DOS, $n_{i\alpha}(E)$, to the products of the matrix elements of the Hamiltonian operator $\hat{H}_{i\alpha j\beta}$, reducing the task of calculating the moments of the local DOS to a series of matrix multiplications and establishing a direct connection between the electronic structure of orbital α on atom i and the crystal structure environment of atom i. Higher moments represent longer hopping paths which sample the atomic environment further away from $i\alpha$ and an infinitely large set of moments would exactly reproduce the TB DOS. As we will see this expression can therefore be evaluated within real-space without solving any Schrödinger equations and allows the relative influences of successive neighbour shells to be studied systematically.

5.4.3 The Recursion Method

The recursion method is an alternative, but mathematically equivalent, way of relating the electronic structure to the crystal structure[221]. The TB Hamiltonian may be transformed into a tridiagonal matrix by using the Lanczos recursion algorithm[220]. Starting from the atomic orbital $|u_0\rangle = |i\alpha\rangle$ a suitable basis set can be recursively generated from on-site matrix elements a_n and nearest-neighbour hopping matrix

elements b_n, given by

$$\begin{aligned} a_n &= \langle u_n \mid \hat{H} \mid u_n \rangle \qquad \text{and} \\ b_n &= \langle u_n \mid \hat{H} \mid u_{n-1} \rangle = \langle u_{n-1} \mid \hat{H} \mid u_n \rangle, \end{aligned}$$

using the following recursion relation

$$b_{n+1} \mid u_{n+1} \rangle = (\hat{H} - a_n) \mid u_n \rangle - b_n \mid u_{n-1} \rangle. \tag{5.45}$$

The corresponding Hamiltonian is then given by

$$\langle u_n \mid \hat{H} \mid u_m \rangle = \begin{vmatrix} a_0 & b_1 & 0 & 0 & \ddots \\ b_1 & a_1 & b_2 & 0 & \ddots \\ 0 & b_2 & a_2 & b_3 & \ddots \\ 0 & 0 & b_3 & a_0 & \ddots \\ \ddots & \ddots & \ddots & \ddots & \ddots \end{vmatrix}. \tag{5.46}$$

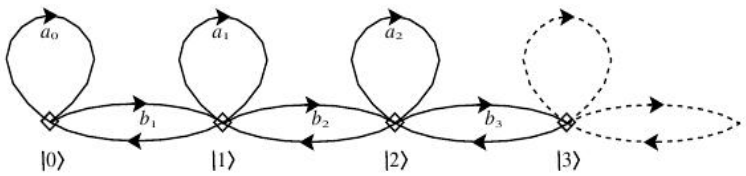

Figure 5.1: The recursion chain: a semi-infinite 1-dimensional linear chain, which represents the tridiagonal Hamiltonian. It can be seen that only nearest neighbours, represented by the recursively generated orbitals, $\mid u_n \rangle$, are coupled. The recursion coefficients, a_n and b_n, which couple the orbitals are coefficients in a continued fraction expansion of the Green's function, $G_{i\alpha i\alpha}$, given in equation 5.52. Taken from Ref. 230.

This tridiagonal Hamiltonian can be understood as a semi-infinite one-dimensional linear chain as is illustrated in Figure 5.1 and it is then evident that the n^{th} moment is given, following Eq. 5.44, as the sum of all possible self-returning paths of length

n which start on $|u_0\rangle$, namely

$$\mu_{i\alpha}^{(n)} = \langle u_0 \mid \hat{H}^n \mid u_0 \rangle \tag{5.47}$$

For example for $n = 0, 1, 2, 3$ and 4 the following expressions are obtained

$$\begin{aligned}
\mu_{i\alpha}^{(0)} &= 1, \\
\mu_{i\alpha}^{(1)} &= a_0, \\
\mu_{i\alpha}^{(2)} &= a_0^2 + b_1^2, \\
\mu_{i\alpha}^{(3)} &= a_0^3 + 2a_0 b_1^2 + a_1 b_1^2, \\
\mu_{i\alpha}^{(4)} &= a_0^4 + 3a_0^2 b_1^2 + 2a_0 a_1 b_1^2 + a_1^2 b_1^2 + b_1^2 b_2^2 + b_1^4.
\end{aligned} \tag{5.48}$$

Taking the centre of gravity as the reference energy these relations may be inverted to read[97]

$$\begin{aligned}
a_0 &= 0, \\
a_1 &= \frac{\mu_3}{\mu_2}, \\
b_1^2 &= \mu_2, \\
b_2^2 &= \frac{\mu_4}{\mu_2} - (\frac{\mu_3}{\mu_2})^2 - \mu_2.
\end{aligned} \tag{5.49}$$

Construction of the DOS within the recursion method

To calculate the bond energy of a system of atoms requires the integration of the DOS. Within the recursion method the DOS may be constructed from the moments of the DOS by making use of the relation

$$n_{i\alpha}(E) = -\frac{1}{\pi}\mathrm{Im}G_{i\alpha i\alpha}(E), \tag{5.50}$$

where $G_{i\alpha i\alpha}$ are the diagonal elements of the Green's function

$$\hat{G} = (E\hat{1} - \hat{H})^{-1}. \tag{5.51}$$

These Green's function elements can be expressed as a continued fraction[221]. For example, for a starting state G_{00}

$$G_{i\alpha i\alpha} = G_{00} = \cfrac{1}{(E-a_0) - \cfrac{b_1^2}{(E-a_1) - \cfrac{b_2^2}{(E-a_2) - \cfrac{b_3^2}{(E-a_3) - \ddots}}}}, \tag{5.52}$$

where a_n and b_n are the recursion coefficients of the tridiagonal Hamiltonian, which are directly related to the moments of the DOS through the relationships given in equations 5.48 and 5.49.

Calculating this continued fraction to an infinite number of levels is analogous to using an infinite number of moments, which would exactly reproduce the TB DOS. However in practice the continued fraction is truncated after a certain number of levels n so that, for example, for $m > n$, $a_m = a_\infty$ and $b_m = b_\infty$. Within the recursion method the approximate local DOS obtained from the truncated continued fraction could then be integrated numerically to calculate the bond energy. This approach forms the basis of the numerical BOP method. The advantages of such approaches are that the calculation of the DOS from the Green's function is performed in real-space and scales linearly with the system size. However the primary drawbacks of numerical BOPs are that the Hellmann-Feynman forces converge too slowly for dynamic simulations to be practical.

Within the analytical BOP method once an expression for the local DOS has been obtained it is integrated analytically. There are two types of analytic BOP; bond-based and atom-based. In bond-based analytic BOP the continued fraction

(equation 5.52) is terminated after three 'levels' or, for symmetric eigenspectra with $a_n = 0$, 'poles'. b_3 can then be written in terms of b_1 and b_2, providing an expansion which uses only up to the fourth moment. This demonstrates good convergence and is suitable for describing the covalent bonds in sp-valent materials[231]. An alternative approach, which forms the basis of the atom-based analytic BOP method, is to use a constant terminator all the way along the Lanczos chain such that, for example, $a_n = a_\infty$ and $b_n = b_\infty$ for all n[33]. In this way the sum of the continued fraction can be evaluated analytically with the resultant semi-elliptical local DOS given by

$$n_{i\alpha}(E) = n_{i\alpha}(\epsilon)/2b_\infty, \tag{5.53}$$

where

$$n_{i\alpha}(\epsilon) = \frac{2}{\pi}\sqrt{1-\epsilon^2}, \tag{5.54}$$

and

$$\epsilon = \frac{E - a_\infty}{2b_\infty}. \tag{5.55}$$

It can be seen that this local DOS represents a single band of states between $\epsilon = \pm 1$ and $E = a_\infty \pm 2b_\infty$. Contact may be made here with the Finnis-Sinclair potentials which use the second-moment approximation, corresponding to choosing $a_\infty = a_0$ and $b_\infty = b_1$ so that the resultant bond energy is proportional to b_1 or $\sqrt{\mu_{i\alpha}^{(2)}}$[29]. In fact the lowest order approximation of the atom-based analytic BOP method is the second-moment approximation and it may therefore be thought of as a systematic extension of the FS potential to include higher moments.

5.4.4 Atom-Based Analytic BOP

Within atom-based analytic BOP the local DOS from equation 5.53 is expanded as

$$n_{i\alpha}(\epsilon) = n_{i\alpha}^{(0)}(\epsilon) + \delta n_{i\alpha}(\epsilon), \tag{5.56}$$

where $\delta n_{i\alpha}(\epsilon)$ is then expanded in terms of Chebyshev polynomials of the second kind $U_n(\epsilon)$[232]. This expansion may also be done using Chebyshev polynomials of the first kind forming the basis of the closely related kernel polynomial method[233,234] which will be referred to in Sec. 5.4.5. It may be shown that both expansions are equivalent, however Chebyshev polynomials of the second kind are the eigenstates of the semi-infinite constant Lanczos chain[221] and are therefore particularly well-suited to the systematic expansion of equation 5.53 beyond the second-moment approximation[33]. Chebyshev polynomials of the second kind are defined as

$$U_n(\epsilon) = \sum_{m=0}^{n} p_{nm}\epsilon^n. \tag{5.57}$$

where p_{nm} are expansion coefficients satisfying the recursion relation of Chebyshev polynomials of the second kind,

$$p_{(n+1)m} = 2p_{n(m-1)} - p_{(n-1)m}, \tag{5.58}$$

with $p_{nm} = 0$ if $m < 0$ or $m > n$.

The local DOS, including n_{max} exact moments, is then given by[33]

$$n_{i\alpha}(\epsilon) = \frac{2}{\pi}\sqrt{1-\epsilon^2}\left[\sum_{n=0}^{n_{max}} \sigma_{i\alpha}^{(n)} U_n(\epsilon)\right], \tag{5.59}$$

where the expansion coefficients $\sigma_{i\alpha}^{(n)}$ are given by

$$\sigma_{i\alpha}^{(n)} = \sum_{m=0}^{n} p_{nm} \hat{\mu}_{i\alpha}^{(m)}, \tag{5.60}$$

where $\hat{\mu}_{i\alpha}^{(m)}$ are the normalised moments of the local density of states

$$\hat{\mu}_{i\alpha}^{(m)} = \frac{1}{\left(2b_{i\alpha}^{(\infty)}\right)^{m}} \sum_{n=0}^{m} \binom{m}{n} (-1)^{n} a_{i\alpha}^{(\infty)n} \mu_{i\alpha}^{(m-n)}. \tag{5.61}$$

Within a simple linear approximation, Pettifor and Drautz[33] showed that the expansion coefficients, $\sigma_{i\alpha}^{(n)}$, can be expressed in terms of Lanczos recursion coefficients, $a_{ni\alpha}$ and $b_{ni\alpha}$,

$$\sigma_{i\alpha}^{(2n)} = \left(b_{ni\alpha}^{2} - b_{i\alpha}^{(\infty)2}\right) / b_{i\alpha}^{(\infty)2} \tag{5.62}$$

and

$$\sigma_{i\alpha}^{(2n+1)} = \left(a_{ni\alpha} - a_{i\alpha}^{(\infty)}\right) / b_{i\alpha}^{(\infty)} \tag{5.63}$$

for $m \geq 1$.

The asymptotic recursion coefficients $a_{i\alpha}^{(\infty)}$ and $b_{i\alpha}^{(\infty)}$ must be approximated and within this work the following identities are used[235]

$$a_{i\alpha}^{(\infty)} = (\epsilon_{max} + \epsilon_{min})/2, \tag{5.64}$$

$$b_{i\alpha}^{(\infty)} = (\epsilon_{max} - \epsilon_{min})/4, \tag{5.65}$$

where ϵ_{max} and ϵ_{min} are calculated from the maximum and minimum values of $a_{ni\alpha}$ and $b_{ni\alpha}$

$$\epsilon_{max} = a_{ni\alpha}^{max} + 2b_{ni\alpha}^{max}, \tag{5.66}$$

$$\epsilon_{min} = a_{ni\alpha}^{min} - 2b_{ni\alpha}^{max}. \tag{5.67}$$

The expansion of the local DOS in terms of the Chebyshev polynomials of the second kind can then be integrated analytically to obtain the bond energy and the number of electrons. However in practice these can be evaluated directly from the moments without calculating and integrating the DOS by using the response functions $\hat{\chi}$ defined as

$$\hat{\chi}_{(n)}\left(\phi_{F,i\alpha}\right) = \frac{1}{\pi}\left[\frac{\sin(n+1)\left(\phi_{F,i\alpha}\right)}{n+1} - \frac{\sin(n-1)\left(\phi_{F,i\alpha}\right)}{n-1}\right], \tag{5.68}$$

which are functions of the Fermi phase $\phi_{F,i\alpha}$

$$\phi_{F,i\alpha} = \cos^{-1}\left[\left(E_F - a_{i\alpha}^{(\infty)}\right)/b_{i\alpha}^{(\infty)}\right], \tag{5.69}$$

and which therefore introduce an explicit valence dependence into the atom-based analytic BOP formalism which is missing from simpler interatomic potentials such as the EAM or FS potentials. Using the rescaled onsite energy $\gamma_{0i\alpha}$ given by

$$\gamma_{0i\alpha} = \left(E_{i\alpha} - a_{i\alpha}^{(\infty)}\right)/b_{i\alpha}^{(\infty)}, \tag{5.70}$$

the bond energy may be written as

$$\begin{aligned} U_{bond} &= 2\int^{E_F}(E - E_{i\alpha})n_{i\alpha}(E)dE \\ &= 2\sum_{i\alpha} b_{i\alpha}^{(\infty)} \sum_{n=0}^{n_{max}} \sigma_{i\alpha}^{(n)}\left[\hat{\chi}_{(n+2)} - \gamma_{0i\alpha}\hat{\chi}_{(n+1)} + \hat{\chi}_{(n)}\right], \end{aligned} \tag{5.71}$$

and the number of the electrons as

$$N_{i\alpha} = 2\int^{E_F} n_{i\alpha}(E)dE = 2\sum_{n=0}^{n_{max}} \sigma_{i\alpha}^{(n)}\hat{\chi}_{(n+1)}. \tag{5.72}$$

5.4.5 Extensions of Analytic BOP

Inclusion of magnetism

Pettifor and Drautz extended the analytic BOP formalism to include collinear and non-collinear magnetism and charge transfer[34]. Just as for the inclusion of magnetism within the TB model (see equation 5.41) the local coordinate system for each atom i and orbital α must first be rotated such that the z axis is parallel to the local moment. Once this is done the system can be characterised by just the up- and down-spin DOS which can be evaluated from the $\uparrow\uparrow$ and $\downarrow\downarrow$ matrix elements of the moments of the global Hamiltonian, namely

$$\mu_{i\alpha\nu}^{(n)} = \int E^{(n)} n(E)_{i\alpha\nu} dE = \langle i\alpha\nu | \hat{H}^n | i\alpha\nu \rangle. \tag{5.73}$$

The expressions considered in Section 5.4.4 remain fundamentally the same but now include the spin index ν which denotes either $\uparrow$ or $\downarrow$ spins. For example the bond energy becomes

$$U_{bond} = \sum_{i\alpha} \sum_{\nu=\uparrow,\downarrow} b_{i\alpha\nu}^{(\infty)} \sum_{n=0}^{n_{max}} \sigma_{i\alpha\nu}^{(n)} \Big[\hat{\chi}_{(n+2)} - \gamma_{0i\alpha\nu} \hat{\chi}_{(n+1)} + \hat{\chi}_{(n)} \Big], \tag{5.74}$$

with $\gamma_{0i\alpha\nu} = \left(E_{i\alpha\nu} - a_{i\alpha\nu}^{(\infty)} \right) / b_{i\alpha\nu}^{(\infty)}$, the magnetic expansion coefficients

$$\sigma_{i\alpha\nu}^{(n)} = \sum_{m=0}^{n} p_{nm} \hat{\mu}_{i\alpha\nu}^{(m)}, \tag{5.75}$$

and the local magnetic Fermi phase, upon which the response functions $\hat{\chi}$ depend,

$$\phi_{F,i\alpha\nu} = cos^{-1} \left[\left(E_F - a_{i\alpha\nu}^{(\infty)} \right) / b_{i\alpha\nu}^{(\infty)} \right]. \tag{5.76}$$

The normalised moments of the local density of states are given by

$$\hat{\mu}_{i\alpha\nu}^{(m)} = \frac{1}{\left(2b_{i\alpha\nu}^{(\infty)}\right)^m} \sum_{n=0}^{m} \binom{m}{n} (-1)^n a_{i\alpha\nu}^{(\infty)n} \mu_{i\alpha\nu}^{(m-n)}. \tag{5.77}$$

The exchange energy is the same as that used in TB (Eq. 5.36) and the local magnetic moment is given by

$$\begin{aligned} m_i &= N_{i\uparrow} - N_{i\downarrow} \\ &= \sum_{\alpha} \left(\sum_{n=0}^{n_{max}} \sigma_{i\alpha\uparrow}^{(n)} \hat{\chi}_{(n+1)} \left(\phi_{F,i\alpha\uparrow}\right) \right. \\ &\qquad \left. - \sum_{n=0}^{n_{max}} \sigma_{i\alpha\downarrow}^{(n)} \hat{\chi}_{(n+1)} \left(\phi_{F,i\alpha\downarrow}\right) \right). \end{aligned} \tag{5.78}$$

Gradients and forces in analytic BOP

Within the TB approximation any set of self-consistent charges or moments correspond to a stationary point in the energy i.e. they minimise the binding energy. This however breaks down for low-moment BOP expansions where the approximate DOS leads to an inequivalence between the self-consistent solution and that which minimises the energy. Therefore within a BOP calculation, to ensure that the energies and forces are consistent, the true stationary point of the binding energy must be found by a direct minimisation with respect to the charge and magnetic moments, or equivalently, the Hamiltonian onsite levels[34]. This is done by ensuring that the gradients of the binding energy with respect to the Hamiltonian onsite levels are zero, that is

$$\sum_{i\alpha\nu} \frac{\partial U_B}{\partial E_{i\alpha\nu}} = 0. \tag{5.79}$$

The derivatives of the binding energy can be rewritten in terms of the local moments, and the gradients of the local moments with respect to the onsite levels can then be found[226,34]. These various analytic derivatives were recently explicitly

derived by Ford *et al.*[226,225].

A key advantage of analytic BOP is that the calculation of the derivatives also allows a Hellmann-Feynman type expression for the exact analytic forces to be evaluated at no extra computational cost. The expression for these forces, valid once the condition of Eq. 5.79 has been fulfilled, is given by

$$F_k = -\nabla_k U_B = \sum_{i\beta\nu}^{i\alpha \neq j\beta} \tilde{\Theta}_{i\alpha\nu j\beta\nu} \nabla_k H_{j\beta\nu i\alpha\nu} + \nabla_k U_{rep} \tag{5.80}$$

where ∇_k is the gradient due to displacing an atom k in real space and the 'bond-order' term $\tilde{\Theta}_{i\alpha\nu j\beta\nu}$ becomes the usual bond-order (cf. Eq. 5.20) as $n_{max} \to \infty$[34].

Maintaining LCN

Because the self-consistent solution in an analytic BOP calculation does not correspond to a stationary point in the energy, local charge neutrality must be enforced in a slightly different way than in a TB calculation. It is achieved by including an onsite-only Coulomb term U_C, equivalent to a Hubbard U term, in the binding energy. U_C is given by

$$U_C = \frac{1}{2} \sum_i J_i q_i^2 \tag{5.81}$$

where the value of J_i is chosen to be large enough to discourage the accumulation of charge on any atom i.e. to ensure that the LCN condition is fulfilled. In practice a value of 8 eV was used in all calculations. The local charge q_i is defined as the difference between the number of electrons N_i on site i and the number of electrons on the uncharged reference atom $N_i^{(0)}$ and is given by

$$\begin{aligned} q_i &= N_i - N_i^{(0)} \\ &= \sum_\alpha \sum_\nu \sum_{n=0}^{n_{exp}} \left(\sigma_{i\alpha\nu}^{(n)} \hat{\chi}_{(n+1)} \left(\phi_{F,i\alpha\nu} \right) - N_{i\alpha\nu}^{(0)} \right). \end{aligned} \tag{5.82}$$

For local charge neutrality $q_i = 0$ is required for each atom.

Explicitly positive density of states

In the original analytic BOP paper[33] it was shown that some BOP DOS contained small negative regions at the band edges. More recently it was shown that, even for elements for which the Fermi level lies towards the middle of the band, regions of negative DOS can significantly affect the outcome of defect structure calculations and that in calculations with non-collinear magnetism regions of negative DOS can occur in the middle of the band[225]. An example of this may be seen in the left hand panel of Fig. 5.2 where the DOS of AFM α-Mn, as calculated within the original BOP formalism using 12 moments is shown. The TB DOS is given in the right hand panel for comparison. This motivated the development of an adaptation to analytic BOP theory[224] in which applying kernel damping factors to the expansion coefficients $\sigma_{i\alpha\nu}^{(n)}$ can ensure an analytic BOP DOS which is positive across the whole band. The central panel of Fig. 5.2 shows the AFM α-Mn DOS as calculated using the improved BOP formalism, 'BOP+'. In contrast to the DOS in the left hand panel the 'BOP+' DOS is clearly positive everywhere.

These adaptations involve first rewriting the expansion of the DOS given in Eq. 5.59 in the form of an integral equation

$$n_{i\alpha\nu}^{(n_{max})}(\epsilon) = \int K^{(n_{max})}(\epsilon, \epsilon') n_{i\alpha\nu}(\epsilon') d\epsilon' \tag{5.83}$$

where $n_{i\alpha\nu}(\epsilon)$ is the true DOS and $K(\epsilon, \epsilon')$ a kernel which ensures that the expansion of $n_{i\alpha\nu}^{(n_{max})}(\epsilon)$ is smooth.

In the kernel polynomial method[233,234,236] the kernel is expanded in terms of Chebyshev polynomials of the first kind but Seiser *et al.*[224] showed that the kernel

may be expanded in Chebyshev polynomials of the second kind as

$$K^{(n_{max})}(\epsilon,\epsilon') = \frac{1}{\pi}\frac{2}{\sqrt{1-\epsilon^2}}\left[\sum_{n=0}^{n_{max}} g_U^{(n)} U_n(\epsilon) U_n(\epsilon')\right], \tag{5.84}$$

where $g_U^{(n)}$ are kernel expansion coefficients, i.e. damping factors, appropriate to Chebyshev polynomials of the second kind. The local DOS may then be written as

$$n_{i\alpha\nu}^{(n_{max})}(\epsilon) = \frac{2}{\pi}\sqrt{1-\epsilon^2}\left[\sum_{n=0}^{n_{max}} g_U^{(n)} \sigma_{i\alpha\nu}^{(n)} U_n(\epsilon)\right]. \tag{5.85}$$

In making use of the kernel the choice of the recursion coefficients, $a_{i\alpha\nu}^{(\infty)}$ and $b_{i\alpha\nu}^{(\infty)}$, is critical to obtaining a sensible expansion of the DOS. For example if they are chosen such that the bandwidth is too narrow then this may result in a negative DOS despite the kernel being positive. The form of the recursion coefficients given in equations 5.64 and 5.65 are suitable for use with the kernel expansion outlined above.

While the inclusion of the kernel expansion coefficients can ensure that the DOS is positive everywhere it also leads to a loss of detail in the DOS because the higher

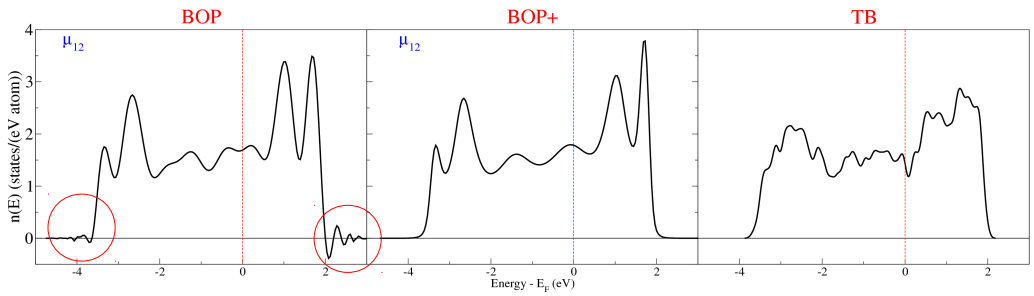

Figure 5.2: DOS for AFM α-Mn calculated using (left panel) original BOP formalism, (centre panel) BOP formalism with explicitly positive DOS and (right panel) TB. Negative, oscillating regions of DOS can be clearly seen in the DOS of the original BOP formalism, while the DOS in the centre panel is clearly positive everywhere. These DOS were calculated using the Mn model which will be discussed in Chapter 7.

moments in the expansion are strongly damped. Therefore additional moments must be included in the expansion but this must be done without causing a significant increase in calculation time. The approach used is to rewrite the local DOS expansion in terms of moments that are calculated exactly from 0 up to n_{max} plus additional moments, which run from $n_{max}+1$ up to n_{exp}, that are calculated approximately using the recursion method as per Eq. 5.47[224]. The local DOS is therefore written as

$$n_{i\alpha\nu}(\epsilon) = \frac{2}{\pi}\sqrt{1-\epsilon^2}\Bigg[\sum_{n=0}^{n_{max}} g_U^{(n)}\sigma_{i\alpha\nu}^{(n)}U_n(\epsilon) + \sum_{n_{max}+1}^{n_{exp}} g_U^{(n)}\sigma_{i\alpha\nu}^{(n)}U_n(\epsilon)\Bigg]. \tag{5.86}$$

The expansion coefficients in the first term in the square brackets, which runs up to n_{max} moments, are calculated exactly using the analytic BOP formalism. In contrast the expansion coefficients in the second term, corresponding to the remaining 'fictitious' moments, which run from $n_{max}+1$ up to n_{exp}, are obtained from the approximate square-root terminator. The time taken to calculate the fictitious moments is negligible but the number of extra moments must be chosen such that the energy is converged. Using this method the analytic BOP expansion converges smoothly to the recursion/numerical BOP expansion but is still fully analytic such that the exact forces may be evaluated.

5.4.6 Computational Details

BOP calculations were also performed using the BOPfox code[218] using the bond integrals and repulsive and embedding parameters from the TB model, details of which are given in Chapters 7 and 8. Local charge neutrality (LCN) was enforced by using a J_i of 8 eV. A feature of using the damping coefficients to maintain a strictly

positive DOS is that the higher moment contributions to the expansion are damped and the number of additional moments n_{exp} therefore needs to be chosen to ensure a good reproduction of the DOS. Test calculations show that using a terminator with 100 additional moments produces consistent results, even for large values of exact moments. All analytic BOP calculations have therefore been performed using $n_{exp} = 100$. With the version of the BOPfox code used in this work the speed of a TB calculation τ_{TB}, for a four atom unit cell, is comparable to that of a 17-moment BOP calculation. In contrast a 14-moment BOP calculation takes $\sim$0.40 τ_{TB} and a 9-moment BOP calculation takes $\sim$0.05 τ_{TB}. The convergence of BOP results to those of TB, as a function of the number of moments, will be discussed in the following chapters.

5.5 Summary

Density functional theory is a quantum mechanical modelling method which can be used to compute the ground state electronic properties of many-body condensed matter systems by solving carefully approximated solutions to the non-relativistic time-independent Schrödinger equation. Within DFT the charge density replaces the wavefunction as the central quantity and using the two Hohenberg-Kohn theorems and the Kohn-Sham equations the problem of finding the ground state of a system of N interacting electrons can be recast to self-consistently solving a set of Schrödinger equations for N non-interacting electrons which move in an effective potential.

In the tight-binding approximation the electronic wavefunction is expanded approximately using a superposition of wavefunctions for isolated atoms located at each atomic site. A number of assumptions are made which results in a simplified form of the Hamiltonian which is much easier to diagonalise. TB is therefore signif-

icantly less computationally demanding than DFT. The tight-binding bond model, which can be derived as a second-order expansion of the Kohn-Sham total energy in DFT with respect to charge and magnetic fluctuations, offers an intuitive physical description of chemical bonding in molecules and cohesion in solids, and it can be extended to include the effects of magnetism using the Stoner model. It also provides a first step in coarse-graining *ab initio* DFT to simpler interatomic potentials such as bond-order potentials.

Bond-order potentials are a class of real-space order (N) interatomic potentials in which the electronic structure is related to the local topology of a crystal using the moments theorem. BOPs can be considered as a systematic extension of the Finnis-Sinclair potential to include higher moments which sample the crystal structure, and therefore bonding, further out into a material. Analytic BOP theory is derived from a moments-based perturbation expansion of the continued fraction approximation in terms of Chebyshev polynomials of the second kind. The bond energy may be integrated analytically and the forces calculated exactly. An overview of analytic BOP theory has been given and details of the inclusion of magnetism and the recent development of the guarantee of a strictly positive density of states have been described.

Chapter 6

Origin of the Ground State Structural Trend from χ to hcp down Group VII

6.1 Introduction

It has been noted that Mn is anomalous in having a complex χ-phase ground state rather than hcp as is found for the other group VII elements, 4d Tc and 5d Re. It has been commonly reported that the reason for the stability of the χ-phase in Mn is its self-intermetallic character driven by the atomic size difference of the two sets of inequivalent sites with the site I and II atoms, and their larger local coordination polyhedra, behaving as larger atoms which are therefore able to support larger magnetic moments, and the site III and IV atoms, and their smaller local coordination polyhedra, behaving as smaller atoms. However as is shown in Fig. 6.1 DFT calculations predict that, even without the magnetic energy which stabilises χ-phase AFM α-Mn, χ-phase NM α-Mn remains more stable than the hcp and fcc structures. This is in contrast to Tc and Re where the nonmagnetic χ-phase is less stable than nonmagnetic hcp. Thus magnetism and the resulting effective atomic size difference present in the χ-phase are not the critical factors in stabilising α-Mn.

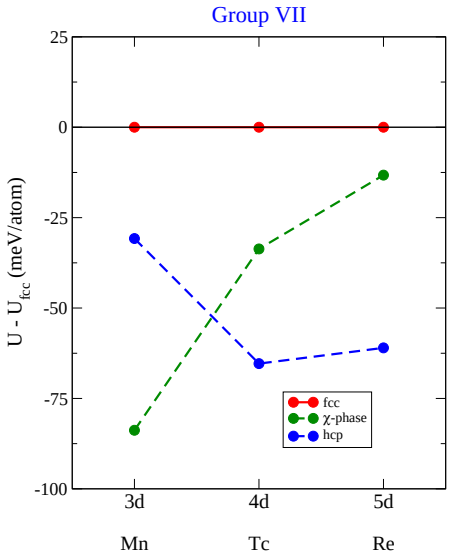

Figure 6.1: DFT structural energy differences for the nonmagnetic phases of the group VII elements Mn, Tc and Re. The total energies are all given relative to that of fcc for a given element. As expected from the trends across the periodic table Tc and Re are predicted to have hcp ground state structures but $3d$ Mn is predicted to anomalously adopt the χ-phase even in the absence of magnetism. The starting internal coordinates of the χ-phase, which are taken from a χ-phase niobium rhenium alloy[237] and which are used as the starting internal coordinates for the χ-phase throughout this work, have been fully relaxed.

6.2 Electronic Structure and Internal Coordinates

In order to highlight any differences between Mn, Tc and Re, and therefore the reason for the anomalous stability of the χ-phase in Mn, the electronic structure of the fcc, hcp and χ phases for these three elements was investigated using DFT calculations. Furthermore differences between the relaxed χ-phase geometries were also analysed.

6.2.1 Electronic Structure

A comparison of the DFT total DOS for the NM χ-phase, hcp and fcc structures for Mn, Tc and Re is plotted in Fig. 6.2. In each case the relative contributions of

s, p and d orbitals are given and as expected there are very few s and p states in the d-band. For all three structure types the bandwidth increases moving down the group from Mn $\rightarrow$ Tc $\rightarrow$ Re which reflects the increasing extent of the d orbitals on moving from $3d \rightarrow 4d \rightarrow 5d$ due to increasing core size. The DOS for the hcp and fcc structures of the three elements are fairly similar but it can be seen that for the χ-phase the d orbital DOS at E_F does exhibit a small difference, lying at the shoulder of a peak in Mn but lying in a small trough in Tc and Re. By examining

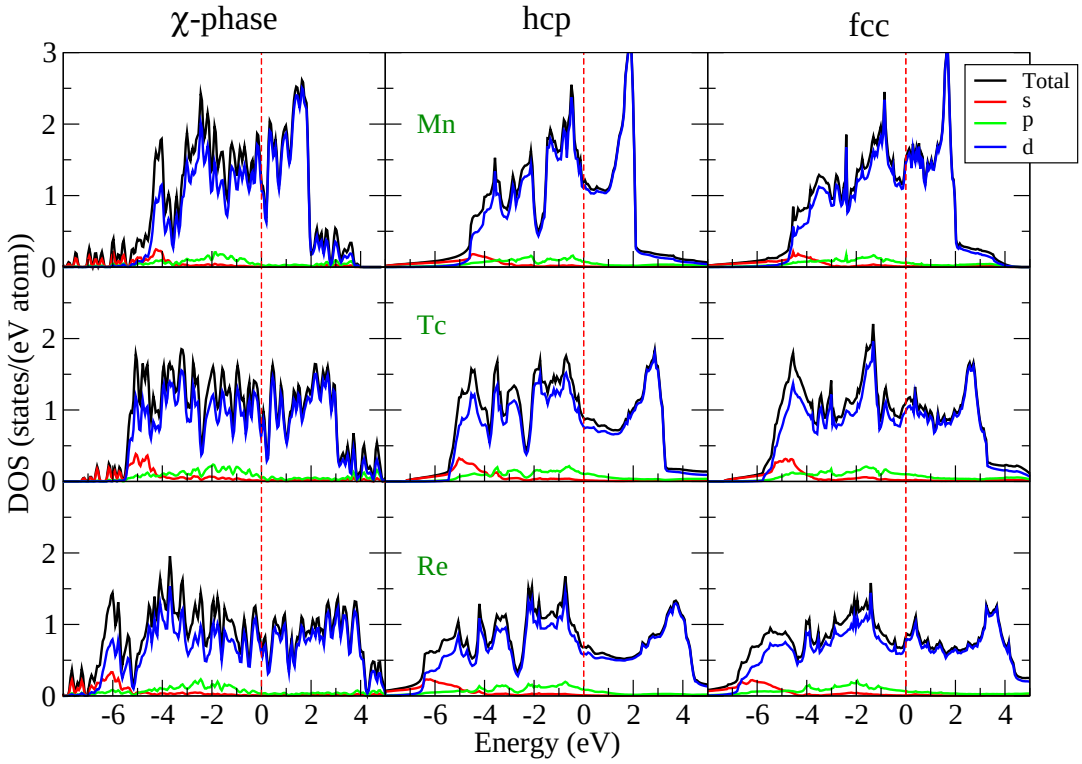

Figure 6.2: (Comparison of DFT total DOS for NM χ-phase, hcp and fcc for Mn, Tc and Re including the partial contributions from s, p and d orbitals. The Fermi level is marked with a dashed vertical line. There are no significant differences between the DOS of the Mn χ-phase and hcp structures and those of Tc and Re which could explain the anomalous stability of the χ-phase in Mn.

the local DOS of the four individual sites in the χ-phase, as shown in Fig. 6.3, it can be seen that the sources of this difference are shallow troughs in the local DOS at E_F of the site II, III, and IV atoms in Tc and Re which are absent in Mn. But is this

small difference the key to driving the stability of the χ-phase in Mn?

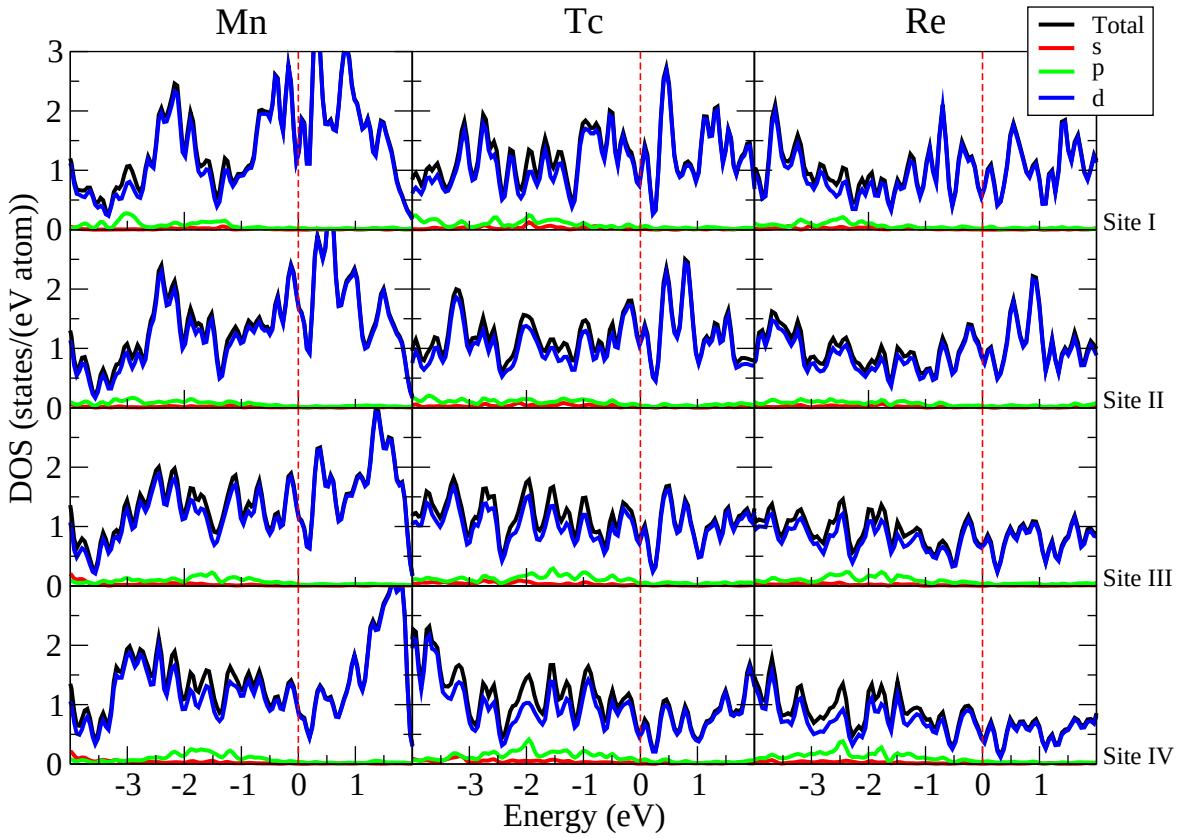

Figure 6.3: Comparison of DFT local DOS at the four inequivalent sites of the NM χ-phase for Mn, Tc and Re. The partial contributions from s, p and d orbitals are given. The Fermi level is marked with a dashed vertical line. Shallow troughs may be observed in the local DOS at E_F of the site II, III, and IV atoms in Tc and Re which are absent in Mn.

To analyse the possible effects of this small shoulder in the Mn DOS in Fig. 6.4 the total normalised DOS has been plotted as a function of band filling. In order to negate differences in the bandwidths of the three elements each has been normalised with respect to the DOS at E_F of the χ-phase at a band filling of $N = 7$ (corresponding to the seven valence electrons of the group VII elements). From these three plots it can be seen that the differences between the χ-phase DOS of Mn, Tc and Re are small and that there are no features in the electronic structure obviously responsible for driving the change in hcp-χ stability observed from the $3d$

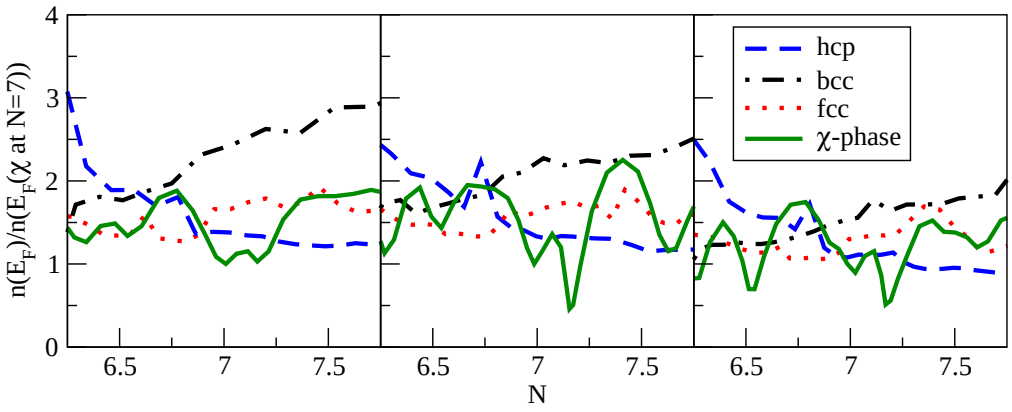

Figure 6.4: DFT total DOS as a function of band filling N for the χ-phase, fcc, bcc and hcp structures for Mn, Tc and Re. For each element the DOS has been normalised with respect to the value of the DOS at the Fermi level for the χ-phase at $N = 7$ (the valence electron count for the group VII elements). The value of the absolute DOS per atom of the χ-phase at $N = 7$ is 0.989 states/eV for Mn, 0.722 states/eV for Tc and 0.718 states/eV for Re.

to the 4d and 5d elements.

The DFT valence band structures have been plotted for Mn, Tc and Re in Fig. 6.5 within the primitive fcc unit cell. In order to compare them directly they have been normalised by the bandwidth of the respective element. It can be seen that the differences between the band positions and curvatures of all three elements are minor and it is notable that the separation between the top of the s band and the bottom of the d band at the Γ-point in Mn is similar to that in Tc and Re. This indicates that the degree of s-d hybridisation in Mn is not drastically different to that present in Tc and Re.

The charges on each atom and orbital in the χ-phase were also calculated. To do this within VASP a value of the Wigner Seitz radius is set such that the sum of the volume of the spheres around all the atoms is the same as the total volume of the cell. (Note that this means that the four inequivalent sites share the same Wigner Seitz radius rather than having unique values as should strictly be the case.) The total charges were then calculated by projecting the orbitals onto spherical

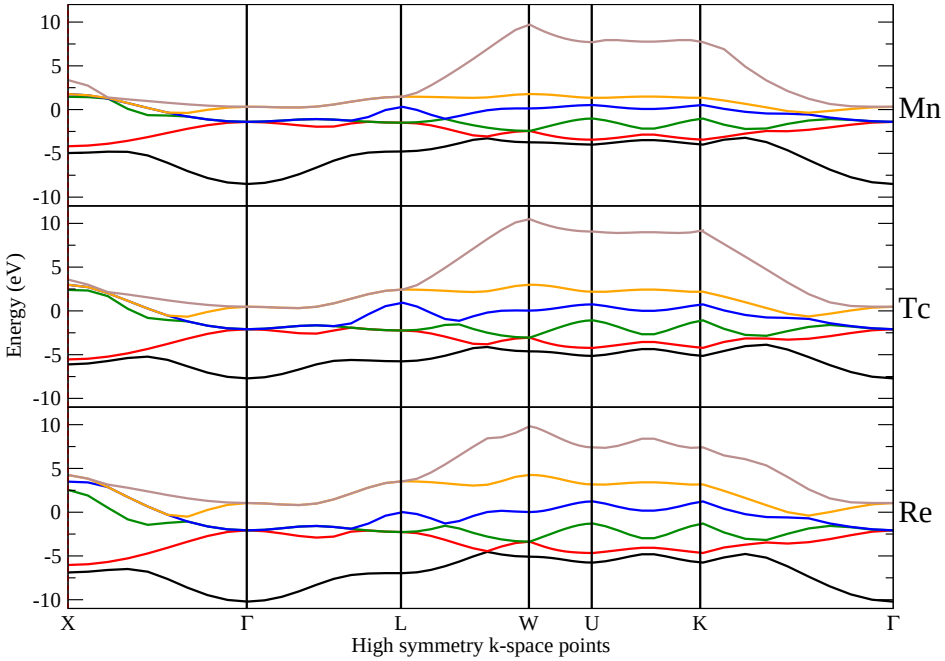

Figure 6.5: Band structure, normalised by the bandwidth, of the fcc primitive cell for Mn, Tc and Re, plotted at their respective equilibrium volumes.

Site	Charges per atom per site					
	d			$s+p+d$		
	Mn	Tc	Re	Mn	Tc	Re
I	5.24	5.05	4.71	6.20	5.99	5.82
II	5.27	5.10	4.75	6.26	6.07	5.94
III	5.34	5.19	4.86	6.45	6.28	6.19
IV	5.42	5.29	4.96	6.61	6.49	6.42

Site	Charges per site type as a % of total					
	d			$s+p+d$		
	Mn	Tc	Re	Mn	Tc	Re
I	2.8	2.8	2.6	3.3	3.3	3.2
II	11.2	11.1	10.5	13.3	13.2	13.1
III	34.1	33.9	32.2	41.2	41.1	41.1
IV	34.6	34.6	32.9	42.2	42.4	42.6

Table 6.1: Charges per site type for the nonmagnetic χ-phases of Mn, Tc and Re. The upper table contains the absolute charge per atom per site both for the d orbital projections alone and for the sum of the s, p and d orbital projections. The lower table contains the total charges per site type (i.e. for 2 site I atoms, 8 site II atoms, 24 site III atoms and 24 site IV atoms) given as a percentage of the total charge of the 58-atom unit cell, also both for the d and the $s+p+d$ orbital projections.

harmonics that are non-zero within spheres of a radius equal to the Wigner Seitz radius. Analysis of the total charges per orbital and per site type in the χ-phase, an overview of which is given in Tab. 6.1, showed trends consistent only with a decrease in effective nuclear charge moving down the group from 3d to 4d to 5d. For example, while the absolute charges per atom per site for both the d and the $s + p + d$ orbital projections change a little from Mn $\rightarrow$ Tc $\rightarrow$ Re, as a percentage of the total charge they are very similar, especially for Mn and Tc. This seems to discount the possibility of variations in sp-d hybridisation or the relative numbers of valence d electrons being the critical factor in stabilising the χ-phase in Mn. (The calculations were also repeated with the Wigner Seitz radius adjusted such that the total charge, as calculated from summing the charges of the projected orbitals, was equal to 406, i.e. the total number of electrons in the 58-atom unit cell. Similar trends resulted.)

6.2.2 Internal Coordinates

The DFT relaxed internal coordinates of NM χ-phase Mn, Tc and Re are given in Table 6.2. It can be seen that the differences between the three sets of coordinates are very minor. To test whether these minor differences do play a critical role in de-

Structure	Magnetic state	Site	Internal coordinates								
			Mn			Tc			Re		
			x	y	z	x	y	z	x	y	z
χ	NM	I	0.500	0.500	0.500	0.500	0.500	0.500	0.500	0.500	0.500
		II	0.318	0.318	0.318	0.321	0.321	0.321	0.322	0.322	0.322
		III	0.357	0.357	0.038	0.357	0.357	0.041	0.358	0.358	0.043
		IV	0.088	0.088	0.281	0.090	0.090	0.282	0.090	0.090	0.283

Table 6.2: Relaxed internal coordinates for nonmagnetic the χ-phase of Mn, Tc and Re. The labelling convention used here can be matched to that used in Ref. 6.

termining the χ-hcp relative stabilities the DFT structural energy differences for the NM bcc, hcp, fcc and χ-phase structures of the 3d and 5d elements have been plotted using the relaxed χ-phase internal coordinates from both the 3d and 5d elements

in each group. These have been plotted in Fig. 6.6 for the $3d$ transition elements V to Co, and the corresponding $5d$ elements, Ta to Ir. It can be seen that even when using the relaxed internal coordinates from the $5d$ series the qualitative behaviour of the structural energy differences of the $3d$ series remain unchanged with χ more stable than hcp for group VII Mn. The same is true of the $5d$ series when using the $3d$ coordinates, except that for group VII Re hcp remains more stable than χ. Using the $4d$ series elements produces results in qualitative agreement to those described for the $5d$ series elements. These results suggest that the differing behaviour of Mn and Tc/Re is not driven by a structural effect. In summary therefore it has been found that differences in the electronic structure and relaxed internal coordinates of the χ-phase are not significant enough to explain the anomalous χ-phase stability in Mn.

6.3 Effective Atomic Repulsion

The canonical TB d-band model of Seiser *et al.*[228], previously used to investigate trends within topologically close-packed structures in the $4d$ and $5d$ series, was then used to further investigate how the effective atomic repulsion affects the relative stabilities of hcp and the χ-phase in the group VII elements. Within the canonical TB model the binding energy is given as the sum of a bond energy, as given in Eq. 5.25, and a repulsive energy. The bond integrals take the simple canonical form[207,238]

$$\left.\begin{matrix} dd\sigma \\ dd\pi \\ dd\delta \end{matrix}\right\} = \left.\begin{matrix} -6 \\ 4 \\ -1 \end{matrix}\right\} \beta(R) \tag{6.1}$$

where

$$\beta(R) = CR^{-n}, \tag{6.2}$$

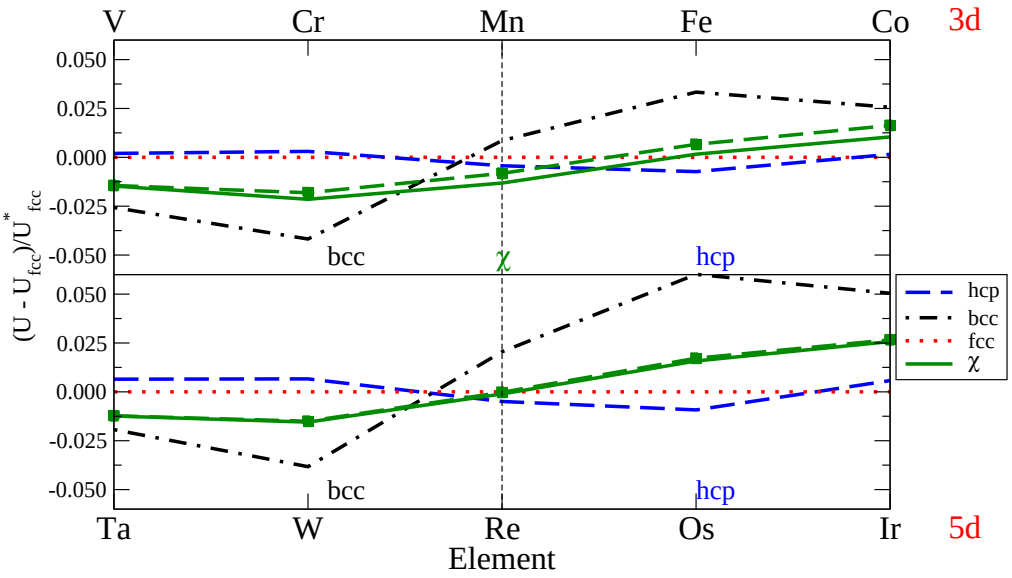

Figure 6.6: (Upper panel) DFT structural energy differences for the $3d$ transition metals, V to Co, calculated using fully relaxed χ-phase internal coordinates. The dashed, green χ-phase line marked with squares shows the structural energy differences calculated using the relaxed χ-phase internal coordinates for the corresponding $5d$ elements, Ta to Ir. (Lower panel) DFT structural energy differences for the $5d$ transition metals, Ta to Ir, calculated using fully relaxed χ-phase internal coordinates. The dashed, green χ-phase line marked with squares shows the structural energy differences calculated using the relaxed χ-phase internal coordinates for the corresponding $3d$ elements, V to Co. In both cases using the relaxed internal coordinates from the elements in another series leaves the χ-hcp stability unchanged. The energies are normalised with respect to U^*_{fcc} which is the group VII fcc total energy.

and C is a constant. The repulsive energy is assumed to be pairwise and given by the Wolfsberg-Helmholz approximation[5] decaying with distance as a power of the bond integral, namely

$$U_{rep} = \sum_{i,j,i\neq j} \Phi(R_{ij}), \tag{6.3}$$

where

$$\Phi(R_{ij}) = k[\beta(R_{ij})]^m. \tag{6.4}$$

The repulsive function is therefore dependent on both exponents n and m with

$$U_{rep} \propto R^{-nm}. \tag{6.5}$$

By varying the exponents n and m, which control the decay of the bond integrals and the repulsive energy, the role of the relative hardness of the potential on phase stability for a nearly half-filled d-band was investigated. Previous work has shown that changes in the relative hardness significantly affect structural stability. For sp-valent carbon the graphite ground state was shown to be stabilised over diamond by decreasing the relative hardness of the potential compared to silicon[239]. The origin of the decreased hardness for carbon as compared to silicon is due to the absence of p-core electrons in carbon, which leads to a weaker repulsion of the p-valence electrons from the core region[5]. The variation of the s-p level splitting then drives the stability from Si diamond to the close-packed fcc ground state of Pb down group IV, but cannot explain the grahite ground state of C[240]. Thus C (graphite), N (dimer) and O (dimer) all take more open ground state structures than their counterparts in the remaining rows of the groups because they have a decreased hardness, due to the absence of p electrons in their cores[5]. Related structural trends were also observed for four-atom molecules (linear chain, planar square, rhombus and tetrahedron) modelled by a simple pair potential. A harder potential was shown to stabilise the close-packed tetrahedron and rhombus over the more open square but when the hardness is decreased, the relative stabilities of the rhombus and the square switch[5]. Specifically, the change in relative stability of the rhombus and square occur as the degree of normalised hardness α_h, given by $(m-1)/m$, decreases from $\frac{1}{2}$ to $\frac{1}{3}$.

I

Fig. 6.7 shows a plot of the structural energy difference of hcp relative to χ as a function of both n and m as calculated using the canonical TB model with a valence electron count of N_d = 5.7. Increasing n relates to the bond integrals decaying more rapidly while decreasing m relates to the repulsive function decaying less rapidly. The χ-phase is stabilised over hcp as n is increased above $\sim$4.25 and as

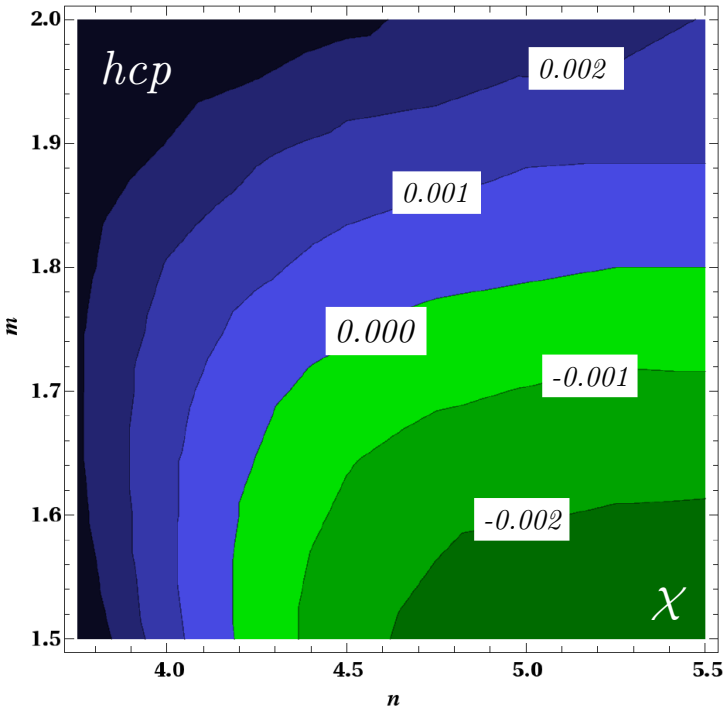

Figure 6.7: Plot of $U^{\chi}_{bond} - U^{hcp}_{bond}$ energies, calculated using the structural energy difference theorem (Eq. 7.6), as a function of the exponents n and m which control the decay of the bond integrals and the repulsive energy in the canonical TB model. The calculations used a constant of proportionality of 1 in Eq. 6.5 and, for comparison with Fig. 7.5, the bonding energies have been normalised with respect to U^{fcc}_{bond} using $m = 2$ and $n = 4$. All calculations are for $N_d = 5.7$. The domain of χ-phase stability, plotted in green and corresponding to negative values of $U^{\chi}_{bond} - U^{hcp}_{bond}$, lies in the lower right of the plot where m is small and n large. The domain of hcp stability is plotted in blue and corresponds to positive values of $U^{\chi}_{bond} - U^{hcp}_{bond}$.

m is decreased from 2.00 to 1.50, which corresponds to α_h decreasing from $\frac{1}{2}$ to $\frac{1}{3}$. That is, the χ-phase structure becomes more stable than the more close-packed hcp structure as the potential is softened. The source of the structural trend of the group VII elements therefore appears to be analogous to that of the group IV elements discussed above. Mn is expected to have a softer core because it lacks core d states and its valence electrons are therefore able to readily penetrate the core region. This favours the more open-packed χ-phase structure over the closer-packed hcp. In contrast $4d$ Tc and $5d$ Re have harder cores which stabilise the closer-packed hcp. Consistent with this argument it is found that the hcp-χ-phase

energy difference for 5d Re, which we would expect to have a harder core than 4d Tc, is larger, 48 meV/atom, than that of 4d Tc, 32 meV/atom. Additionally the existence of the binary χ-phase alloys in which Tc and Re are found in the presence of elements which lie to their left in the periodic table e.g. $Nb_{0.25}Tc_{0.75}$, $Zr_{0.14}Tc_{0.86}$, $Ta_{0.25}Re_{0.75}$ and $Hf_{0.14}Re_{0.86}$ also makes sense in the context of this argument because such alloying elements are larger and have softer cores than Tc and Re thus leading to the stabilisation of the χ-phase.

It is apparent that the repulsion in the canonical TB with $m = 2$ and $n = 4$ is hard enough to stabilise close-packed hcp over the χ-phase thus reproducing the relative structural stabilities characteristic of 4d Tc and 5d Re[228]. In contrast we will see in the following Chapter that in the newly parameterised Mn TB model the repulsion is soft enough to reproduce the χ-phase stability characteristic of 3d Mn.

6.4 Summary

DFT calculations have shown that without magnetism the χ-phase is still the ground state of Mn implying that magnetism and the resultant atomic size difference between large and small moment atoms are not the critical factors, as is commonly believed, in driving the anomalous stability of the χ-phase over hcp. DFT calculations of Mn, Tc and Re have shown that there are no differences in the electronic structure or internal coordinates which are large enough to explain why the χ-phase is stable for Mn but hcp is stable for Tc and Re.

Using a canonical tight-binding (TB) model it is found that for a more than half-filled d-band, while harder potentials stabilise close-packed hcp, a softer potential stabilises the more open χ-phase. By analogy with the structural trend from open to close-packed phases down the group IV elements, the anomalous stability of the χ-phase in Mn is shown to be due to 3d valent Mn lacking d states in the core which

leads to an effectively softer atomic repulsion between the atoms than in $4d$ Tc and $5d$ Re.

Chapter 7

Magnetic Analytic BOP for Mn

7.1 Introduction

In this chapter the details and results of new TB and BOP models for Mn will be given. The binding energies, elastic constants and vacancy formation energies of the five main structure types of Mn have been calculated using these models and compared to the results of reference DFT calculations. Furthermore the ground state magnetic configurations for each structure type have been compared as have the relaxed internal coordinates for the α- and β-Mn structures. Reproduction of the density of states and the structural energy difference plots discussed in Chapter 6 are also analysed. The convergence of the BOP binding energies and elastic constants, with respect to those of TB, as a function of increasing number of moments have also been assessed.

7.2 Model Parameters

The parameters for the Mn model, which are given in Table 7.1, were fitted as follows. Firstly the bond integrals which are given by simple exponential func-

Repulsive energy		
a_{rep} (eV)	b_{rep} (Å^{-1})	c_{rep}
896.80	3.362	0.907
a_{hcr} (eV)	b_{hcr} (Å^{-1})	c_{hcr}
10000	0.01	15
Embedding potential		
a_{emb} (eV^2)	b_{emb} (Å^{-1})	c_{emb}
2.513	0.0631	2.542
Bond integrals		
	a (eV)	b (Å^{-1})
$dd\sigma$	-24.723	1.404
$dd\pi$	81.218	2.101
$dd\delta$	-83.284	2.892
Stoner parameter		Electron count
I_d (eV)		N_d
0.65		5.7

Table 7.1: Mn TB model parameters: repulsive energy, embedding potential, bond integrals, Stoner parameter and electron count.

tions[102,103] of the form

$$\beta_{dd\lambda}(R) = a_{dd\lambda}\exp(-b_{dd\lambda}R), \qquad \lambda = \sigma, \pi, \delta, \tag{7.1}$$

were parameterised by collaborators at the Interdisciplinary Centre for Advanced Materials Simulation (ICAMS), Ruhr-Universität Bochum, Germany. These were fitted to the matrix elements of the Mn dimer which McEniry *et al.* obtained by projecting an extended multiple-ζ basis set, taken from DFT calculations based on the linear combination of atomic orbitals (LCAO) approach, onto an optimised single-ζ basis set which was then orthogonalised via the Löwdin transformation[100]. Alternative methods exist for extracting TB bond integrals from DFT[241]. Within the d-band model s and p electrons are not explicitly treated however some effect of the broad s-p band may be accounted for by varying the number of d electrons N_d. The value of N_d in the model was chosen to minimise the error between the TB and DFT bonding energies of the NM hcp ϵ-Mn and NM fcc γ-Mn structures at their equilibrium

volumes.

In addition to the usual attractive bond energy of Eq. 5.25 an attractive embedding term is also included to account for the contribution of the s electrons and sd hybridisation, which are not included in the TB Hamiltonian, to the cohesive energy. The Finnis-Sinclair[29] square-root embedding function is chosen with the embedding potential given by

$$U_{emb} = -\sum_i \sqrt{\sum_{j\neq i} (a^{ij}_{emb})^2 \exp(-b^{ij}_{emb}(R_{ij})^{c^{ij}_{emb}})}. \tag{7.2}$$

The repulsive energy which accounts for the overlap repulsion, double counting energy and ion-ion repulsion is represented by two stretched exponential terms

$$\begin{aligned} U_{rep} = \sum_i \sum_{j\neq i} \Big[& a^{ij}_{rep} \exp(-b^{ij}_{rep}(R_{ij})^{c^{ij}_{rep}}) \\ & + a^{ij}_{hcr} \exp(-b^{ij}_{hcr} R_{ij}) R_{ij}^{-c^{ij}_{hcr}} \Big]. \end{aligned} \tag{7.3}$$

The first term follows the form of the repulsive energy of a previous TB model[100] and the second, a hard-core repulsion which has a form similar to a Yukawa potential, has been introduced to ensure that the internal coordinates of α-Mn and vacancy-containing structures relax correctly.

The parameters for the hard-core part of the repulsive function were chosen to ensure a strong repulsion at atomic distances of less than 2 Å while the remaining repulsive and embedding parameters were then fitted to minimise errors in the TB binding energies with respect to the DFT energy-volume curves of the NM α-, β-, γ-, δ- and ϵ-Mn and the AFM α- γ- and δ-Mn structures for atomic volumes of between 8 and 14 Å^3. The range over which the bond integrals, repulsive energy

and embedding energy all extend is controlled by a cosine cut-off function

$$f(R) = \frac{1}{2}\left(\cos\left(\pi\left(\frac{R-(R_{cut}-d_{cut})}{d_{cut}}\right)\right)+1\right), \tag{7.4}$$

for

$$R_{cut} - d_{cut} \leq R < R_{cut}. \tag{7.5}$$

This ensures firstly that the parameters decay smoothly to zero in order to avoid any discontinuities and secondly controls how many shells of neighbours are taken into account within the model. It should be noted that the effect of cutting off the two-centre matrix elements beyond say the second nearest neighbour shell is likely to be small compared to the effect of neglecting all of the three-centre terms[96]. However while contributions from three-centre and non-orthogonal terms can be large in sp valent elements such as fcc Al and diamond Si they are small within the Fe d band[242] and it is therefore the neglect of $sp-d$ hybridisation that is expected to have the most significant effect on the accuracy of the bandstructure within the current model. Indeed it is necessary to include $sp-d$ hybridisation to reproduce the phonon spectra, and hence elastic constants, of bcc transition metals[243,244]. With the efficient implementation of large-scale BOP simulations in mind the model was parameterised with shorter-ranged cut-offs than those of previous Mn TB models[100] such that the Hamiltonian matrix elements are cut off by the fourth, and the U_{rep} and U_{emb} functions by the fifth, nearest neighbours in fcc γ-Mn. Specifically, the cut-offs are $R_{cut} = 4.5$ Å and $d_{cut} = 1.0$ Å for the bond integrals, and $R_{cut} = 5.5$ Å and $d_{cut} = 0.5$ Å for the repulsive and embedding functions.

The value of the Stoner parameter I_d was chosen to best reproduce the behaviour of the magnetic states of the most stable structures. Whilst in principle its value should depend on the atomic environment[245], in-keeping with the simplicity of the TB model it is kept constant across all structure types ignoring volume-

dependent effects, which are small[51].

7.3 Relative Structural Stabilities of the Nonmagnetic Phases of Mn

Results for the DFT, TB and BOP calculations are presented in the following sections. Fig. 7.1 shows a plot of the binding energy curves for the five primary phases of Mn calculated with DFT (left-hand panel), TB (centre-left), 20-moment BOP (centre-right) and 14-moment BOP (right). For α- and β-Mn the internal coordinates have been fully relaxed using DFT, TB and BOP, respectively. Looking at the left-hand panel of Fig. 7.1 and considering only the nonmagnetic structures, DFT predicts the relative ordering from $\alpha \rightarrow \beta \rightarrow \epsilon \rightarrow \gamma \rightarrow \delta$. The TB and BOP models reproduce this ordering with even the very small energy difference between the β and ϵ structures correctly characterised. The relative stabilities of the fcc and hcp structures is a key metric for determining the prevalence of the TRIP or TWIP plasticity mechanisms in Mn-containing steels and the NM γ-ϵ energy difference in TB, 20-moment and 14-moment BOP of 29, 34 and 38 meV, are close to the DFT value of 35 meV. The absolute TB and BOP binding energies are all within 0.5 % of the DFT binding energies while the equilibrium atomic volumes are all within 3 % of DFT. The DFT atomic volumes are all within 2 % of those of the DFT results given in Ref. 90 which were also calculated within VASP using the all-electron PAW method. The PW91 GGA exchange-correlation functional[246] used by Hafner *et al.* is generally understood to produce numerically similar bulk properties to the PBE functional[200] used in this work and therefore it seems that the small discrepancies between the two sets of DFT data are most likely caused by differences in the cut-off energy used for the plane wave expansion and k-point grid sizes. For example, Hafner *et al.* used a cut-off of 250 eV while 350 eV was used in this work, and they used

k-point grids of $2 \times 2 \times 2$ for α-Mn, and up to $8 \times 8 \times 8$ for structures with smaller unit cells, whereas grids of $3 \times 3 \times 3$ for α-Mn, and up to $16 \times 16 \times 16$ for structures with smaller unit cells, were used in this work.

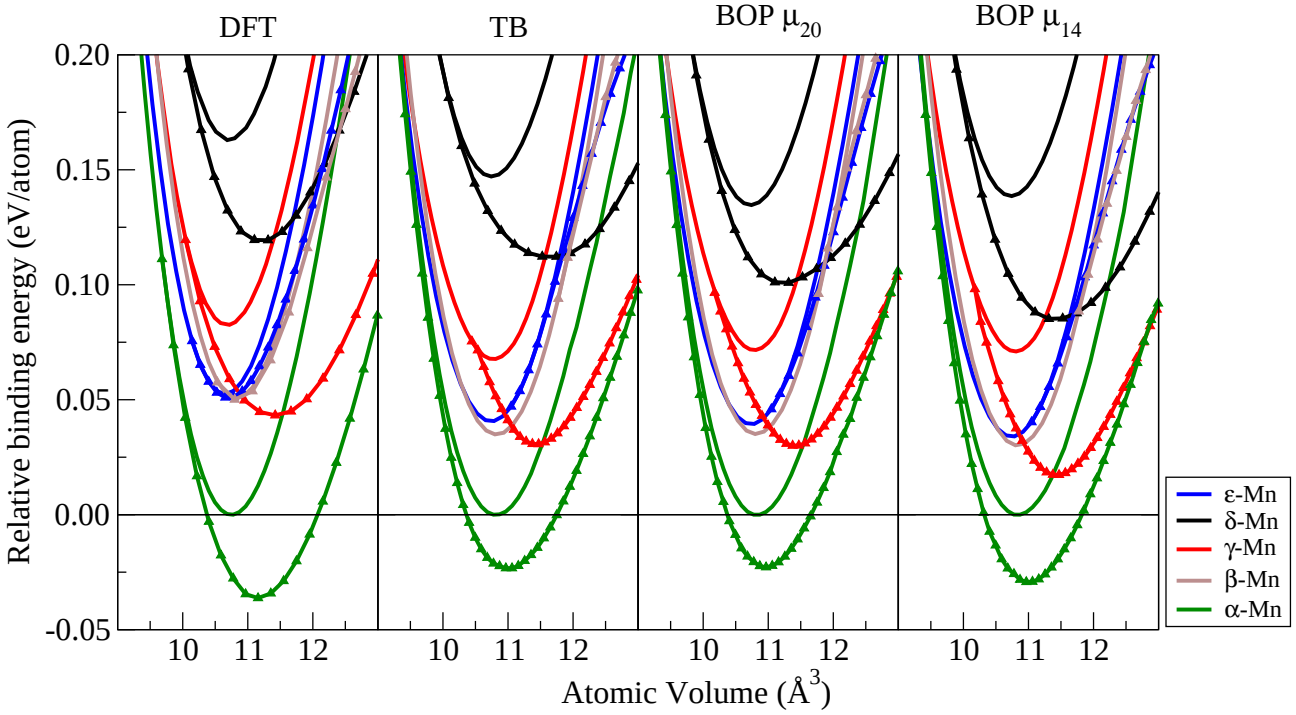

Figure 7.1: Plots of the binding energy relative to NM α-Mn for the α, β, γ, δ and ϵ phases of Mn. The curves for magnetic states, namely AFM α-Mn, FiM β-Mn, AFM γ-Mn and AFM2 δ-Mn, are marked with triangles. Results are shown for DFT (left), TB (centre-left), 20-moment BOP (centre-right) and 14-moment BOP (right).

Table 7.2 lists the internal coordinates, as relaxed using DFT, TB and BOP, for non-magnetic α- and β-Mn. The labelling conventions used here can be matched to those used in Refs. 6 and 90 for the α and β phase, respectively. It can be seen that in both cases the TB relaxed internal coordinates are similar to the DFT coordinates with slightly larger errors in the α-Mn site II coordinates and the β-Mn site I coordinate. The differences between BOP and TB are smaller than the differences between TB and DFT. Within the TB, 20-moment and 14-moment BOP calculations the c/a ratio of NM hcp ϵ-Mn is calculated to be 1.619, which is very

close to the value of 1.628 calculated within DFT and the ideal c/a ratio of 1.633.

Allotrope	Magnetic state	Site	Internal coordinates											
			DFT			TB			BOP μ_{20}			BOP μ_{14}		
			x	y	z	x	y	z	x	y	z	x	y	z
α	NM	I	0.500	0.500	0.500	0.500	0.500	0.500	0.500	0.500	0.500	0.500	0.500	0.500
		II	0.318	0.318	0.318	0.345	0.345	0.345	0.349	0.349	0.349	0.350	0.350	0.350
		III	0.357	0.357	0.038	0.349	0.349	0.030	0.349	0.349	0.033	0.347	0.347	0.035
		IV	0.088	0.088	0.281	0.089	0.089	0.296	0.089	0.089	0.298	0.089	0.089	0.299
	AFM	I	0.500	0.500	0.500	0.500	0.500	0.500	0.500	0.500	0.500	0.500	0.500	0.500
		II	0.319	0.319	0.319	0.322	0.322	0.322	0.327	0.327	0.327	0.327	0.327	0.327
		III	0.356	0.356	0.035	0.351	0.351	0.032	0.352	0.352	0.030	0.350	0.350	0.030
		IV	0.088	0.088	0.283	0.086	0.086	0.288	0.088	0.088	0.291	0.087	0.087	0.288
			x			x			x			x		
β	NM	I	0.052			0.041			0.038			0.038		
		II	0.197			0.196			0.194			0.193		
	FiM	I	0.054			0.041			0.038			0.038		
		II	0.198			0.196			0.194			0.193		

Table 7.2: Relaxed internal coordinates for non-magnetic and magnetic forms of α- and β-Mn. The labelling conventions used here can be matched to those used in Refs. 6 and 90 for the α and β phase, respectively. For NM hcp ϵ the optimised c/a ratio of NM hcp ϵ-Mn was calculated to be 1.619 using TB, 20-moment and 14-moment BOP. This is very close to the value of 1.628 calculated within DFT and the ideal c/a ratio of 1.633. However in this work the ideal c/a ratio was used for fcc γ- and hcp ϵ-Mn and the ideal rhombohedral angle was used for bcc δ-Mn.

In general it is clear that, as expected, the 20-moment BOP calculations reproduce the properties of the TB model better than those of the 14-moment BOP. It is instructive to compare the BOP DOS to see how much extra detail is included in the 20-moment DOS. The DOS calculated using DFT, TB, 20-moment BOP and 14-moment BOP for NM γ-, ϵ- and α-Mn are therefore shown in Fig. 7.2. It can be seen that the general shape of the TB DOS is reproduced by the 14-moment calculations but that some of the more subtle features are only reproduced in the 20-moment calculations. It is also clear that while the general shape of the DFT DOS can be said to be captured by the d-valent TB model, the finer structure such as the peaks and troughs close to the Fermi level are not reproduced due to the neglect of sd hybridisation. Thus we should anticipate that the TB, and BOP, models will have certain limitations.

The convergence of the analytic BOP NM binding energies to the TB binding energies are plotted in Fig. 7.3 for fcc γ-, hcp ϵ- and α-Mn. It can be seen that the BOP energies converge systematically as the number of moments is increased. It is

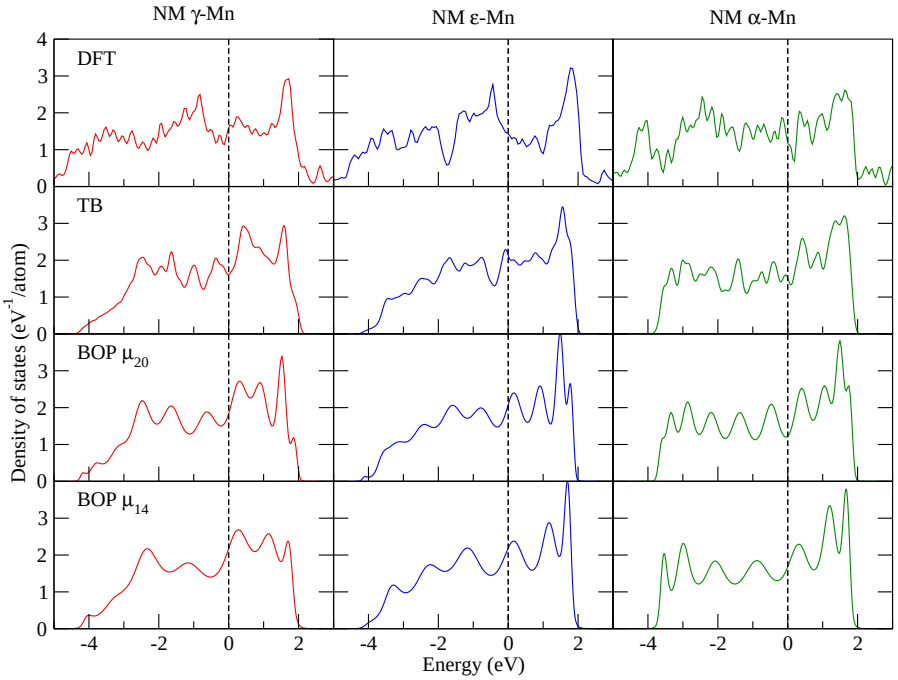

Figure 7.2: Comparison of the electronic density of states in nonmagnetic γ-Mn (left panel), ϵ-Mn (central panel) and α-Mn (right panel), as calculated using DFT (top), TB (upper centre), 20-moment BOP (lower centre) and 14-moment analytic BOP (bottom). The plots have been shifted such that the Fermi level lies at the zero of energy and is marked with a dashed vertical line. Methfessel-Paxton k-space integration with a smearing of 0.1 eV has been used in the TB and DFT calculations.

noted that the binding energy of AFM γ oscillates out of phase with the energies of the other structures. For example, the binding energy of NM γ-Mn falls close to a peak while that of AFM γ-Mn falls close to a trough for μ_{18}, but the reverse is true for μ_{16}. To investigate a possible cause of this the DOS for NM and AFM γ-Mn as calculated with TB and 14-, 16- and 18-moment BOP have been plotted in Fig. 7.4. It can be seen that while a peak is observed in the DOS at E_F for NM γ-Mn, a trough is observed for AFM γ-Mn for μ_{18}, and the reverse is true for μ_{16}. For μ_{14} the NM DOS does not lie exactly at a peak but it is close to one, while the AFM DOS lies in a trough. Thus it seems that differences between the shapes of the BOP DOS at the Fermi level correspond to the oscillations observed in the convergence of the BOP

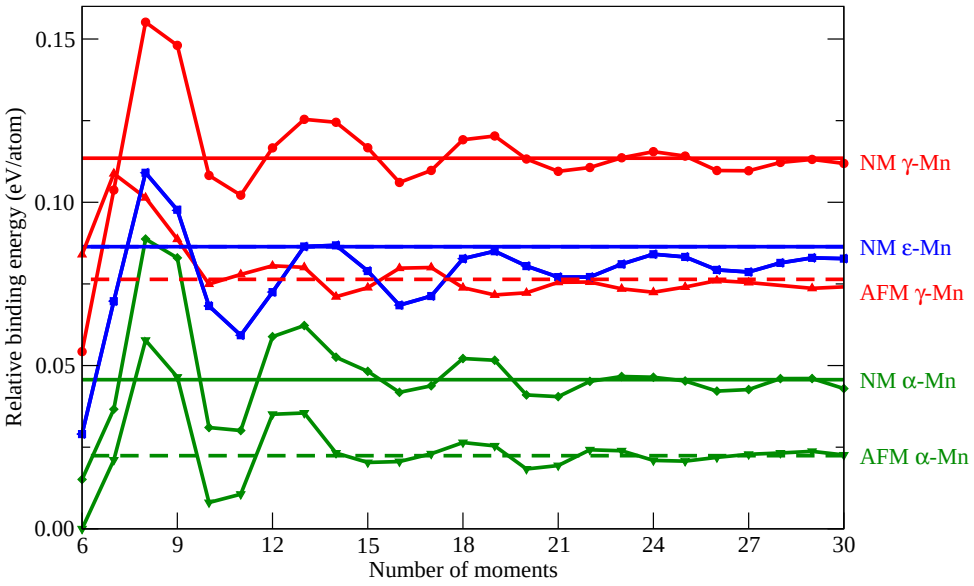

Figure 7.3: Convergence of BOP binding energies to TB binding energies as a function of increasing number of moments for NM and AFM (fcc) γ-Mn, NM (hcp) ϵ-Mn, and NM and AFM α-Mn.

binding energies as a function of the number of moments.

Structural Energy Differences

The structural energy difference theorem[247] allows differences in the structural energy to be approximated as the difference in the d-band energy alone, once the atomic volumes have been prepared such that all structures display the same average repulsive energy per atom. That is, to first order,

$$\Delta U = [\Delta U_{bond}]_{\Delta U_{rep}=0}. \tag{7.6}$$

In this section the attractive embedding term is grouped with the repulsive energy, resulting in a net repulsive contribution for use in Eq. 7.6. The TB NM structural

energy differences as a function of band filling for the bcc δ-Mn, hcp ϵ-Mn and α-Mn are plotted with respect to the bond energy of NM fcc γ-Mn in Fig. 7.5 with the results for the current Mn TB model in the upper right panel and those of the canonical TB model (with $m = 2$ and $n = 4$) in the lower right panel. In both cases the plots have been centred around $N_d = 5.7$ which is the d electron count in the Mn model. The DFT structural energy differences of the 3d transition elements from V to Co (upper right panel) and the corresponding 5d elements Ta to Ir (lower left panel) are also plotted. It can be seen that the Mn TB model qualitatively reproduces the behaviour observed for the 3d transition series, with χ most stable

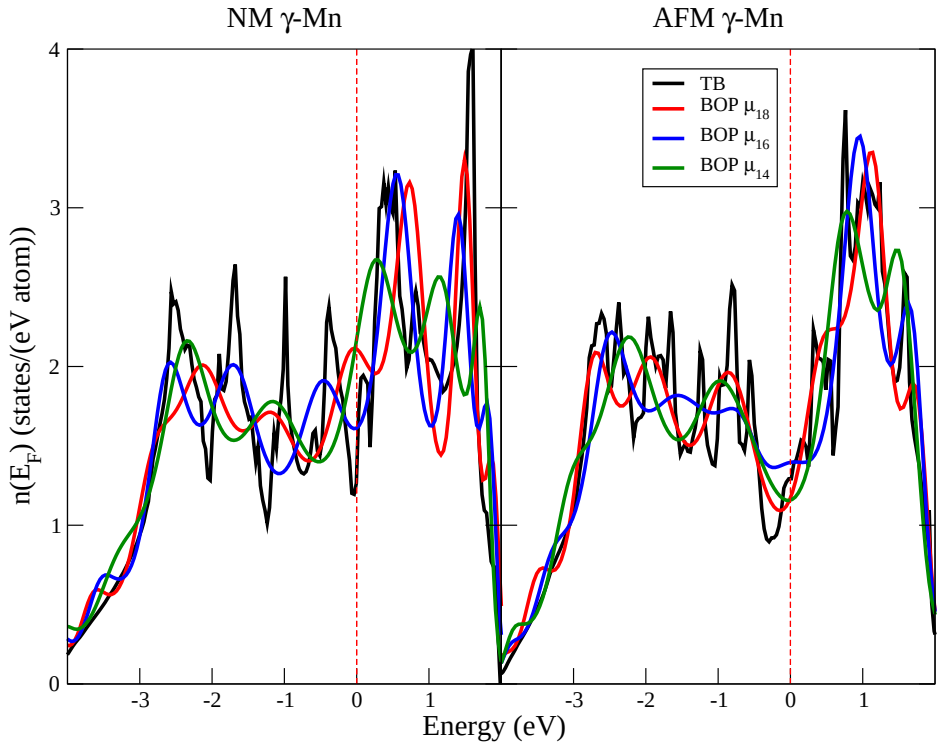

Figure 7.4: Densities of states for NM and AFM γ-Mn as calculated with TB and 14-, 16- and 18-moment BOP. The Fermi level is marked with a dotted line. The oscillations of the binding energy as a function of BOP moments for AFM γ-Mn which, with respect to those of the other structure types, were out-of-phase (as seen in Fig. 7.3) can be traced back to the differing behaviour of the DOS at the Fermi level. For example, for μ_{18} while a peak is observed in the DOS at E_F for NM γ-Mn, a trough is observed for AFM γ-Mn.

at $N_d = 5.7$, while the canonical model reproduces the behaviour of the 5d series, with hcp most stable at $N_d = 5.7$.

Given the findings of Chap. 6 it would be expected that the differing behaviour of the two TB models is due to the softness/hardness of their effective repulsive potentials. Differences in the bond integrals were assessed and found indeed to not play a critical role in affecting which of hcp or χ is preferentially stabilised at $N_d \sim 5.7$. For example using the canonical TB bond integrals with the repulsive and embedding potentials from the Mn TB model left the hcp-χ relative stabilities unchanged. Similarly the ratio of bond integrals from the Mn TB model measured at the first nearest neighbour distance in fcc γ-Mn, found to be -6.0:3.6:-0.5, was used with the repulsive function from the canonical TB model and this also left the hcp-χ relative stabilities unchanged.

The degree of normalised hardness α_h was then evaluated for both models. In Sec. 6.3 it was noted that using the canonical TB model the χ-phase was stabilised over hcp as α_h was decreased from around $\frac{1}{2}$ to $\frac{1}{3}$. For the canonical TB model the hardness parameter is given simply by $(m-1)/m$ such that in the case of $m = 2$ and $n = 4$, $\alpha_h = 0.500$. However more generally α_h is given by $(\lambda - 1)/\lambda$ where

$$\lambda = \left\{ \left[R\frac{d}{dR}(\ln \Phi_{rep}) \right] \Big/ \left[R\frac{d}{dR}(\ln \Phi_{bond}) \right] \right\}_{R=R_0}, \tag{7.7}$$

where $\Phi_{rep}(R)$ and $\Phi_{bond}(R)$ are the repulsive and bonding contributions to the potential. The degree of normalised hardness of the newly parameterised Mn TB model was evaluated using Eq. 7.7 and found to have a value of $\alpha_h = 0.329$. Thus, consistent with the findings of Chap. 6, the origin of the tendency of the two TB models to stabilise either hcp or the χ-phase can be traced back to a difference in the hardness of the effective repulsive potential. The reproduction of the Mn TB structural energy differences by BOP are shown in Fig. 7.6. The trends from the TB

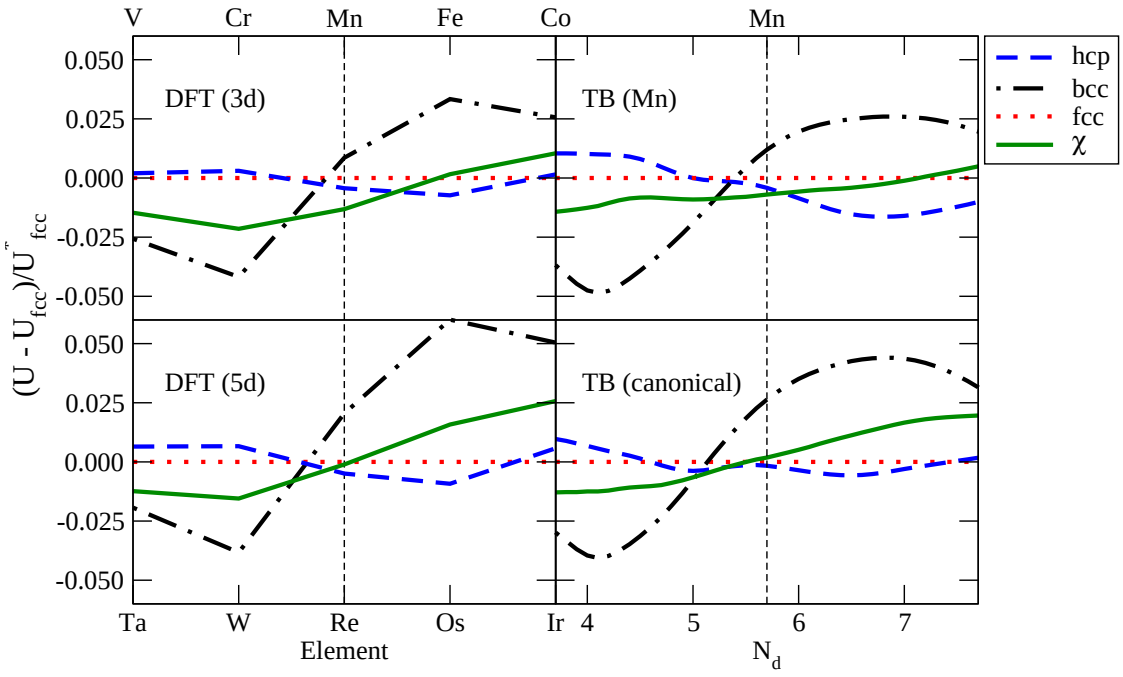

Figure 7.5: Left-hand panels - Structural energy differences calculated with DFT total energies for (upper left) $3d$ transition metals, V to Co, and (lower left) $5d$ transition metals, Ta to Ir. Right-hand panels - Structural energy differences calculated with TB bond energies using structural energy difference theorem (see Eq. 7.6) versus the number of d electrons N_d for (upper right) the Mn TB model detailed in this paper and (lower right) the canonical TB model detailed in Ref 228. The energies are normalised with respect to U^*_{fcc} which for the DFT calculations is the group VII fcc total energy and for the TB calculations is the fcc bond energy at $N_d = 5.7$ (the valence electron count for the Mn TB model).

model are reproduced very well in both the 20- and 14-moment calculations.

7.4 Relative Structural Stabilities of the Magnetic Phases of Mn

Having analysed the reproduction of the structural stabilities of the nonmagnetic phases that of the magnetic phases will now be examined. Referring to the DFT results in the left-hand panel of Fig. 7.1 it can be seen that with the inclusion of magnetism (curves marked with triangles) the relative stabilities of the phases are

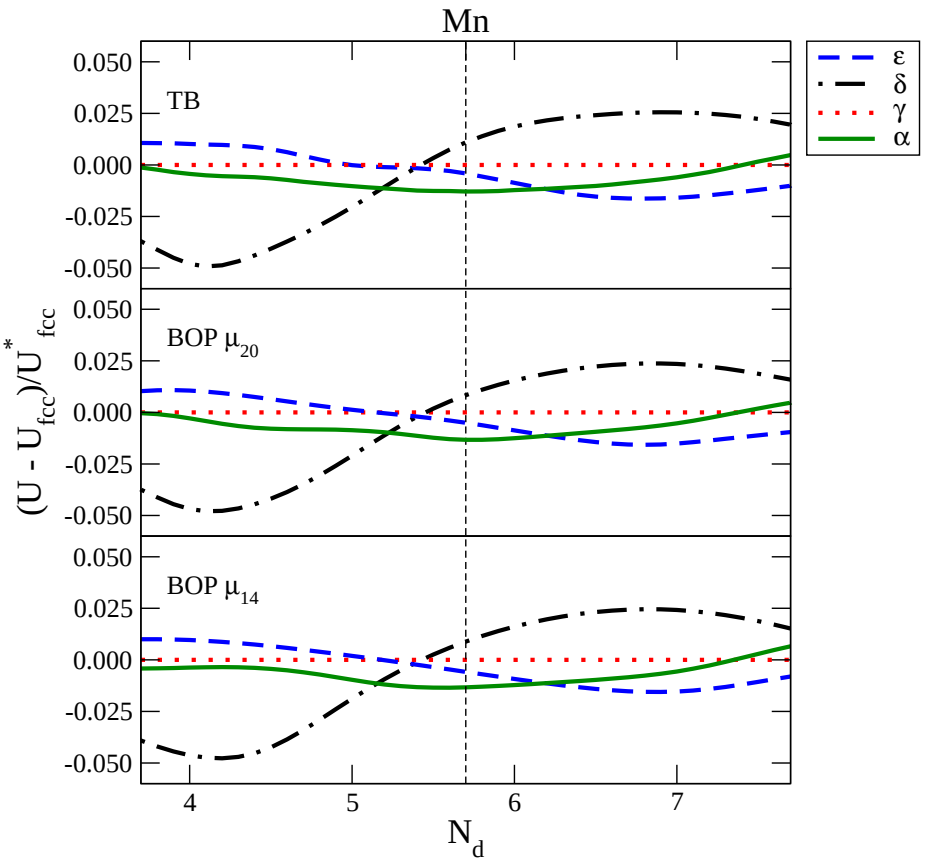

Figure 7.6: Mn structural energy differences versus the number of d electrons N_d for (upper panel) TB, (centre) 20-moment BOP and (lower) 14-moment BOP. The energies are normalised with respect to U^*_{fcc}, the fcc bond energy at $N_d = 5.7$.

left unchanged with the exception of AFM (fcc) γ, which is stabilised significantly with respect to its NM counterpart and which is predicted to become more binding than β and ϵ as a result. Within the DFT results the FiM β and AFM ϵ structures are virtually degenerate in energy with FiM β found to be just 1 meV more stable. Hafner and Hobbs[90] also predict these two structures to be very closely spaced in energy, but instead predict AFM ϵ-Mn to be 2 meV more stable than FiM β-Mn. This highlights just how difficult it is to calculate the small energy differences between the different Mn structures, even with accurate *ab initio* methods. The ordering of the magnetic phases as per my DFT calculations, namely $\alpha \rightarrow \gamma \rightarrow \beta \rightarrow \epsilon \rightarrow \delta$, is correctly reproduced by the TB and BOP models and the correct forms of magnetism

are stabilised i.e. complex collinear AFM in α-Mn, FiM in β-Mn and AFM in the other three structures. While the atomic volume at which the onset of magnetism occurs for α-, γ- and δ-Mn in the TB and BOP calculations is in good agreement with DFT, the FiM β- and AFM ϵ-Mn structures are only stabilised within TB and BOP at expanded atomic volumes.

Table 7.3 gives the energies of the magnetic phases relative to the AFM α-Mn ground state as well as the magnetic energy for each phase i.e. the difference in energy between the nonmagnetic and magnetic forms of the structure at their respective equilibrium volumes. It can be seen that the magnetic energies for α-Mn calculated using TB, 20-moment BOP and 14-moment BOP (25, 23 and 30 meV, respectively) are in good agreement with the DFT calculated value of 36 meV. Additionally the relative stabilities of the γ and ϵ phases, which are important in determining the prevalence of TRIP and TWIP plasticity mechanisms in Fe-Mn steels, are also well reproduced. The observation that it is only with the inclusion of magnetism that γ-Mn becomes more stable than ϵ-Mn demonstrates the importance of local magnetism in stabilising the fcc structure relative to hcp, just as Hasegawa and Pettifor first predicted for Fe at high temperatures[24]. Fig. 7.3 shows the convergence to the TB values of the AFM analytic BOP binding energies for fcc γ- and α-Mn. The convergence is systematic as the number of moments is increased.

The equilibrium atomic volumes of AFM α-Mn predicted by TB, 20- and 14-moment BOP are 1.65, 1.90 and 1.85 %, respectively, smaller than that predicted by DFT, differences which are slightly larger than for NM α-Mn. The DFT equilibrium atomic volume is 7 % smaller than the experimental atomic volume, reported as 12.05 Å by Lawson[77]. It has been noted previously that GGA is less successful in correcting overbinding in the LSDA in antiferromagnetic $3d$ metals than in ferromagnetic metals[6] and this is the cause of the larger disparity between DFT and experiment. Table 7.2 lists internal coordinates, relaxed using DFT , TB and BOP,

Allotrope	Magnetic state	Relative energy (meV/atom)			
		DFT	TB	BOP	
				μ_{20}	μ_{14}
α	AFM	0	0	0	0
	NM	36	25	23	30
	Mag. Energy	*36*	*25*	*23*	*30*
β	FiM	86	61	57	60
	NM	88	61	57	60
	Mag. Energy	*2*	*0*	*0*	*0*
γ	AFM	80	58	57	49
	NM	124	92	97	104
	Mag. Energy	*44*	*34*	*39*	*55*
δ	AFM2	155	120	111	107
	NM	199	170	157	169
	Mag. Energy	*44*	*49*	*46*	*62*
ϵ	AFM	87	63	63	66
	NM	89	63	63	66
	Mag. Energy	*2*	*0*	*0*	*0*
U_ϵ-U_γ	AFM	7	5	6	17
	NM	-35	-29	-34	-38

Table 7.3: Binding energies relative to the AFM α-Mn ground state for the nonmagnetic and magnetic forms of the five primary allotropes of Mn, calculated using DFT, TB, and 20- and 14-moment BOP. The magnetic energy, defined as $U_{NM}(V_{eq}^{NM}) - U_{Mag}(V_{eq}^{Mag})$, is given for each allotrope. The relative energies of the nonmagnetic and magnetic γ and ϵ phases are also given. The BOP calculations reproduce the results of the TB model reasonably well, while slightly larger differences are found between the DFT and TB results.

for the magnetic forms of α- and β-Mn. The TB relaxed internal coordinates for AFM α-Mn are closer to the DFT coordinates than their NM counterparts. The 14-moment, and 20-moment, BOP relaxed internal coordinates for AFM α-Mn are all very close to the TB values. At equilibrium volume the FiM β-Mn is only fractionally more stable than NM β-Mn and it can be seen from the two sets of DFT coordinates that their structures are very similar. In the TB model the FiM β-Mn state only becomes more stable than NM β-Mn at volumes a little above the equilibrium volume and so the two sets of coordinates are identical. This is also observed in the results of the 14- and 20-moment BOP calculations.

Table 7.4 lists the magnitudes of the magnetic moments for each structure calculated with DFT, TB, and 20- and 14-moment BOP at their respective, fully relaxed, equilibrium atomic volumes. The TB and BOP models are found to correctly reproduce the complex collinear antiferromagnetic magnetic structure of α-Mn. Not only are the correct parallel and anti-parallel alignments at each site correctly reproduced (as may be seen in Fig. 3.1 where the DFT (green arrows), TB (red arrows) and 14-moment BOP (blue arrows) magnetic moment vectors have been calculated using the DFT-relaxed atomic coordinates), but also the relative sizes of the magnetic moments at each site, which decrease from site I $\rightarrow$ II $\rightarrow$ III $\rightarrow$ IV, are correctly reproduced. This is in contrast to a number of published DFT results[81,79] which predict different alignments of the Mn I and/or Mn II moments. Additionally the TB and BOP models correctly predict that the site IV magnetic moment is virtually zero. The TB and BOP predictions of the size of the moments in AFM γ-Mn are in reasonable agreement with those of DFT while those for AFM2 δ-Mn are less good. This is because the TB and BOP models predict a too large equilibrium atomic volume for AFM2 δ-Mn which results in an overestimation of the equilibrium magnetic moment. As has been mentioned, while DFT predicts FiM β-Mn and AFM ϵ-Mn to be fractionally more stable than their NM counterparts, the TB and BOP models significantly stabilise magnetism within these two structure types only at volumes above $\sim$12 Å^3/atom for β-Mn and 11.5 Å^3/atom for ϵ-Mn . As a result the magnetic moments predicted at equilibrium volumes are zero in TB and virtually zero in BOP, whereas DFT predicts small but non-zero moments. The small disparities between TB and BOP result from differences in the shape of the DOS.

Allotrope	Magnetic state	Site	Local magnetic moments (μ_B/atom)			
			DFT	TB	BOP	
					μ_{20}	μ_{14}
α	AFM	I	2.97	3.27	3.34	3.32
		II	2.40	2.88	2.87	2.87
		III	1.39	1.38	1.16	1.70
		IV	0.02	0.06	0.08	0.08
β	FiM	I	0.11	0.00	0.01	0.04
		II	0.30	0.00	0.01	0.01
γ	AFM	I	1.98	2.37	2.26	2.26
δ	AFM2	I	1.58	2.47	2.32	2.36
ϵ	AFM	I	0.54	0.00	0.00	0.00

Table 7.4: Magnitudes of the local magnetic moments of Mn allotropes calculated with DFT, TB, and 20- and 14-moment BOP at their respective, fully relaxed, equilibrium atomic volumes.

7.5 Elastic Constants

Calculation of the elastic constants, which are given by the second derivative of the energy with respect to strain, is a sensitive test of the capabilities of an interatomic potential. Table 7.5 lists values of the bulk modulus (B_0), the tetragonal shear constant (C') and the trigonal shear constant (C_{44}) for the nonmagnetic and magnetic cubic Mn structures as calculated by applying appropriate strains to each unit cell[96]. Unlike the MEAM models[126,127] the TB and BOP model parameters were not explicitly fitted to any elastic constant data, although because the TB parameters were fitted to binding energies over a range of atomic volumes (see Sec. 7.2) values of the bulk moduli will be approximately reproduced. Additionally, the tetragonal shear constant C', a measure of the curvature of the Bain path between bcc and fcc structures and defined as $(C_{11} - C_{12})/2$, was implicitly inferred because differences in the equilibrium binding energies of the bcc δ and fcc γ structures were included in the fitting[248,249].

There is a scarcity of experimental data available for comparison and no DFT

Allotrope	Magnetic state	B_0 (GPa)				C' (GPa)				C_{44} (GPa)			
		DFT	TB	BOP		DFT	TB	BOP		DFT	TB	BOP	
				μ_{20}	μ_{14}			μ_{20}	μ_{14}			μ_{20}	μ_{14}
α	NM	280	237	257	235	133	57	55	47	88	41	37	30
	AFM	175	163	193	152	130	54	73	72	84	68	85	77
β	NM	269	256	256	259	51	40	37	21	94	78	86	70
	FiM	205	218	220	210	53	49	51	39	87	78	86	74
γ	NM	280	237	240	241	74	43	10	17	167	82	70	107
	AFM	155	166	179	189	50	64	77	75	93	80	101	110
δ	NM	284	248	250	248	30	-65	-45	-42	116	18	-32	4
	AFM2	148	72	111	97	25	-1	1	6	146	42	18	41

Table 7.5: Table of the elastic constants, B_0, C' and C_{44}, calculated using DFT, TB, and 20- and 14-moment BOP for the nonmagnetic and magnetic cubic Mn allotropes.

predictions of C' and C_{44} for any Mn phase have been published to my knowledge. The DFT predicted bulk moduli calculated for this thesis are in good agreement with those of Hafner and Hobbs[90] although some minor differences result because they calculated B_0 by fitting energies to the Birch-Murnaghan[250] equation and the Vinet equation of state[251] while mine were calculated directly from the two elastic constants C_{11} and C_{12}[96] using B $= \frac{1}{3}(C_{11} + 2C_{12})$. For example I calculate B_0 for AFM2 δ-Mn to be 148 GPa, whereas if I fit to the Birch-Murnaghan equation I obtain 166 GPa, which matches the value given by Hafner and Hobbs. My DFT calculations predict B_0 for collinear AFM α-Mn to be 175 GPa while Hafner and Hobbs predict a value of 188 GPa for their non-collinear AFM α-Mn. Both of these values are higher than experimentally determined ones, which show a significant spread. More recently published experimental values include 131[252], 137[253] and 158[95] GPa, while older values tend to be lower e.g. 60[206] and 93[254] GPa. Just like the other magnetic 3d transition metals where the bulk modulus is smaller than is expected from the skewed parabolic behaviour across the NM 4d and 5d series due to magnetic pressure[82,13], it can be seen in Table 7.5 that it is indeed the presence of magnetism and not the complex structure that leads to the softness of α-Mn. It is also seen that the inclusion of magnetism drives a softening of the bulk moduli in the other structure types and that this behaviour is correctly reproduced in the TB

and BOP models.

In general the reproduction of the DFT shear moduli C' and C_{44} by the TB model is less satisfactory than for B_0. For example for AFM α-Mn, while B_0 for TB is within 7 % of DFT, C' and C_{44} only within 58 % and 19 %, respectively. The TB model predicts all of the allotropes examined here to be mechanically stable with positive shear constants except for a small negative C' for AFM2 δ-Mn and a negative C' for NM δ-Mn. While in the DFT calculations of the tetragonal deformation pathway, i.e. the Bain pathway, the energy relating to the NM bcc δ-Mn structure lies in a small local minimum at the peak of a global maximum, thus its tetragonal shear constant C' has a small but positive value. In contrast, in the TB model this small local minimum is smeared out and the energy corresponding to the bcc structure lies at the top of the maximum, resulting in a tetragonal shear constant which is therefore negative. The same observations are made for AFM2 bcc δ-Mn. That a previous TB model[100] also, according to my calculations, predicted a negative C_{44} for AFM2 δ-Mn and a negative C' for FiM β-Mn indicates just how challenging it is to capture all of the characteristics and complexities of elemental Mn within a simple model.

Fig. 7.7 illustrates the convergence of the three cubic elastic constants for NM and AFM γ-Mn as a function of the number of moments used in BOP. It can be seen, by comparing with Fig. 7.3, that more moments are required to converge the elastic constants than are required to converge the binding energies[255]. Additionally from Fig. 7.7 it is evident that B_0 converges more quickly than the shear constants, C' and C_{44}. This is because C' and C_{44} rely on the convergence of the cancellation of oscillating force constants which extend out many levels into a structure[243,222]. Distortions caused by shearing also cause distortions of the Fermi surface, shown to be responsible for observed anomalies in the temperature dependence of shear constants in V, Nb, Ta, Pd and Pt[256,257], but because the BOP DOS are always smooth

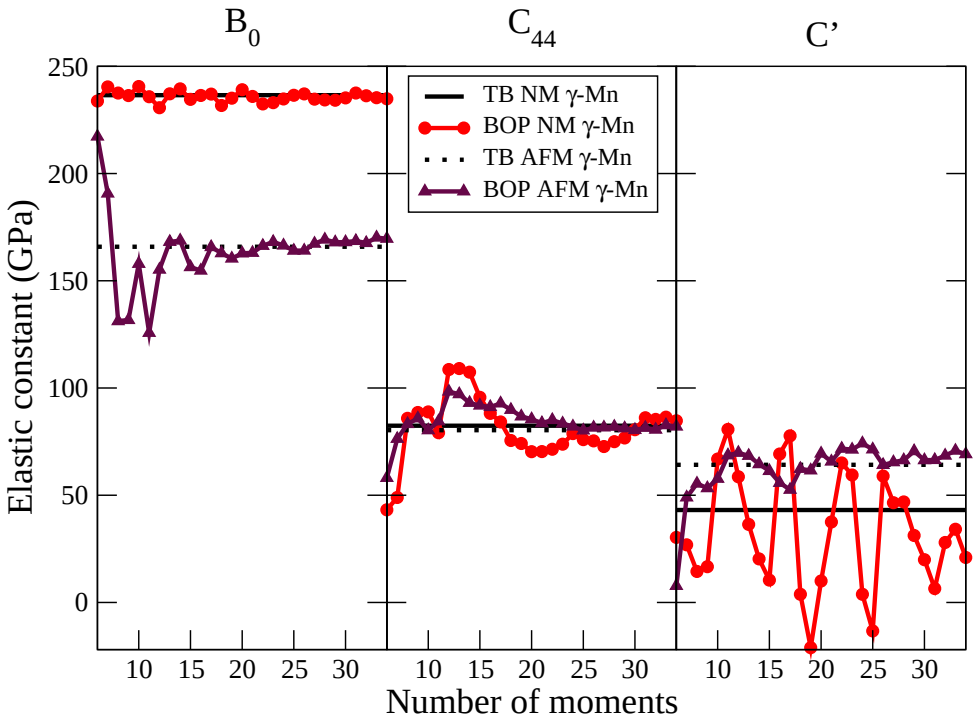

Figure 7.7: A plot of the convergence of BOP elastic constants to TB values for up to 34 exact moments, for NM and AFM γ-Mn.

the effects of these distortions on the fine structure of the DOS close to the Fermi level cannot be reproduced, even using a large number of moments. As a result accurate prediction of the shear constants is challenging. In particular, within the current model C' for NM γ-Mn oscillates strongly as a function of the number of BOP moments with, for example, a negative C' for 19- and 25-moment BOP. In Fig. 7.8 the DOS of NM γ-Mn with C' (centre panel) and C_{44} (right) strains applied, as calculated with TB, 25- and 26-moment BOP are given, along with the corresponding DOS for unstrained NM γ-Mn. It can be seen that the unstrained and strained DOS are very similar for all three sets of calculations and although the 26-moment BOP DOS are much closer to the TB DOS, it is difficult to discern why the reproduction of C' in 25-moment BOP is so much poorer than that of C_{44}. The one perhaps significant difference is a trough at $\sim$-1 eV in the 25-moment BOP DOS for C' in place of which a peak is found in the TB and 26-moment C' DOS. These features

are also found in the unstrained DOS. Given that the energy differences between the strained structures are typically very small ($\sim$0.5 meV/atom for C') these small discrepancies may be enough to cause the poor convergence of C' within BOP.

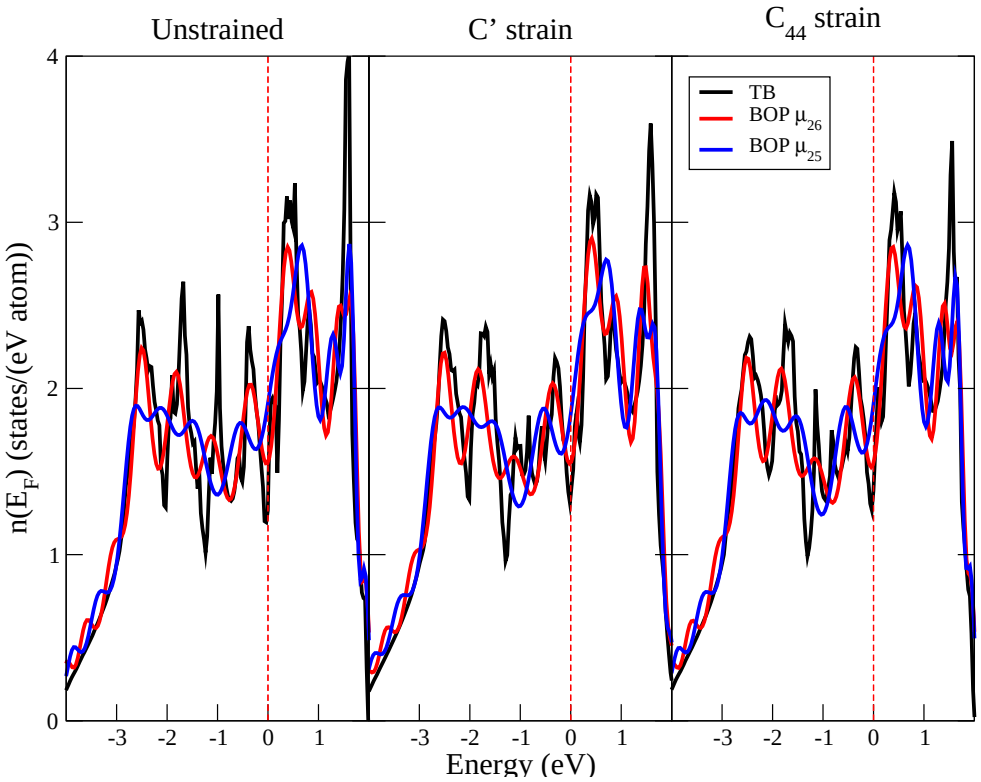

Figure 7.8: A plot of the DOS for NM γ-Mn with C' (centre panel) and C_{44} (right) strains applied, as calculated with TB, 25- and 26-moment BOP. The corresponding DOS for unstrained NM γ-Mn are shown in the left-hand panel. Only very small differences distinguish the strained DOS from the bulk DOS.

For hcp structures there are 5 independent elastic constants; C_{11}, C_{12}, C_{13}, C_{33} and C_{44}. These were calculated in the same way as the elastic constants for the cubic structure were except that strains appropriate to the hcp unit cells were applied[258]. For NM hcp ϵ-Mn the values of these elastic constants, in GPa, as calculated by DFT, TB, 20- and 14-moment BOP respectively are; C_{11} - 746, 502, 418, 465; C_{12} - 129, 196, 245, 207; C_{13} - 196, 218, 231, 228; C_{33} - 188, 132, 130, 130; and C_{44} - 156, 96, 92, 98 The resultant values of the bulk modulus are 303, 267, 265 and 264 GPa. For AFM hcp ϵ-Mn the values of these elastic constants, in GPa, as calculated

by DFT, TB, 20- and 14-moment BOP respectively are; C_{11} - 707, 502, 418, 465; C_{12} - 107, 196, 245, 207; C_{13} - 155, 218, 232, 230; C_{33} - 182, 132, 130, 130; and C_{44} - 156, 96, 92, 98 The resultant values of the bulk modulus are 270, 267, 265 and 266 GPa. Given that the TB and BOP models do not predict a stable AFM state for hcp until higher atomic volumes it is not surprising that the elastic constants for NM and AFM hcp are virtually identical. This is in contrast to the DFT results where small changes, e.g. a slight softening of the bulk modulus, are observed when magnetism is included.

7.6 Vacancy Formation Energies

The formation energies of a single vacancy were calculated using the supercell method[259] and the formula

$$U_f^{vac} = U_B^{vac} - \frac{N^{vac}}{N} U_B, \tag{7.8}$$

where N is the number of atoms in the perfect supercell, U_B is the binding energy of the perfect supercell, and N^{vac} and U_B^{vac} are those respective quantities for the vacancy-containing supercell, such that $N^{vac} = N - 1$. Tests of the convergence of the energy with respect to the supercell size showed that, in agreement with other calculations[260], 32-atom supercells were sufficient for γ-Mn and 54-atom supercells were sufficient for δ-Mn and ϵ-Mn. The 58- and 20-atom unit cell were shown to be sufficient for α- and β-Mn respectively.

Table 7.6 lists the unrelaxed and relaxed vacancy formation energies for the magnetic forms of α-, β-, γ-, δ- and ϵ-Mn as calculated with DFT, TB, and 20- and 14-moment BOP. DFT calculations predict that AFM2 bcc δ-Mn has the smallest relaxed single vacancy formation energy, with the β sites I and II and the α site IV having slightly larger energies, and then fcc γ, hcp ϵ and the α sites II, III and

Allotrope	Magnetic state	Site	Vacancy formation energy (eV/atom)							
			Unrelaxed				Relaxed			
			DFT	TB	BOP		DFT	TB	BOP	
					μ_{20}	μ_{14}			μ_{20}	μ_{14}
α	AFM	I	2.94	1.99	1.93	1.92	2.85	1.75	1.70	1.71
		II	2.81	1.83	1.85	1.81	2.60	1.45	1.44	1.39
		III	2.78	1.80	1.84	1.78	2.57	1.20	1.27	1.16
		IV	2.41	1.85	1.88	1.81	1.98	0.98	1.12	1.02
β	FiM	I	2.30	1.86	1.81	1.76	1.93	0.41	0.39	0.36
		II	2.23	2.02	2.03	1.97	2.05	0.73	0.59	0.76
γ	AFM	I	2.34	1.82	1.80	1.77	2.29	1.53	1.50	1.43
δ	AFM2	I	2.00	1.67	1.70	1.70	1.19	0.95	0.88	0.91
ϵ	AFM	I	2.55	2.06	2.04	2.04	2.42	1.04	1.03	1.03

Table 7.6: Unrelaxed and relaxed single vacancy formation energies calculated using DFT, TB, and 20- and 14-moment BOP, for the magnetic forms of α-, β-, γ-, δ- and ϵ-Mn.

IV having somewhat larger energies. This trend is also reflected in the unrelaxed vacancy formation energies.

For α-Mn there are four possible atoms which can be removed in order to create a vacancy. To the best of my knowledge in all of the examples found in the literature the site-specific details of the vacancy formation energy of α-Mn are either not given or not relevant to the level of theory used. For AFM α-Mn my DFT calculations predict that an unrelaxed vacancy created by the removal of a site IV Mn atom has the lowest formation energy followed by site III, site II and then site I. This trend is preserved upon structural relaxation around the vacancies and accompanied by a modest reduction of the formation energy. These trends are also observed for NM α-Mn indicating that they are a result of structural, rather than magnetic, effects. Indeed this ordering of the α-Mn vacancy formation energies reflects the local coordination, with the higher coordinated Z16 Mn I site having the largest vacancy formation energy, followed by the Z16 Mn II site, the Z13 Mn III site, and finally the lowest coordinated Z12 Mn IV site. This behaviour is consistent with the vacancy formation energy being proportional to a reduction in the cohesive energy caused by the loss of local coordination, which is proportional to the local coor-

dination number of the bulk structure z, scaling as $\sim \sqrt{(z-1)/z}$[260]. The TB and BOP models correctly predict the relative ordering of the relaxed U_f^{vac} at each α-Mn site, although for the unrelaxed vacancies TB and BOP predict the U_f^{vac} of site III to be smaller than that of site IV. The absolute TB and BOP values of U_f^{vac} for AFM α are all somewhat lower than their DFT counterparts however they are comparable to the values found in the literature for α-Mn, namely 0.93[261], 1.16[127] and 1.20[126] eV/atom.

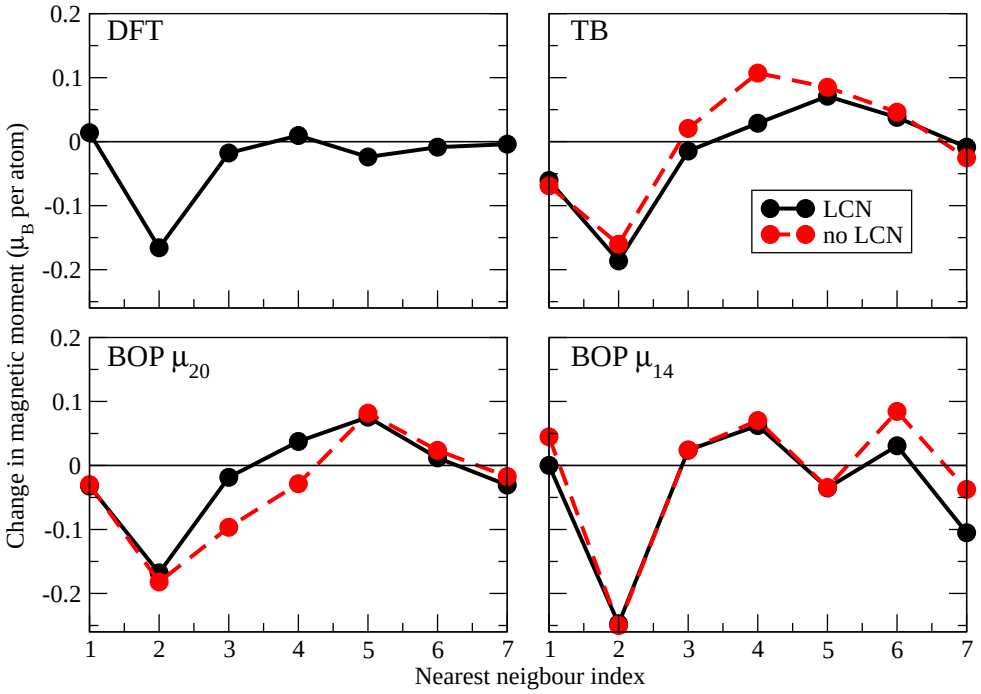

Figure 7.9: The change in local magnetic moments on nearest neighbours about a relaxed vacancy in an AFM α-Mn unit cell as calculated using DFT (upper left), TB (upper right), 20-moment BOP (lower left) and 14-moment BOP (lower right). The calculations with local charge neutrality (LCN) enforced (J_i = 8 eV) are solid black while those with no charge constraints are dashed red.

The changes in magnetic moment about a relaxed vacancy in AFM α-Mn are plotted in Fig. 7.9. For DFT there are significant changes in the magnetic moments of the first two nearest neighbour shells but only very small changes for atoms in

subsequent shells. For TB and BOP the plotted results include calculations both with (solid black lines) and without (dashed red lines) the constraint of local charge neutrality (LCN). It can be seen that in the plot of the TB results that enforcing LCN damps down the oscillations in the magnetic moments which gives better agreement with DFT for the third shell and beyond. This damping behaviour was also found to occur by Liu *et al.*[262] and Ford[225] in Fe vacancies. Notably however both results for the TB model predict a decrease in magnetic moment for the first nearest neighbour atom whereas DFT predicts a small increase. This difference may be due to the neglect of s electrons and sd hybridisation in the TB model or it may indicate that a more complex charge interaction is required in the TB model. However Soin and Horsfield[263] recently attempted to control charge transfer about an Fe vacancy by varying a Hubbard U term but concluded that it did not significantly improve the agreement with DFT of the vacancy formation energy. Alternatively it may be an effect of the lack of a unique projection method by which to determine the local charges and magnetic moments in the DFT calculations as implemented in VASP. The damping effects of enforcing LCN are reproduced in the 20-moment BOP calculation and the changes in magnetic moments of the locally charge neutral calculations is in good agreement with TB. However in the 14-moment BOP calculation the enforcement of LCN leads to a less conclusive effect and the agreement with the TB results both with and without LCN is rather poor.

Our DFT calculations show that for FiM β-Mn, of the two possible vacancy sites the lower-coordinated Z12 site I vacancy has a smaller relaxed formation energy than that of the Z14 coordinated site II. This is consistent with the observations of the effects of local coordination on the vacancy formation energies of the inequivalent sites in α-Mn. The TB and BOP models correctly predict this relative stability of the vacancy energies of two sites within FiM β-Mn, however a shortcoming of the models is that while the unrelaxed energies are reasonably close to the DFT

values, the relaxed values are significantly underestimated. We find that this is a result of the vacancy-containing β-Mn structure relaxing to a structure far from that predicted by DFT. For example in the DFT calculations the nearest neighbour distance in bulk FiM β-Mn is 2.29 Å and in the vacancy supercell it is 2.27 Å. However in the TB calculations while the nearest neighbour distance in the bulk supercell is 2.28 Å, in good agreement with DFT, in the vacancy supercell it is 2.04 Å. This, and the more modest underestimation in the α-Mn structure, may be due to the simple pair repulsion used in my model not being sufficient to model the nature of the bonding and forces in the vacancy-containing structures. This however could be mitigated by making the repulsive energy environment-dependent. For example in the numerical BOP for W developed by Mrovec *et al.*[264] the repulsive term was described by a screened Yukawa-type potential, the screening exponent of which was fitted to experimental data for bcc W to ensure the reproduction of the correct sign of the Cauchy pressure, thus allowing the BOP to be applied to the investigation of extended defects. Similarly Aoki *et al.*[265] applied the same principles in the parameterisation of numerical BOPs in order to model mechanical properties in hcp Ti and bcc Mo.

DFT predicts that for the three common crystal structures fcc, bcc and hcp, that AFM2 bcc δ-Mn has the smallest unrelaxed vacancy formation energy, with the close-packed AFM fcc γ-Mn and AFM hcp ϵ-Mn having larger energies. For AFM2 δ-Mn, just as for α- and β-Mn, it is found that there is a modest change in the vacancy formation energy upon relaxation of the supercell but in contrast, for the more compact fcc γ and hcp ϵ vacancy supercells the changes are much smaller, in agreement with the work of Willaime *et al.*[266]. While TB and BOP reproduce the relative ordering of the unrelaxed vacancy formation energies for these three structures, the relaxed vacancy formation energy for ϵ-Mn is anomalously small. Just as for β-Mn this is found to be due to the TB and BOP relaxed vacancy-containing struc-

tures having collapsed somewhat as compared to their DFT counterparts. Using a self-consistent Green's function method, Korzhavyi[260] calculated vacancy formation energies in magnetic γ- and δ-Mn, although they do not state the type of magnetic ordering considered for either structure. Additionally they neglected the effects of local lattice relaxations which, as shown for δ-Mn, can be significant. Their values of 1.51 eV/atom for δ-Mn and 2.51 eV/atom for γ-Mn are consistent with my unrelaxed vacancy formation energy results.

Overall while the TB and BOP models underestimate the absolute values of the DFT vacancy formation energies, they reproduce the relative trends between the inequivalent sites in both α- and β-Mn and predict larger values of U_f^V for the more close-packed γ and ϵ structures and smaller values for the more open α, β and δ.

7.7 Summary

An analytic BOP has been developed to investigate the structural and magnetic properties of elemental Mn at 0 K. It is derived within BOP theory directly from a new short-ranged orthogonal d-valent TB model of Mn, the parameters of which are fitted to reproduce the DFT binding energy curves of the experimentally observed phases of Mn, α, β, γ, δ, and ϵ-Mn. A recent version of analytic BOP by Seiser *et al.* [224] is used in order to guarantee that the density of states (DOS) is strictly positive across the entire band. Not only does the BOP reproduce qualitatively the DFT binding energy curves of the five different structure types, it also predicts the complex collinear antiferromagnetic (AFM) ordering in α-Mn, the ferrimagnetic (FiM) ordering in β-Mn and the AFM ordering in γ-, δ- and ϵ-Mn that are found by DFT. A BOP expansion including 14 moments is sufficiently converged to reproduce most of the properties of the TB model with the exception of the elastic shear constants which require further moments. The TB and BOP models correctly reproduce trends in

the relative sizes of the vacancy formation energies in the antiferromagnetic α-Mn ground state. However one limitation of the current model is that the absolute vacancy formation energies are somewhat smaller than those predicted by DFT. This is particularly true in the case of vacancies in the β-Mn structure and was found to be due to poor structural relaxation of the vacancy-containing structure possibly due to the lack of environmental dependence within the pairwise repulsion potential.

Chapter 8

Magnetic Analytic BOP for Fe-Mn

8.1 Introduction

In this chapter the details and results of new TB and BOP models for Fe and Fe-Mn will be given. A range of properties have been tested with respect to the results of reference DFT calculations including binding energies, elastic constants, vacancy formation energies and in the case of Fe-Mn the stacking fault energies.

8.2 Magnetic Analytic BOP for Fe

Before the Fe-Mn TB model could be parameterised an Fe TB model needed to be chosen, a number of which already exist in the literature. A model by Liu *et al.*[262] was shown to reproduce bulk DFT structural energy differences and provide reasonable predictions for the elastic constants, and vacancy and self-interstitial atom (SIA) formation energies. However it was reported separately by Ford[225] and by Soin & Horsfield[263] that they were unable to reproduce the results in Liu's paper with the parameters provided. A model by Mrovec *et al.*[227] was used to study dislocations in bcc Fe and has been shown to predict formation energies for a mono-

vacancy and for self-interstitial defects in good agreement with DFT and experiment. However this model was parameterised specifically for use within 9-moment numerical BOP calculations. There are also two distinct Fe TB parameterisations that have been published by collaborators at ICAMS. Madsen, McEniry *et al.* have published a shorter-ranged model[267] and another slightly longer-ranged one which was fitted to use with Fe-Cr and Fe-Mn binary TB models[100]. Ford used the shorter-ranged model within magnetic analytic BOP calculations to demonstrate how well they reproduced the results of exact TB calculations (see Chapter 5 of Ref. 225). However while this model had been previously shown to reproduce structural energy differences and vacancy formation energies with reasonable accuracy it was found that a number of features of the DFT reference data were rather poorly reproduced, most notably the SIA formation energies and the behaviour of the (100) surface upon relaxation[225]. While 9-moment BOP calculations reproduced the TB results for monovacancy and divacancy formation energies, in the case of the SIA formation energies it was found that 9- and 12-moment BOP calculations failed to find the same local magnetic states or the correct formation energies as predicted by TB. Additional complications meant that for both TB and BOP SIA calculations the forces on the atoms had to be relaxed first using an EAM model[125] before being further relaxed with TB and BOP. From my own tests using this Fe TB model I also found that χ-phase Fe structures did not relax successfully.

It was chosen initially, therefore, to use the parameters taken from the longer-ranged Fe TB model[100]. However it was soon found that the absolute binding energies in this Fe model were around 0.3 eV less stable than reference DFT energies, whereas the absolute binding energies in the Mn model described in Chap. 7 are only $\sim$0.03 eV less stable than DFT values. This difference resulted in Fe-Mn enthalpy of formation plots which were highly skewed, because the enthalpies of formation are of course given with respect to the Fe and Mn ground state ener-

gies. Therefore the decision was made to retain the bond integrals from the longer-ranged Fe model but to reparameterise the repulsive and embedding functions. In addition to rectifying the issue with the enthalpy of formation plot, reparameterising the Fe model meant that the same cut offs as were used in the Mn model could be used. These are slightly shorter than those used in the longer-ranged McEniry *et al.* model and are therefore consistent with the aim of performing fast, large-scale atomistic simulations. Furthermore the McEniry *et al.* model used the simpler form of the repulsive energy, i.e. only the first term in brackets on the left hand side of Eq. 7.3, so reparameterising it meant that the hard-core repulsion term, the second term in brackets on the left hand side of Eq. 7.3, could be included such that the functional forms and cut offs are consistent across all three of the Fe, Mn and Fe-Mn models.

8.2.1 Model Parameters

The parameters for the new Fe TB model are given in Table 8.1. The hard-core repulsion parameters used in the Mn model were used here and the values of c_{rep} and c_{emb} were fixed at 1.000 and 2.000, respectively, in line with the parameters of the other Fe TB models described above. The remaining repulsive and embedding parameters were then fitted to minimise errors in the TB binding energies with respect to the DFT energy-volume curves of the NM bcc, fcc and hcp Fe, FM bcc Fe and AFM fcc and hcp Fe for atomic volumes of between 8 and 14 Å^3. The range over which the bond integrals, repulsive energy and embedding energy all extend is controlled by the same cosine cut-off function with the same cut-off parameters as the Mn model. That is, the cut-offs are $R_{cut} = 4.5$ Å and $d_{cut} = 1.0$ Å for the bond integrals, and $R_{cut} = 5.5$ Å and $d_{cut} = 0.5$ Å for the repulsive and embedding functions. The results of binding energy, elastic constant, single vacancy formation energy and self-interstitial atom formation energy calculations using the new Fe

parameterisation are presented below for both TB and BOP. They have been compared with experimental results, DFT from the literature and the results of the TB and 9-moment BOP calculations of Ford[225].

Repulsive energy		
a_{rep} (eV)	b_{rep} (Å^{-1})	c_{rep}
1808.27	3.571	1.000
a_{hcr} (eV)	b_{hcr} (Å^{-1})	c_{hcr}
10000	0.01	15
Embedding potential		
a_{emb} (eV^2)	b_{emb} (Å^{-1})	c_{emb}
2.235	0.138	2.000
Bond integrals		
	a (eV)	b (Å^{-1})
$dd\sigma$	-32.180	1.585
$dd\pi$	68.065	2.050
$dd\delta$	-55.034	2.650
Stoner parameter		Electron count
I_d (eV)		N_d
0.74		6.8

Table 8.1: Fe TB model parameters: repulsive energy, embedding potential, bond integrals, Stoner parameter and electron count.

8.2.2 Binding Energies

Fig. 8.1 compares the binding energy curves for bcc, hcp and fcc Fe as calculated using DFT, the TB model of McEniry *et al.*[100], the newly developed TB model, and 9-moment BOP with the new model parameters. Firstly comparing the two TB models with respect to the DFT results, it can be seen that the correct ground state is reproduced within both TB models with the FM bcc stabilised over NM bcc by 0.38 eV/atom in the McEniry model and 0.35 eV/atom in the new TB model. These are both slightly smaller than the 0.48 eV/atom predicted by DFT. It can also be seen that both TB models show the overstabilisation of AFM hcp which was also a feature of the shorter-ranged Madsen *et al.* model. Ford[225] concluded that this

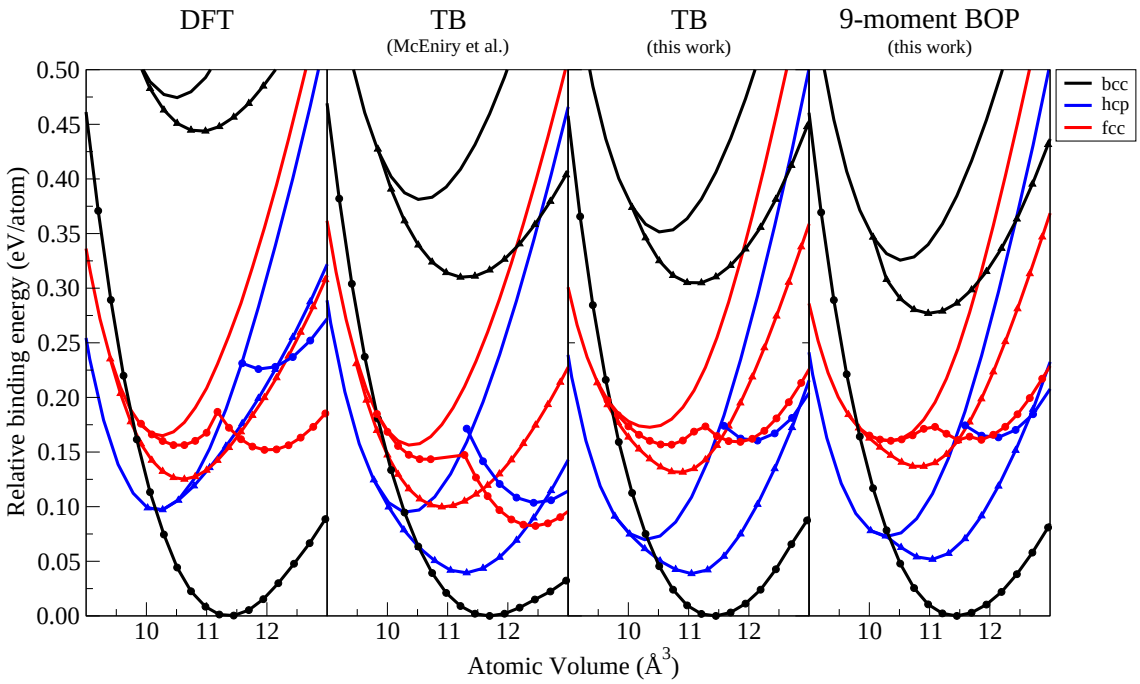

Figure 8.1: Binding energy curves for bcc, hcp and fcc Fe as calculated using (left to right) DFT, TB (McEniry *et al.* [100]), TB (this work) and 9-moment BOP (this work). The curves for AFM magnetic states are marked with triangles while those for FM states are marked with circles.

overstabilisation must be due to the poor shape of the TB DOS close to the Fermi level leading to a too high magnetic moment (see Fig. 5.9 of Ref. 225). The new TB model gives better agreement with respect to DFT for the magnetic phases of hcp and fcc, for example the low-spin to high-spin transition in FM fcc is better reproduced meaning that the FM fcc phase is correctly positioned with respect to the AFM fcc phase, and most importantly has absolute energies just 0.003 eV/atom lower than DFT, which are therefore consistent with the absolute energies of the Mn model.

Moving on to examine the 9-moment BOP, it can be seen that it clearly reproduces the most important features of the TB model and that it also reproduces the overstabilisation of the AFM hcp phase. The low-spin to high-spin transition in FM fcc are also distinguishable from the 9-moment BOP results which was not the case for 9-moment BOP calculations done using the short-ranged Madsen *et al.*

model[225]. The FM - NM energy difference for bcc is slightly smaller than in TB with a value of 0.325 eV/atom predicted.

8.2.3 Elastic Constants

The elastic constants for NM and FM bcc Fe, calculated for DFT, TB, and 14- and 9-moment BOP using the method that is outlined in Chap. 7, are listed in Table 8.2. The DFT results presented here are similar to DFT (FLAPW PBE) results[268] which found that for NM bcc $B_0 = 276$, $C' = -110$ and $C_{44} = 141$ and for FM bcc $B_0 = 186$, $C' = 69$ and $C_{44} = 99$, where all elastic constants are in GPa. Both sets of DFT calculations for FM bcc are in reasonable agreement with the results of ultrasonic pulse technique tests which when extrapolated to 0 K gave $B_0 = 173$, $C' = 53$ and $C_{44} = 122$ GPa[269].

For NM bcc Fe the TB model predicts a bulk modulus in good agreement with DFT but while it correctly predicts a negative C', which is to say that NM bcc Fe is unstable with respect to a tetragonal deformation, C' is somewhat too large and C_{44} somewhat too small. With respect to the BOP calculations the reproduction of the bulk moduli is better than that of C' and C_{44}, just as was found for the Mn model. For FM bcc Fe the TB model predicts all three elastic constants in good agreement with DFT. The value of the bulk modulus appears to be well converged by 14-moments while the agreement of C' is fortuitously excellent for both BOP models. However C_{44} is less well reproduced. In contrast Ford found that the description of the NM and FM bcc Fe elastic constants as calculated with BOP using the Madsen *et al.* model was poor, requiring many moments to converge towards the TB values. This was especially true for the trigonal shear constant C_{44}[225]. In addition using that model, TB predicts a negative C_{44} for NM bcc. He therefore concluded that such a BOP would need to be refitted specifically to reproduce the experimental or DFT elastic constants in order to perform realistic mechanical simulations, just as

Mrovec *et al.*[227] parameterised their 9-moment numerical BOP for Fe.

Structure	Magnetic state	B_0 (GPa)				C' (GPa)				C_{44} (GPa)			
		DFT	TB	BOP		DFT	TB	BOP		DFT	TB	BOP	
				μ_{14}	μ_9			μ_{14}	μ_9			μ_{14}	μ_9
bcc	NM	265	283	286	286	-117	-217	-151	-98	193	63	139	121
	FM	189	196	194	163	54	60	62	68	83	67	101	60

Table 8.2: Table of the elastic constants, B_0, C' and C_{44}, calculated using DFT, TB, and 14- and 9-moment BOP for nonmagnetic and ferromagnetic bcc Fe.

8.2.4 Defect Energy Calculations

Vacancy formation energies

The single vacancy formation energies for FM bcc Fe were calculated according to the method described in Sec. 7.6 using a 54 atom supercell. Table 8.3 lists the formation energies calculated using the new TB and BOP models (lower panel) alongside some reference DFT values and the values calculated by Ford using the Madsen *et al.* model (upper panel). The unrelaxed and relaxed vacancy formation energies calculated with TB are in good agreement with DFT although they are overestimated slightly and fall slightly outside the error bar for the experimental result. The TB values are closely reproduced by the 14- and 9-moment BOP. These results are comparable to those calculated by Ford using the Madsen *et al.* model, although it should be pointed out that in their paper Madsen *et al.* provide an additional set of parameters which more closely reproduces the DFT results, predicting a relaxed vacancy formation energy for FM bcc of 2.05 eV/atom. In comparison the results predicted by Liu's TB model[262], e.g. 1.65 eV for a relaxed vacancy in a 250 atom supercell, are quite poor.

	Vacancy formation energy (eV/atom)	
	Unrelaxed	Relaxed
Experiment[270]	-	2 ± 0.2
DFT (PAW PBE)[271]	-	2.16
TB (Madsen *et al.*)[225]	2.01	1.86
BOP μ_9 (Madsen *et al.*)[225]	2.09	2.02
TB	2.47	2.33
BOP μ_{14}	2.50	2.36
BOP μ_9	2.43	2.19

Table 8.3: Unrelaxed and relaxed single vacancy formation energies for FM bcc Fe. The reference DFT values are from calculations using the projector augmented wave (PAW) method[204,272].

Self-interstitial atom formation energies

Self-interstitial atom (SIA) defects can be modelled by inserting an atom into a supercell in a particular place and then allowing the supercell to relax. Within the bcc structure such defects can be inserted in a number of different ways resulting in dumbbell-shaped defects which lie along the $\langle 100 \rangle$, $\langle 110 \rangle$ and $\langle 111 \rangle$ crystallographic directions. There also exists a 'crowdion' SIA but this will not be considered here. Experimentally the lowest energy SIA in iron has been found by X-ray scattering experiments to be the $\langle 110 \rangle$ dumbbell[273]. This has been reproduced by DFT calculations of FM bcc Fe[274,275,271]. Firstly it should be noted that for the new Fe model the results were relaxed solely within either the TB or BOP calculations. In contrast Ford found that the large atomic forces present in the initial SIA supercells could not be relaxed using the Madsen *et al.* model and therefore it was necessary to first relax them using the EAM Fe Model of Dudarev & Derlet[125]. Table 8.4 lists the SIA formation energies calculated using the new TB and BOP models (lower panel) alongside some reference DFT values and the values calculated by Ford using the Madsen *et al.* model (upper panel). With respect to the results from the new Fe parameterisation it can be seen that the TB model predicts the correct ordering, namely $\langle 110 \rangle < \langle 111 \rangle < \langle 100 \rangle$ and that although still smaller than the DFT results,

the predicted energies are significantly closer to DFT than those of the other TB model. The results from the 9- and 14-moment BOP calculations are in qualitative agreement with both TB and DFT. Although the 9-moment BOP results are slightly smaller than the TB results they are significantly better than those calculated using the model of Madsen *et al.*

	SIA formation energy (eV/atom)		
	$\langle 100 \rangle$	$\langle 110 \rangle$	$\langle 111 \rangle$
DFT (US PW91)[274]	4.37	3.41	4.11
TB (Madsen *et al.*)[225]	2.67	2.16	2.25
BOP μ_9[225]	1.61	1.14	1.49
TB	3.85	3.00	3.37
BOP μ_{14}	3.74	2.92	3.21
BOP μ_9	3.17	2.31	2.92

Table 8.4: Relaxed self-interstitial atom formation energies for FM bcc Fe. The results from Ref. 274 are for 54 atom supercells using the ultrasoft pseudopotential (US) method[276] and the PW91 exchange-correlation functional.

8.2.5 Summary

While it was not one of the original aims of this thesis to develop a new TB or BOP model for Fe it was found that an existing, reliable TB parameterisation taken from the literature was not, with respect to parameterising an Fe-Mn model, compatible with the Mn model developed in Chapter 7. Using the new Fe TB model the reproduction of the DFT energies is in general good although, as is found for other related Fe TB models, AFM hcp is overstabilised. The trends in the DFT bcc elastic constants are also reproduced with, for example, the negative C' for NM bcc correctly predicted. Reproduction of the results of the TB model using a 9-moment BOP is very reasonable, although the elastic shear constants C' and C_{44} may require many more moments to converge.

For both TB and 9-moment BOP the relaxed vacancy energies are close to the experimental and DFT calculated values and the reproduction of the relative sta-

bilities of the $\langle 100 \rangle$, $\langle 110 \rangle$ and $\langle 111 \rangle$ SIA defects in FM bcc Fe is good. Indeed the formation energies for these SIA defects are superior to those of another TB model[267] tested recently[225] although the energies are still underestimated slightly compared to DFT calculated values. Importantly even in the presence of the large forces that occur when initiating a SIA calculation both TB and BOP calculations are able to correctly relax without the need to resort to using an EAM model. This could be due to the presence of an additional hard-core repulsive term which was originally introduced in the Mn model in order to stabilise structural relaxations of the χ-phase. The model is also relatively short-ranged and therefore is consistent with the aims of performing large-scale atomistic simulations with analytic BOP. However further calculations, examining for example divacancy formation energies and surface reconstruction, should be carried out in order to fully characterise the model if it is to be used to investigate the properties of Fe.

8.3 Magnetic Analytic BOP for Fe-Mn

8.3.1 Lowest Energy Fe-Mn Structures

It was necessary to establish the lowest energy Fe-Mn structures, with respect to magnetic ordering and chemical ordering, which would be used to fit the Fe-Mn TB model. DFT calculations for a range of hcp and fcc structures were therefore carried out. The investigation was restricted to ordered binaries allowing small unit cells to be used. In spite of the debate surrounding the ground state magnetic structure of fcc $Fe_{0.5}Mn_{0.5}$ in a combination of DFT and Monte Carlo simulations Comtesse *et al.* found that the energy difference between the lowest energy non-collinear and lowest energy collinear fcc $Fe_{0.5}Mn_{0.5}$ structures was just 3.41 meV/atom[277]. Furthermore Ekholm and Abrikosov found that the choice of GGA parameterisation affected whether a non-collinear or collinear ground state was predicted for fcc

$Fe_{0.5}Mn_{0.5}$[145]. Therefore within this work only collinear magnetic structures were considered.

For fcc $Fe_{0.5}Mn_{0.5}$ the CuAu $L1_0$ structure was found to be the ground state and the AFM collinear spin configuration matched that found in the literature[23,277]. In good agreement with the findings of others[277,182] relaxing the cell shape led to a tetragonal distortion corresponding to a c/a ratio of 1.02 but this was only 1.9 meV/atom more stable than the structure with a c/a ratio of 1.00. Throughout this work all Fe-Mn structures therefore have ideal c/a ratios. For fcc Fe_3Mn and $FeMn_3$ the lowest energy atomic arrangements, $L1_2$, and collinear spin configuration matched those reported in recent first-principles study of Fe-Mn alloys by Comtesse *et al.*[277]. For hcp structures four atom unit cells were also used and a range of atomic and magnetic configurations were investigated for the 25, 50 and 75 % Fe-Mn structures. Again only ideal c/a ratios were used. A number of χ-phase Fe-Mn structures with different compositions were also tested. These were created by starting with a pure Fe χ-phase structure and replacing all the site I, II, III or IV inequivalent atoms, and combinations thereof, with Mn. For bcc-based structure types only the $Fe_{0.5}Mn_{0.5}$ B2 structure was investigated.

8.3.2 Model Parameters

The parameters for the Fe-Mn TB model are given in Table 8.5. The functional form of the model is identical to that used for the Mn and Fe models, as is the cut-off function and cut-off parameters. The bond integrals used are taken from the Fe-Mn model of McEniry *et al.*[100]. It was found to be challenging to fit the model to reproduce reasonable SFE while also ensuring that the χ-phase structures, which are typically neglected in Fe-Mn TB models and interatomic potentials found in the literature, remain stable. As a results the hard-core repulsion parameters chosen for the Fe-Mn model are slightly different to those used in the Fe and Mn models.

These were fixed and then the repulsive and embedding parameters were fitted in the same way as for the Mn and Fe models. The TB energies were fitted to DFT energies of nonmagnetic and antiferromagnetic forms of ordered fcc and hcp with compositions $FeMn_3$, FeMn and Fe_3Mn.

Repulsive energy		
a_{rep} (eV)	b_{rep} (Å^{-1})	c_{rep}
520.00	3.308	0.848
a_{hcr} (eV)	b_{hcr} (Å^{-1})	c_{hcr}
100000	0.01	15.74
Embedding potential		
a_{emb} (eV^2)	b_{emb} (Å^{-1})	c_{emb}
-3.263	0.0671	2.754
Bond integrals		
	a (eV)	b (Å^{-1})
$dd\sigma$	-28.190	1.504
$dd\pi$	63.400	1.981
$dd\delta$	-52.414	2.575

Table 8.5: Fe-Mn TB model parameters: repulsive energy, embedding potential, bond integrals.

8.3.3 Formation Energy of Fe-Mn

When examining the relative energies of multi-component compounds it is intuitive to use the enthalpy of formation ΔH_f rather than total energies or binding energies. This may be approximated as

$$\Delta H_f \approx \Delta U_f = U^{(\mathrm{Fe_{1\text{-}x}Mn_x})} - (1-x)U^{(\text{FM bcc Fe})} - xU^{(\text{AFM } \alpha\text{-Mn})}, \tag{8.1}$$

where the formation energies are calculated with respect to the energies of the FM bcc Fe and AFM α-Mn ground states. The difference between ΔH_f and the total-energy differences of formation ΔU_f are mainly due to zero-point vibrational energies and may be assumed to be negligible because of cancellation[278].

The formation energies as calculated using DFT, TB and 14-moment BOP are presented in Fig. 8.2. First let us compare the DFT results to data found in the literature. In the left hand panel of Fig. 8.2. it can be seen that DFT calculations predict that on the Fe-rich side of the plot FM bcc is most stable while on the Mn-rich side AFM χ-phase is most stable. Accounts of χ-phase Fe-Mn are typically neglected in the literature, the rationale being that Mn-rich Fe-Mn structures are not relevant to the steels of interest. Nevertheless according to the trend in the DFT results it appears that AFM χ-phase Fe-Mn could be the most stable structure up to $\sim$30 % Fe. It is worth noting that it has been shown experimentally that as much as 33 at. % Fe is soluble in α-Mn with the alloy retaining the α-Mn structure below 700 °C[279]. Similarly experimentally bcc Fe-Mn structures have been reported for up to $\sim$13 % Mn[280]. In the centre of the plot AFM fcc structures are most stable. Furthermore comparing the nonmagnetic and magnetic data it is clear that magnetism plays an important role in stabilising the fcc and bcc structures but appears to play a smaller role in stabilising hcp structures. The minimum for the AFM fcc structures is found for the Fe_3Mn structure, i.e. it lies towards the Fe-rich side, in good agreement with experimental formation enthalpies measured using calorimetry at 873 K, 1073 K and 1443 K[281]. For the NM fcc-type structures the formation enthalpies of $FeMn_3$ and FeMn are very similar with that of Mn-rich $FeMn_3$ fractionally lower. Interestingly recent DFT calculations by Lintzen *et al.*, which include effects of disorder using special quasirandom structures (SQS), predict that for collinear AFM tetragonally distorted fcc structures the formation enthalpy minimum lies on the Mn-rich side[182]. Furthermore they predict the minimum in the NM fcc-type structure curve to occur at 100 % Mn. This suggests that disorder and tetragonal distortions of the fcc unit cell are important but it is strange that their results do not agree with any experimental results. Thermodynamic[9] and CALPHAD[172,182] assessments of formation enthalpies produce curves that have minima which lie at 50:50 compositions

or towards the Mn-rich side. Lintzen *et al.* also predict a region at ∼13-45 % Mn where magnetic hcp structures have the lowest formation enthalpies and predict that NM hcp has a lower formation enthalpy for ∼2-40 % Mn, which is not what my results show. Neglecting these differences both sets of DFT calculations predict the NM fcc is less stable than NM hcp across the whole composition range.

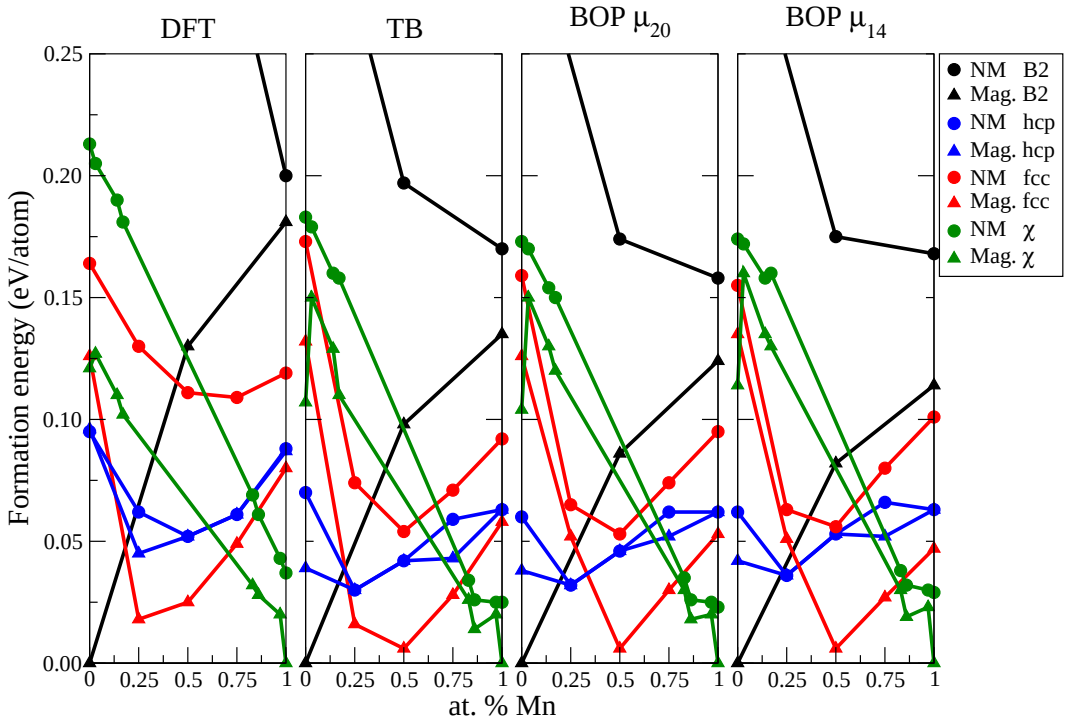

Figure 8.2: Formation energies for Fe-Mn structures and the respective elements plotted with respect to the energies of FM bcc Fe and AFM α-Mn.

Referring to the TB results in Fig. 8.2 it can be seen that the TB model correctly reproduces the most stable structure types as a function of increasing Mn concentration from FM bcc $\rightarrow$ AFM fcc $\rightarrow$ AFM χ. Importantly the ΔU_f for the NM fcc structures is much too low and this will have a significant effect on the NM SFE predicted by the TB model. The poor reproduction of the NM fcc energies is partly caused by an underestimation of the magnetic energy for the fcc structures. As a result it was challenging to fit both the NM hcp-fcc and AFM hcp-fcc energy differences and so the magnetic ones were prioritised. The magnetic energy is dependent

on the Stoner parameters used in the elemental Mn and Fe models. Rectifying this issue might require refitting the Mn model with a larger Stoner parameter or implementing an environmental dependence of the Stoner parameter. Refitting the bond integrals might also benefit the reproduction of the hcp-fcc energy differences. The assumption that N_d(Fe) and N_d(Mn) are constants and not environment dependent is also likely to contribute to the issues with fitting the Fe-Mn model. The other anomaly observable in the TB results is that AFM hcp for pure Fe is much too stable as was discussed in Sec. 8.2. The χ-phase structures are stable across the whole concentration range and while the formation energies for compositions with extreme high and low Mn concentrations are, with some minor discrepancies, reasonable those compositions close to 50:50 (not shown) give poorer agreement and are lower in energy than within DFT. This effect is due to poor structural relaxation in which the χ-phase structures relax into geometries dissimilar to those predicted by DFT. This was also an issue when parameterising the Mn model and was the reason why the hard-core repulsion term was introduced into the repulsive energy. While the poor reproduction of the χ-phase does not directly affect the ability of the model to reproduce the behaviour of the hcp and fcc structures it could indicate that tests in which significant relaxations are involved, such as defect energies, may also be poor. Additionally it again highlights the challenges of attempting to capture a wide range of complex characteristics within a relatively simple model.

The agreement of the 20- and 14-moment BOP models with TB is in general good with one exception. It can be seen that the BOP formation energies of the AFM fcc Fe_3Mn structure are far too high. This is because for AFM fcc Fe_3Mn the BOP calculations converge to a different, less stable, magnetic configuration compared to that obtained in the TB and DFT calculations. Indeed this happens in BOP calculations even with up to 30 exact moments, and using a higher number of fictitious moments, $n_{exp} = 249$, also fails to resolve the issue. This suggests that

the Fe-Mn model parameters may need to be reparameterised specifically for BOP rather than being simply taken from the TB parameterisation, a conclusion also reached by Ford[225] in his recent testing of the Fe TB model of Madsen *et al.*

8.3.4 Elastic Constants

Table 8.6 lists the elastic constants as calculated using DFT, TB and 20-moment and 14-moment BOP for NM B2 and for the NM and AFM states of the three fcc-type Fe-Mn structures. In the literature experimental measurements of the elastic constants of Fe-Mn systems can only be found for fcc $Fe_{0.60}Mn_{0.40}$. These were measured using the ultrasonic pulse-echo-overlap technique at room temperature and found $B_0 = 122$ GPa, $C' = 36$ GPa and $C_{44} = 142$ GPa[282]. In terms of the relative sizes of B_0, C' and C_{44} these are similar to the DFT predictions for the three fcc Fe-Mn structures in this work. A similar trend was found by Music *et al.*[283] who used DFT to study the elastic constants of Fe-Mn random binary alloys for Mn concentrations of up to 40 % Mn using the disordered local moments picture to include the effects of magnetism. For fcc Fe_3Mn they found $B_0 = 130$ GPa, $C' = 30$ GPa and $C_{44} = 135$, values which are all slightly smaller than those predicted by DFT calculations in this work.

The reproduction of the DFT elastic constants by the TB model displays similar trends to those observed for the Mn and Fe models. The bulk moduli are good, with B_0 for the magnetic structures softer than for nonmagnetic structures, but values of the shear constants C' and C_{44} are less well reproduced. For example while C' for the magnetic fcc structures are reasonable and the TB model correctly reproduces the negative C' for NM B2, the reproduction of C' for the NM fcc structures and the C_{44} in general are some way off the DFT values. The performance of the BOP calculations also mirrors what was observed for the Mn and Fe models again with quite rapid convergence to the TB bulk moduli but slower convergence for C' and

C_{44}.

Structure	Magnetic state	B_0 (GPa)				C' (GPa)				C_{44} (GPa)			
		DFT	TB	BOP		DFT	TB	BOP		DFT	TB	BOP	
				μ_{20}	μ_{14}			μ_{20}	μ_{14}			μ_{20}	μ_{14}
B2 FeMn	NM	267	266	270	268	-127	-100	-88	-76	141	46	115	96
fcc FeMn	NM	281	284	283	284	95	29	53	70	226	106	93	117
	AFM	171	203	-	-	77	72	43	71	167	114	93	128
fcc Fe_3Mn	NM	281	282	283	284	79	8	20	32	226	124	118	121
	AFM	138	203	239	236	66	56	66	83	180	130	122	135
fcc $FeMn_3$	NM	279	264	264	264	87	38	18	45	191	105	93	111
	AFM	147	162	183	185	43	49	54	68	207	152	143	149

Table 8.6: Table of the elastic constants, B_0, C' and C_{44}, calculated using DFT, TB, and 20- and 14-moment BOP for bcc and fcc phases of Fe-Mn.

8.3.5 Vacancy Formation Energies

The formation energy of a single vacancy U_f^{vac} has been calculated for $Fe_{0.5}Mn_{0.5}$ hcp and fcc as per the method given in Sec. 7.6. For Fe-Mn structures the vacancy can be created by removal of a either an Fe or a Mn atom. For the AFM fcc structure the spins on the Fe atoms are arranged ferromagnetically with respect to one another but the Mn atoms are arranged antiferromagnetically. Therefore an up- or down-spin Mn atom can be removed. For the hcp structure at equilibrium volume the ground state is only very slightly antiferromagnetic. As a result the nonmagnetic and antiferromagnetic vacancy energies are very similar and only the antiferromagnetic results are included here. Furthermore the spins on both Fe and Mn atoms are aligned antiferromagnetically such that whether an up- or down-spin atom is removed does not affect the final magnetic state or energy of the vacancy supercell. The results as calculated by DFT, TB and 20- and 14-moment BOP are listed in Table 8.7.

With respect to the results of the DFT calculations in all cases the formation energy of a vacancy by removal of a Fe atom is lower than that of a Mn atom. This is consistent with the Mn atoms, with a close to half-filled d band, being more

bonding. For the AFM fcc structure U_f^{vac} for a vacancy created by removal of an up-spin Mn atom, which has a magnetic moment aligned parallel with those of the Fe atoms, is smaller than that for the removal of a down-spin Mn atom. The change in energy upon relaxation of the vacancy-containing structures are modest.

The TB model qualitatively reproduces the features of the DFT results with U_f^{vac} for removal of an Fe atom smaller than that of a Mn atom. Furthermore for the AFM fcc structure the up-spin Mn atom vacancy formation energy is smaller than that of the down-spin Mn. However as was observed with the Mn model the absolute energies predicted by TB are somewhat smaller than DFT, and this is more pronounced for the relaxed, rather than unrelaxed, formation energies. The BOP calculations reproduce the tendency for U_f^{vac} for removal of an Fe atom to be smaller than that of a Mn atom and the absolute values for most of the calculated U_f^{vac} are in good agreement with TB. However for both 14- and 20-moment BOP the formation energies of the vacancies created by removal of an up- or down-spin Mn atom in AFM fcc FeMn are virtually identical, despite the underlying magnetic ordering in the final relaxed vacancy-containing structures being different.

Structure	Magnetic state	Vac. atom	Vacancy formation energy (eV/atom)							
			Unrelaxed				Relaxed			
			DFT	TB	BOP		DFT	TB	BOP	
					μ_{20}	μ_{14}			μ_{20}	μ_{14}
fcc	NM	Fe	2.14	1.39	1.40	1.47	1.99	0.77	0.80	1.00
		Mn	3.06	1.92	1.92	1.94	2.96	1.68	1.67	1.73
	AFM	Fe ↑	1.90	1.10	1.06	1.17	1.84	0.99	0.96	1.12
		Mn ↑	2.80	2.00	2.15	2.27	2.76	1.83	1.87	2.06
		Mn ↓	3.12	2.32	2.15	2.27	3.07	2.20	1.88	2.06
hcp	AFM	Fe	2.33	1.42	1.40	1.38	2.28	1.29	1.28	1.25
		Mn	3.01	1.93	1.95	2.00	2.95	1.87	1.89	1.92

Table 8.7: Unrelaxed and relaxed single vacancy formation energies for the non-magnetic and antiferromagnetic hcp and fcc structures of Fe-Mn at 50:50 composition.

8.3.6 Stacking Fault Energy

The axial next-nearest-neighbour Ising (ANNNI) model[178] has been used to evaluate the SFE. It has been used previously with *ab initio* methods to calculate the SFE in binary Fe-Mn[23] and quaternary FeCrNi-X austenitic stainless steels[151]. The ANNNI model approximates the intrinsic SFE as a series expansion of different infinitely repeating stacking sequences. To first order the SFE is given by the difference between the total energies (per atom) of idealised fcc and hcp crystals

$$\Gamma^1 = \frac{2(U^{hcp} - U^{fcc})}{A_{int}}, \tag{8.2}$$

evaluated at the fcc equilibrium volume, where A_{int} is the area of the fcc unit cell. This makes it a very simple way of evaluating the SFE requiring only calculations of the bulk hcp and fcc phases. Higher-order expansions include more complex structure types such as the double hcp phase which is included in the second-order ANNNI SFE

$$\Gamma^2 = \frac{(U^{hcp} + 2U^{dhcp} - 3U^{fcc})}{A_{int}}. \tag{8.3}$$

However the first-order expression has been found to reproduce with high accuracy the SFE in transition metals[284] and it is therefore used within this work.

The stacking fault energies as calculated using DFT, TB and 14-moment BOP are presented in Fig. 8.3. Examining first the results of the DFT calculations the trend predicted for the NM SFE matches very closely that predicted by Dick *et al.* in their calculations of ordered NM structures using the ANNNI model[23] with the minimum SFE occurring for 100 % Fe. While Dick *et al.* went on to examine the effects of disorder, which had the effect of making the SFE less negative and gave rise to a clear minimum at $\sim$25 % Mn, which is at least in qualitative agreement with experiment, they did not consider the effects of antiferromagnetic ordering. It can be seen in the DFT plot in Fig. 8.3 that including antiferromagnetism gives

rise to positive SFE for all of the structures investigated except for 100 % Fe. With the limited number of structures used it is difficult to compare the results with experiment except to point out that the SFE predicted for 25 % Mn, $\sim$200 mJ/m^2 is much larger than that predicted by experiment. It also appears from trends in finite temperature experimental results that the SFE for pure Fe is positive rather than negative[156,157]. There are a number of reasons that could be responsible for these disparities. Firstly, no compositional disorder has been considered here. Secondly, changes in the c/a ratio for the hcp and fcc structures, which have not been considered here, may affect the final SFE, although these effects are expected to be rather small. Thirdly, while this work assesses the SFE of defect-free, binary Fe-Mn the experimental Fe-Mn steels had small additions of carbon and other elements, and would have contained other defects. Finally, these calculations are for 0 K and no entropic contributions to the energy have been considered.

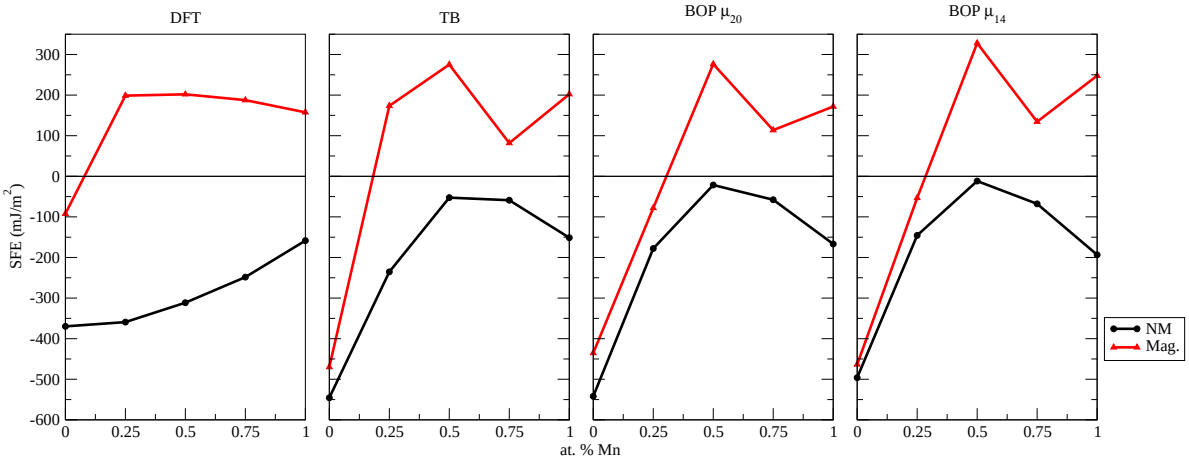

Figure 8.3: Stacking fault energies for binary Fe-Mn as calculated with DFT, TB and 20- and 14-moment BOP using the ANNNI[178] approach.

The TB model was parameterised with the reproduction of the magnetic SFE prioritised over that of the NM SFE. The values of the NM SFE predicted by the TB model are, discounting the SFE for 100 % Mn, rather poor with the trend as

a function of changing composition not reproduced. The magnetic SFE are better although for the Mn-containing structures the TB values oscillate around the relatively constants DFT values. Furthermore the TB model predicts a much larger negative SFE for pure Fe than DFT. This is a direct result of the anomalously stable AFM hcp structure predicted by the TB model. Despite the poor reproduction of the NM SFE the TB model still reproduces the correct qualitative differences between the NM and AFM SFE, with negative SFE predicted for NM structures and positive SFE predicted for all the magnetic structures except pure Fe. Therefore the effects of the presence or absence of magnetism as a function of temperature might still, in principle, be investigated using this model.

Finally, examining the results from the 20- and 14-moment BOP calculations it can be seen that the TB data points are reproduced with one significant inconsistency. For the AFM fcc Fe_3Mn structure the calculated SFE is negative rather than positive which is a direct result of the failure of the BOPs to reproduce the correct low energy magnetic state for this particular structure, as noted in Sec. 8.3.3. This, unfortunately, means that the current model would not be suitable for investigating the effects of the presence or absence of magnetism with increasing temperature with BOP, although it could be reparameterised specifically such that the BOPs reproduce the correct qualitative behaviour of the NM versus magnetic SFE.

8.3.7 Summary

A new Fe-Mn model for TB and BOP was parameterised by fitting to the total energies of a range of ordered Fe-Mn structures as calculated with DFT. The trends in the DFT formation energies are in agreement with experiment and other *ab initio* results, and where differences occur these are thought to be due largely to the neglect of chemical disorder in my calculations. The formation energies as calculated TB and BOP are reasonable with the trend in the lowest energy structure as a function

of Mn concentration correctly predicted. However nonmagnetic fcc-type structures are predicted to be too stable and within the BOP model only a higher energy magnetic state can be found for antiferromagnetic fcc Fe_3Mn. The reproduction of the elastic constants is reasonable for the structures tested with two key trends seen in the results for Mn and Fe also observed here. That is, the reproduction of the elastic shear constants can be quite poor and the convergence of the BOP elastic shear constants to TB values is slower than for the bulk moduli. General trends in the vacancy formation energies are correctly reproduced by both TB and BOP models but the absolute energies are somewhat smaller than in DFT.

Using the ANNNI model the NM SFE calculated with DFT are in good agreement with those found in the literature for ordered structures, predicting negative values of the SFE in contrast to experiment. However it is found that by including the effects of AFM ordering the SFE for all compositions tested, except pure Fe, become positive. Differences in the experimental SFE values and my results are likely due to the neglect of chemical disorder and the fact that the DFT calculations are valid for 0 K only. The reproduction of the SFE by the TB and BOP models is disappointing. Firstly, while the TB model reproduces the qualitative difference between SFE evaluated with and without magnetism, the trends as a function of increasing Mn concentration are not well reproduced. Furthermore both 20- and 14-moment BOP produce a negative SFE for antiferromagnetic fcc Fe_3Mn because of their failure to converge to the correct magnetic state. Thus the current BOP parameterisation would not be suitable for conducting large-scale atomistic calculations to investigate the effects of, for example, magnetism and temperature on the SFE. The BOP model could be refitted instead of using the parameters taken directly from the TB model. Alternatively, extending the TB model to include an environment-dependent Stoner parameter may be required to correctly capture both the magnetic and nonmagnetic behaviour of hcp and fcc Fe-Mn structures.

Chapter 9

Conclusions

In this thesis I have investigated why 3d Mn has a complex χ-phase ground state in contrast to the other group VII elements 4d Tc and 5d Re which are hexagonally close-packed. DFT calculations have confirmed that magnetism and the resulting effective atomic size difference are not the critical factors in driving the anomalous stability of the χ-phase in Mn. Additionally it has been shown that structural differences in the χ-phase geometry of the three elements and variations in the electronic structure are not significant enough to be responsible. Using a simple canonical TB model, which allows the effective potential to be varied in a transparent way, it was found that for a more than half-filled d-band harder potentials stabilise close-packed hcp whereas a softer potential stabilises the more open χ-phase. It is proposed therefore by analogy with the structural trend from open to close-packed phases down the group IV elements, that the anomalous stability of the χ-phase in Mn is due to 3d valent Mn lacking core d states and therefore having a softer repulsion than either 4d Tc and 5d Re.

Furthermore an analytic BOP has been derived from a new short-ranged, d-band, TB model and used to investigate the structural and magnetic properties of Mn. The analytic BOP model made use of a recent version of the analytic BOP ex-

pansion which guarantees a positive DOS across the whole band[224]. In spite of their simplicity the TB and BOP models not only qualitatively reproduce the small structural energy differences in the DFT binding energy curves of the five primary phases of Mn, but they also predict the complex collinear AFM ordering in α-Mn, the FiM ordering in β-Mn and the AFM ordering in γ-, δ- and ϵ-Mn that are predicted by DFT. Additionally the models correctly predict the relative ordering of the nonmagnetic structures such that χ-phase α-Mn is more stable than hcp, in contrast to 4d Tc and 5d Re in which hcp is the ground state structure. However, while the TB model reproduces trends in the bulk moduli observed in the DFT results the values of the elastic shear constants C' and C_{44}, which were not included in the fitting of the model, are poorer. Furthermore while a BOP expansion including 14 moments is sufficiently converged to reproduce most of the properties of the TB model, the elastic shear constants require, in some cases, significantly more moments. Improvements could be made to the model by including the elastic shear constants in the TB model parameterisation scheme or refitting the BOP model parameters directly to DFT data.

The TB and BOP models correctly reproduce trends in the relative sizes of vacancy formation energies in antiferromagnetic α-Mn but a limitation of the current model is that these energies are somewhat smaller than those predicted by DFT. This is particularly true in the case of vacancies in the β-Mn structure and was found to be due to poor structural relaxation of the vacancy-containing structure. An improved TB model might therefore include an environment dependent repulsive potential. Nevertheless the new Mn model captures the most important structural and magnetic features of the complex low energy Mn phases and the BOP model is suitable for performing large-scale dynamic simulations such that, for example, the local magnetic fluctuations with temperature that may be responsible for stabilising the different Mn phases at high temperatures could be investigated.

A new Fe TB model that is both reliable and compatible with the newly developed model for Mn has also been parameterised. The new model correctly reproduces trends in the structural stabilities of the common metallic structures, bcc, hcp and fcc, for Fe as predicted by DFT, except that, as is found for related Fe TB models such as that of Madsen *et al.*, antiferromagnetic hcp is overstabilised. Trends in the DFT elastic constants for bcc are also correctly reproduced with, for example, the negative C' for NM bcc correctly predicted. The reproduction of the TB results using a 9-moment BOP is very reasonable, although as was found for the Mn model the elastic shear constants C' and C_{44} may require many more moments to converge. For both TB and 9-moment BOP the relaxed vacancy energies are close to the experimental and DFT calculated values and the reproduction of the relative stabilities of the $\langle 100 \rangle$, $\langle 110 \rangle$ and $\langle 111 \rangle$ SIA defects in FM bcc Fe is good. Indeed the formation energies predicted for these SIA defects are superior to those of the model of Madsen *et al.* although the energies are still underestimated slightly compared to DFT-calculated values. Importantly even in the presence of the large forces that occur when initiating a SIA calculation both TB and BOP calculations are able to correctly relax. This is in contrast to the Madsen model for which TB and BOP forces had to be relaxed initially using an EAM model. This improved behaviour could be due to the presence of an additional hard-core repulsive term which was introduced in the newly developed Mn TB model in order to stabilise structural relaxations of the χ-phase. The new Fe model is also relatively short-ranged and therefore is consistent with the aims of performing large-scale atomistic simulations with analytic BOP. Further calculations, examining for example divacancy formation energies and surface reconstruction, should be carried out in order to fully characterise the model.

Using the Mn and Fe models a new Fe-Mn model for TB and BOP was parameterised. Trends in the DFT formation energies as a function of Mn concentration

are in good agreement with experiment and these are largely reproduced by TB and BOP. However nonmagnetic fcc-type structures are predicted to be too stable and within the BOP model only a higher energy magnetic state can be found for antiferromagnetic fcc Fe_3Mn.

Using the ANNNI model the NM SFE calculated with DFT are in good agreement with results found in the literature for ordered structures, predicting negative values of the SFE in contrast to experiment. However it is found that by including the effects of AFM ordering the SFE for all compositions tested, except pure Fe, become positive. Differences in the experimental SFE values and my results are likely due to the neglect of chemical disorder and the fact that the DFT calculations are valid for 0 K only. Unfortunately the reproduction of the SFE by the TB and BOP models is disappointing. While the TB model reproduces the qualitative difference between SFE evaluated with and without magnetism, the trends as a function of increasing Mn concentration are not well reproduced. Furthermore both 20- and 14-moment BOP produce a negative SFE for antiferromagnetic fcc Fe_3Mn because of their failure to converge to the correct magnetic state. Thus the current BOP parameterisation, while capturing a number of the important features of Fe-Mn, would not be suitable for conducting large-scale atomistic calculations to investigate the effects of, for example, magnetism and temperature on the SFE. This BOP model could be refitted independently, instead of using the parameters taken directly from the TB model, to ensure that the correct magnetic states are reproduced. However there is room for significant improvements to the TB model to be made as well. Further work might consist of extending what is currently a very simple TB model to include an environment-dependent Stoner parameter, which may provide the flexibility needed to correctly capture the magnetic energy differences, or an environment-dependent value of the electron count N_d. Additionally refitting the bond integrals might help to better reproduce the nonmagnetic hcp-fcc energy differences.

Bibliography

1. C. G. Shull and M. K. Wilkinson. Neutron diffraction studies of various transition elements. *Rev. Mod. Phys.*, 25:100–107, 1953.

2. Takemi Yamada. Magnetism and crystal symmetry of α-Mn. *J. Phys. Soc. Jap.*, 28(3):596–609, 1970.

3. Takemi Yamada, Nobuhiko Kunitomi, Yutaka Nakai, D. E. Cox, and G. Shirane. Magnetic structure of α-Mn. *J. Phys. Soc. Jap.*, 28(3):615–627, 1970.

4. L. Brewer. Bonding and structures of transition metals. *Science*, 161(3837):115–122, 1968.

5. D. G. Pettifor. *Bonding and structure of molecules and solids*. Oxford University Press, 1995.

6. D. Hobbs and J. Hafner. Understanding the complex metallic element Mn. I. crystalline and noncollinear magnetic structure of α-Mn. *Phys. Rev. B*, 68(1):014407, 2003.

7. Elizer Rapoport and George C Kennedy. Phase diagram of manganese to 40 kbars. *J. Phys. Chem. Solids*, 27(1):93–98, 1966.

8. A. Hellawell and W. Hume-Rothery. The constitution of alloys of iron and manganese with transition elements of the first long period. *Philos. Trans. R. Soc. Lond. A*, 249(968):417–459, 1957.

9. V. T. Witusiewicz, F. Sommer, and E. J. Mittemeijer. Reevaluation of the Fe-Mn phase diagram. *J. Phase Equil. Diffus.*, 25:346–354, 2004.

10. Q. Gu, J. Van Humbeeck, and L. Delaey. A review on the martensitic transformation and shape memory effect in Fe-Mn-Si alloys. *J. Phys. IV France*, 04:C3–135–C3–144, 1994.

11. A. Sato, E. Chishima, K. Soma, and T. Mori. Shape memory effect in $\gamma \rightleftharpoons \epsilon$ transformation in Fe-30Mn-1Si alloy single crystals. *Acta Metall.*, 30(6):1177 – 1183, 1982.

12. T. Schneider, M. Acet, B. Rellinghaus, E. F. Wassermann, and W. Pepperhoff. Antiferromagnetic Invar and anti-Invar in Fe-Mn alloys. *Phys. Rev. B*, 51(14):8917–8921, 1995.

13. R. W. Cahn, P. Haasen, and D. G. Pettifor. *Physical metallurgy*. North Holland, Amsterdam, 3rd edition, 1983.

14. M. Meyers and K. Chawla. *Mechanical Behavior of Materials*. Cambridge University Press, 2nd edition, 2009.

15. G. Frommeyer, E. J. Drewes, and B. Engl. Physical and mechanical properties of iron-aluminium-(Mn, Si) lightweight steels. *Rev. Met. Paris*, (10):1245–1253, 2000.

16. O. Grassel, L. Kruger, G. Frommeyer, and L. W. Meyer. High strength Fe-Mn-(Al, Si) TRIP/TWIP steels development – properties – application. *Intern. J. Plastic.*, 16(10-11):1391–1409, 2000.

17. G. Frommeyer. Supra-ductile and high-strength manganese-TRIP/TWIP steels for high energy absorption purposes. *ISIJ International (Iron and Steel Institute of Japan)*, 43(3):438–446, 2003.

18. S. Allain, J. P. Chateau, O. Bouaziz, S. Migot, and N. Guelton. Correlations between the calculated stacking fault energy and the plasticity mechanisms in Fe-Mn-C alloys. *Mater. Sci. Eng. A*, 387-389:158 – 162, 2004.

19. David Llewellyn and Roger Hudd. *Steels: Metallurgy and Applications: Metallurgy and Applications*. Butterworth-Heinemann, 1998.

20. G. J. L. Van Der Wegen, P. M. Bronsveld, and J. Th. M. De Hosson. A comparison between different theories predicting the stacking fault energy from extended nodes. *Scripta Metall.*, 14(2):285–288, 1980.

21. S. Curtze and V.-T. Kuokkala. Dependence of tensile deformation behavior of TWIP steels on stacking fault energy, temperature and strain rate. *Acta Mater.*, 58(15):5129–5141, 2010.

22. Raymond Edward Smallman and Ray J Bishop. *Modern physical metallurgy and materials engineering*. Butterworth-Heinemann, 1999.

23. A. Dick, T. Hickel, and J. Neugebauer. The effect of disorder on the concentration-dependence of stacking fault energies in Fe-Mn - a first principles study. *Steel Research International*, 80(9):603–608, 2009.

24. H. Hasegawa and D. G. Pettifor. Microscopic theory of the temperature-pressure phase diagram of iron. *Phys. Rev. Lett.*, 50(2):130–133, 1983.

25. Emilio Artacho, Daniel Sánchez-Portal, Pablo Ordejón, Alberto Garcia, and José M Soler. Linear-scaling ab-initio calculations for large and complex systems. *arXiv preprint cond-mat/9904159*, 1999.

26. Chris-Kriton Skylaris, Peter D Haynes, Arash A Mostofi, and Mike C Payne. Introducing onetep: Linear-scaling density functional simulations on parallel computers. *J. Chem. Phys.*, 122:084119, 2005.

27. Gabor Csányi, T. Albaret, M. C. Payne, and A. De Vita. Learn on the fly: a hybrid classical and quantum-mechanical molecular dynamics simulation. *Phys. Rev. Lett.*, 93(17):175503, 2004.

28. Murray S. Daw and M. I. Baskes. Embedded-atom method: Derivation and application to impurities, surfaces, and other defects in metals. *Phys. Rev. B*, 29(12):6443–6453, 1984.

29. M. W. Finnis and J. E Sinclair. A simple empirical n-body potential for transition metals. *Philos. Mag. A*, 50(1):45–44, 1984.

30. A. P. Sutton, M. W. Finnis, D. G. Pettifor, and Y. Ohta. The tight-binding bond model. *J. Phys. C*, 21(1):35–66, 1988.

31. W. Matthew C. Foulkes and Roger Haydock. Tight-binding models and density-functional theory. *Phys. Rev. B*, 39(17):12520–12536, 1989.

32. D. G. Pettifor. New many-body potential for the bond order. *Phys. Rev. Lett.*, 63(22):2480–2483, 1989.

33. Ralf Drautz and D. G. Pettifor. Valence-dependent analytic bond-order potential for transition metals. *Phys. Rev. B*, 74(17):174117, 2006.

34. Ralf Drautz and D. G. Pettifor. Valence-dependent analytic bond-order potential for magnetic transition metals. *Phys. Rev. B*, 84:214114, 2011.

35. P. M. Giles, M. H. Longenbach, and A. R. Marder. High-pressure $\alpha \rightarrow \epsilon$ martensitic transformation in iron. *J. Appl. Phys.*, 42(11):4290–4295, 1971.

36. R. J. Weiss and K. J. Tauer. Components of the thermodynamic functions of iron. *Phys. Rev.*, 102(6):1490–1495, 1956.

37. Larry Kaufman, E. V. Clougherty, and R. J. Weiss. The lattice stability of metals–III. iron. *Acta Metall.*, 11(5):323 – 335, 1963.

38. D. G. Pettifor. Theory of the crystal structures of transition metals. *J. Phys. C: Sol. State Phys.*, 3(2):367, 1970.

39. F. Ducastelle and F. Cyrot-Lackmann. Moments developments: II. application to the crystalline structures and the stacking fault energies of transition metals. *J. Phys. Chem. Solids*, 32(1):285 – 301, 1971.

40. P. Weiss. Hypothesis of the molecular field and ferromagnetic properties. *J. Phys*, 1907.

41. Ernst Ising. A contribution to the theory of ferromagnetism. *Z. Phys*, 31(1):253–258, 1925.

42. L. D. Landau and E. M. Lifshitz. *Quantum Mechanics*. Pergamon Press, New York, 3rd edition, 1976.

43. V. Heine and J. H. Samson. Magnetic, chemical and structural ordering in transition metals. *J. Phys. F*, 13(10):2155, 1983.

44. J. Kübler. Magnetic moments of ferromagnetic and antiferromagnetic bcc and fcc iron. *Phys. Lett. A*, 81(1):81 – 83, 1981.

45. Taru Moriya. Itinerant electron magnetism. *J. Magn. Magn. Mater.*, 31-34(Part 1):10 – 19, 1983.

46. P. Hohenberg and W. Kohn. Inhomogeneous electron gas. *Phys. Rev.*, 136(3B):B864–B871, 1964.

47. W. Kohn and L. J. Sham. Self-consistent equations including exchange and correlation effects. *Phys. Rev.*, 140(4A):A1133–A1138, 1965.

48. O. Gunnarsson and B. I. Lundqvist. Exchange and correlation in atoms, molecules, and solids by the spin-density-functional formalism. *Phys. Rev. B*, 13(10):4274–4298, 1976.

49. J. Callaway and C. S. Wang. The local exchange model of itinerant-electron ferromagnetism: Energy bands in nickel and iron. *Physica B+C*, 91:337 – 343, 1977.

50. V. L. Moruzzi, J. F. Janak, and A. R. Williams. *Calculated Electronic Properties of Metals*. Pergamon Press, New York, 1978.

51. O. K. Andersen, J. Madsen, U. K. Poulsen, O. Jepsen, and J. Kollr. Magnetic ground state properties of transition metals. *Physica B+C*, 86-88(Part 1):249 – 256, 1977.

52. Edmund C. Stoner. Collective Electron Ferromagnetism. II. Energy and Specific Heat. *Proc. R. Soc. Lond. A*, 169(938):339–371, 1939.

53. O. Gunnarsson and B. I. Lundqvist. Exchange and correlation in atoms, molecules, and solids by spin-density functional formalism. *Phys. Rev. B*, 13(10):4274–4298, 1976.

54. S. H. Vosko, J. P. Perdew, and A. H. MacDonald. Ab initio calculation of the spin susceptibility for the alkali metals using the density-functional formalism. *Phys. Rev. Lett.*, 35(25):1725–1728, 1975.

55. A. Gonis. *Theoretical Materials Science: Tracing the Electronic Origins of Materials Behaviou*. Mater. Res. Soc., 2000.

56. D. Jiles. *Introduction to Magnetism and Magnetic Materials*. Taylor and Francis, 1998.

57. G. Lonzarich and A. V. Gold. Temperature dependence of the exchange splitting in ferromagnetic metals I. information from the de Haas - van Alphen effect in iron. *Canadian Journal of Physics*, 52(8):694–703, 1974.

58. D. G. Pettifor. Electronic structure calculations and magnetic properties. *J. Magn. Magn. Mater.*, 15-18(Part 2):847 – 852, 1980.

59. S. Mukherjee and R. E. Cohen. Tight-binding based non-collinear spin model and magnetic correlations in iron. *J. Comput.-Aided Mat. Des.*, 8:107–115, 2001.

60. D. M. Roy and D. G. Pettifor. Stoner theory support for the two-state hypothesis for γ-iron. *J. Phys. F*, 7(7):L183–L187, 1977.

61. R. J. Weiss. The origin of the 'Invar' effect,. *Defense Technical Information Center OAI-PMH Repository [http://stinet.dtic.mil/oai/oai] (United States)*, 2001.

62. M. Shiga. Correlation between lattice constant and magnetic moment in 3d transition metal alloys. *AIP Conference Proceedings*, 18(1):463–477, 1974.

63. H. A. Mook, J. W. Lynn, and R. M. Nicklow. Temperature dependence of the magnetic excitations in nickel. *Phys. Rev. Lett.*, 30(12):556–559, 1973.

64. D. E. Eastman, F. J. Himpsel, and J. A. Knapp. Experimental band structure and temperature-dependent magnetic exchange splitting of nickel using angle-resolved photoemission. *Phys. Rev. Lett.*, 40(23):1514–1517, 1978.

65. M. Cyrot. Phase transition in Hubbard model. *Phys. Rev. Lett.*, 25(13):871–874, 1970.

66. S. H. Liu. Quasispin model for itinerant magnetism—effects of short-range order. *Phys. Rev. B*, 17(9):3629–3638, 1978.

67. Hideo Hasegawa. Single-site functional-integral approach to itinerant-electron ferromagnetism. *J. Phys. Soc. Jap.*, 46(5):1504–1514, 1979.

68. Paul Soven. Coherent-potential model of substitutional disordered alloys. *Phys. Rev.*, 156(3):809–813, 1967.

69. Hideo Hasegawa. Single-site spin fluctuation theory of itinerant-electron systems with narrow bands. *J. Phys. Soc. Jap.*, 49(1):178–188, 1980.

70. J. Hubbard. Magnetism of nickel. *Phys. Rev. B*, 23(11):5974–5977, 1981.

71. Taru Moriya. Temperature-induced local magnetic moment in narrow band electron systems. *Solid State Comm.*, 26(8):483 – 486, 1978.

72. M. Yu. Lavrentiev, D. Nguyen-Manh, and S. L. Dudarev. Magnetic cluster expansion model for bcc-fcc transitions in Fe and Fe-Cr alloys. *Phys. Rev. B*, 81(18):184202, 2010.

73. L. D. Landau and E. M. Lifshitz. *Statistical Physics*. Pergamon Press, New York, 3rd edition, 1980.

74. P.M. Derlet and S.L. Dudarev. Million-atom molecular dynamics simulations of magnetic iron. *Prog. Mater. Sci.*, 52(2-3):299 – 318, 2007.

75. F. C. Frank and J. S. Kasper. Complex alloy structures regarded as sphere packings. i. definitions and basic principles. *Acta Crystall.*, 11(3):184–190, 1958.

76. F. C. Frank and J. S. Kasper. Complex alloy structures regarded as sphere packings. II. analysis and classification of representative structures. *Acta Crystall.*, 12(7):483–499, 1959.

77. A. C. Lawson, Allen C. Larson, M. C. Aronson, S. Johnson, Z. Fisk, P. C. Canfield, J. D. Thompson, and R. B. Von Dreele. Magnetic and crystallographic order in α-manganese. *J. Appl. Phys.*, 76(10):7049–7051, 1994.

78. Hideki Yamagata and Kunisuke Asayama. NMR study of antiferromagnetic α-Mn metal. *J. Phys. Soc. Jap.*, 33(2):400–408, 1972.

79. V. Sliwko, P. Mohn, and K. Schwarz. The electronic and magnetic structures of α- and β-manganese. *J. Phys. Condens. Matt.*, 6(32):6557, 1994.

80. V. P. Antropov, M. I. Katsnelson, M. van Schilfgaarde, and B. N. Harmon. *Ab initio* spin dynamics in magnets. *Phys. Rev. Lett.*, 75(4):729–732, 1995.

81. T. Asada. Electronic structures and magnetism of α- and β-Mn. *J. Magn. Magn. Mater.*, 140-144(Part 1):47 – 48, 1995.

82. J. F. Janak and A. R. Williams. Giant internal magnetic pressure and compressibility anomalies. *Phys. Rev. B*, 14(9):4199–4204, 1976.

83. M. O'Keeffe and S. Andersson. Rod packings and crystal chemistry. *Acta. Crystall. A*, 33(6):914–923, 1977.

84. Ohad Levy, Michal Jahntek, Roman V. Chepulskii, Gus L. W. Hart, and Stefano Curtarolo. Ordered structures in rhenium binary alloys from first-principles calculations. *J. Amer. Chem. Soc.*, 133(1):158–163, 2011.

85. J. S. Kasper and B. W. Roberts. Antiferromagnetic structure of α-manganese and a magnetic structure study of β-manganese. *Phys. Rev.*, 101:537–544, 1956.

86. Y. Masuda, K. Asayama, S.-I. Kobayashi, and J. Itoh. Nuclear magnetic resonance in α- and β-manganese metals. *J. Phys. Soc. Jap.*, 19:460, 1964.

87. H Nakamura, K Yoshimoto, M Shiga, M Nishi, and K Kakurai. Strong antiferromagnetic spin fluctuations and the quantum spin-liquid state in geometrically frustrated β-Mn, and the transition to a spin-glass state caused by non-magnetic impurity. *J. Phys. Condens. Matt.*, 9(22):4701, 1997.

88. Benjamin Canals and Claudine Lacroix. Mean-field study of the disordered ground state in the β-Mn lattice. *Phys. Rev. B*, 61:11251–11254, 2000.

89. Y. Kohori, Y. Iwamoto, Y. Muro, and T. Kohara. NMR and NQR studies of β-Mn alloys. *Physica B*, 237-238(0):455 – 457, 1997.

90. J. Hafner and D. Hobbs. Understanding the complex metallic element Mn. II. geometric frustration in β-Mn, phase stability, and phase transitions. *Phys. Rev. B*, 68(1):014408, 2003.

91. Tamio Oguchi and A.J. Freeman. Magnetically induced tetragonal lattice distortion in antiferromagnetic fcc Mn. *J. Magn. Magn. Mater.*, 46(1-2):L1–L4, 1984.

92. Takeo Jo and Kunitomo Hirai. Lattice distortion and multiple spin density wave state in γ-Mn alloys. *J. Phys. Soc. Jap.*, 55(6):2017–2023, 1986.

93. Antiferromagnetism of γ-phase manganese alloys containing.

94. Yasuo Endoh and Yoshikazu Ishikawa. Antiferromagnetism of γ iron manganese alloys. *J. Phys. Soc. Jap.*, 30(6):1614–1627, 1971.

95. H. Fujihisa and K. Takemura. Stability and the equation of state of α-manganese under ultrahigh pressure. *Phys. Rev. B*, 52:13257–13260, 1995.

96. M. Finnis. *Interatomic forces in condensed matter, Chapter 7*. Oxford University Press, Oxford, 2003.

97. A. P. Horsfield, A. M. Bratkovsky, M. Fearn, D. G. Pettifor, and M. Aoki. Bond-order potentials: Theory and implementation. *Phys. Rev. B*, 53(19):12694–12712, 1996.

98. M. J. Mehl and D. A. Papaconstantopoulos. Application of a new tight-binding method for transition metals: Manganese. *EPL (Europhysics Letters)*, 31(9):537, 1995.

99. F. Süss and U. Krey. On the itinerant magnetism of Mn and its ordered alloys with Fe and Ni. *J. Magn. Magn. Mater.*, 125(3):351 – 362, 1993.

100. Eunan J McEniry, Georg K H Madsen, John F Drain, and Ralf Drautz. Tight-binding simulation of transition-metal alloys. *J. Phys. Condens. Matt.*, 23(27):276004, 2011.

101. K. W. Jacobsen, J. K. Norskov, and M. J. Puska. Interatomic interactions in the effective-medium theory. *Phys. Rev. B*, 35:7423–7442, May 1987.

102. F. Ducastelle and F. Cyrot-Lackmann. Moments developments and their application to the electronic charge distribution of d bands. *J. Phys. Chem. Solids*, 31(6):1295 – 1306, 1970.

103. G. Allan and M. Lannoo. Vacancies in transition metals: Formation energy and formation volume. *J. Phys. Chem. Solids*, 37(7):699 – 709, 1976.

104. Murray S. Daw, Stephen M. Foiles, and Michael I. Baskes. The embedded-atom method: a review of theory and applications. *Mater. Sci. Reports*, 9(7-8):251 – 310, 1993.

105. D. D. Koleske and S. J. Sibener. Molecular dynamics simulations of the basal planes of Ni and Cu using Finnis-Sinclair potentials. *Surface Sci.*, 290(1-2):179 – 194, 1993.

106. M. Yan, V. Vitek, and S. P. Chen. Many-body central force potentials and properties of grain boundaries in NiAl. *Acta Mater.*, 44(11):4351 – 4365, 1996.

107. A. Landa, P. Wynblatt, A. Girshick, V. Vitek, A. Ruban, and H. Skriver. Development of Finnis-Sinclair type potentials for Pb, Pb-Bi, and Pb-Ni systems: application to surface segregation. *Acta Mater.*, 46(9):3027 – 3032, 1998.

108. Q. Zhang, W. S. Lai, and B. X. Liu. Solid-state amorphization in Ni/Mo multilayers studied with molecular-dynamics simulation. *Phys. Rev. B*, 58:14020–14030, Nov 1998.

109. M. I. Baskes. Modified embedded-atom potentials for cubic materials and impurities. *Phys. Rev. B*, 46(5):2727–2742, 1992.

110. Byeong-Joo Lee and M. I. Baskes. Second nearest-neighbor modified embedded-atom-method potential. *Phys. Rev. B*, 62(13):8564–8567, 2000.

111. Byeong-Joo Lee, M. I. Baskes, Hanchul Kim, and Yang Koo Cho. Second nearest-neighbor modified embedded atom method potentials for bcc transition metals. *Phys. Rev. B*, 64(18):184102, 2001.

112. A. E. Carlsson. Angular forces in group-VI transition metals: Application to W (100). *Phys. Rev. B*, 44(13):6590, 1991.

113. S. M. Foiles. Interatomic interactions for Mo and W based on the low-order moments of the density of states. *Phys. Rev. B*, 48(7):4287, 1993.

114. G. C. Abell. Empirical chemical pseudopotential theory of molecular and metallic bonding. *Phys. Rev. B*, 31:6184–6196, May 1985.

115. J. Tersoff. New empirical approach for the structure and energy of covalent systems. *Phys. Rev. B*, 37:6991–7000, Apr 1988.

116. Donald W. Brenner. Empirical potential for hydrocarbons for use in simulating the chemical vapor deposition of diamond films. *Phys. Rev. B*, 42:9458–9471, Nov 1990.

117. L. Pauling. *The Nature of the Chemical Bond*. Cornell University Press, Ithaca, 3rd edition, 1960.

118. P. Alinaghian, P. Gumbsch, A. J. Skinner, and D. G. Pettifor. Bond order potentials: a study of s- and sp-valent systems. *J. Phys: Cond. Matt.*, 5(32):5795, 1993.

119. Walter A. Harrison. Transition-metal pseudopotentials. *Phys. Rev.*, 181:1036–1053, May 1969.

120. John A. Moriarty. Density-functional formulation of the generalized pseudopotential theory. III. transition-metal interatomic potentials. *Phys. Rev. B*, 38(5):3199–3231, 1988.

121. John A. Moriarty. Analytic representation of multi-ion interatomic potentials in transition metals. *Phys. Rev. B*, 42(3):1609–1628, 1990.

122. John A. Moriarty. Angular forces and melting in bcc transition metals: A case study of molybdenum. *Phys. Rev. B*, 49(18):12431–12445, 1994.

123. John A. Moriarty, James F. Belak, Robert E. Rudd, Per Söderlind, Frederick H. Streitz, and Lin H. Yang. Quantum-based atomistic simulation of materials properties in transition metals. *J. Phys: Cond. Matt.*, 14(11):2825, 2002.

124. Graeme J. Ackland. Two-band second moment model for transition metals and alloys. *J. Nucl. Mater.*, 351(1–3):20–27, 2006.

125. S. L. Dudarev and P. M. Derlet. A 'magnetic' interatomic potential for molecular dynamics simulations. *J. Phys. Condens. Matt.*, 17(44):7097, 2005.

126. Piero Torelli, Fausto Sirotti, and Pietro Ballone. Surface alloying and mixing at the Mn/Fe(001) interface: Real-time photoelectron spectroscopy and modified embedded atom simulations. *Phys. Rev. B*, 68:205413, 2003.

127. Young-Min Kim, Young-Han Shin, and Byeong-Joo Lee. Modified embedded-atom method interatomic potentials for pure Mn and the Fe-Mn system. *Acta Mater.*, 57(2):474–482, 2009.

128. Yoshimitsu Hirao, Junko Enomoto, and Hideko Tachikawa. (Tokyo) lead isotope ratios of copper, zinc and lead minerals in turkey-in relation to the provenance study of artifacts. *Essays on Ancient Anatolia and its Surrounding Civilizations*, 8:89, 1995.

129. H. K. D. H. Bhadeshia and R. Honeycombe. *Steels: Microstructure and Properties*. Butterworth-Heinemann, Elsevier, 3rd edition, 2006.

130. Herbert Fisher Moore. *Text-book of the materials of engineering*. McGraw-Hill, 8th edition, 1953.

131. Sharon Oster. The diffusion of innovation among steel firms: the basic oxygen furnace. *The Bell Journal of Economics*, pages 45–56, 1982.

132. E. P. Degarmo, J. T. Black, and R. A. Kohser. *Materials and Processes in Manufacturing*. Wiley International, USA, 9th edition, 2003.

133. World Steel Association. *Frequently Asked Questions*. http://www.worldsteel.org/faq/about-steel.html, Sept 2010.

134. B. C. De Cooman, K. G. Chin, and Jinkyung Kim. High Mn TWIP steels for automotive applications. *New Trends and Developments in Automotive System Engineering, InTech*, pages 101–128, 2011.

135. World Steel Association. *Advanced High Strength Steel (AHSS): Application Guidelines (Version 4.1)*. http://www.worldautosteel.org/Projects/AHSS-Guidelines.aspx, June 2009.

136. International Manganese Institute. *About Manganese: Introduction*. http://www.manganese.org, 2010.

137. Simon Dunstan and Ron Volstad. *Flak Jackets: 20th Century Military Body Armour*. Osprey Publishing, 1984.

138. Hua Ding, Zheng-You Tang, Wei Li, Mei Wang, and Dan Song. Microstructures and mechanical properties of Fe-Mn-(Al, Si) TRIP/TWIP steels. *J. Iron and Steel Res. Intern.*, 13(6):66 – 70, 2006.

139. Z. Gronostajski, A. Niechajowicz, and S. Polak. Prospects for the use of new-generation steels of the AHSS type for collision energy absorbing components. *Archives of Metallurgy and Materials*, 55(1):221–230, 2010.

140. B. C. De Cooman. *Review of Concepts for High Strength, High-Mn Steel: TWIP versus TRIP*. Materials Design Laboratory, Graduate Institute of Ferrous Technology, Pohang University of Science and Technology, 2010.

141. T. C. Schulthess, W. H. Butler, G. M. Stocks, S. Maat, and G. J. Mankey. Non-collinear magnetism in substitutionally disordered face-centered-cubic FeMn. *J. Appl. Phys.*, 85(8):4842–4844, 1999.

142. D Spišák and J Hafner. Magnetic structures in ordered and disordered γ-FeMn alloys: Ordering due to disorder. *Phys. Rev. B*, 61(17):11569, 2000.

143. Akimasa Sakuma. First-principles study on the non-collinear magnetic structures of disordered alloys. *J. Phys. Soc. Japan*, 69(9):3072–3083, 2000.

144. G. Malcolm Stocks, W. A. Shelton, Thomas C. Schulthess, Balazs Ujfalussy, W. H. Butler, and A. Canning. On the magnetic structure of γ-FeMn alloys. *J. Appl. Phys.*, 91(10):7355–7357, 2002.

145. Marcus Ekholm and I. A. Abrikosov. Structural and magnetic ground-state properties of γ-FeMn alloys from ab initio calculations. *Phys. Rev. B*, 84(10):104423, 2011.

146. J. A. Venables. The martensite transformation in stainless steel. *Philosophical Magazine*, 7(73):35–44, 1962.

147. Young G Kim, Yee S Park, and Jae K Han. Low temperature mechanical behavior of microalloyed and controlled-rolled Fe-Mn-Al-CX alloys. *Metallurgical and Materials Transactions A*, 16(9):1689–1693, 1985.

148. S. Cotes, M. Sade, and A. Guillermet. Fcc/hcp martensitic transformation in the Fe-Mn system: Experimental study and thermodynamic analysis of phase stability. *Metallurgical and Materials Transactions A*.

149. J. W. Christian. *The Theory of Transformations in Metals and Alloys (Part I + II), p. 286-288*. Elsevier Science, 2002.

150. Sebastien Allain, Jean-Philippe Chateau, and Olivier Bouaziz. Constitutive model of the TWIP effect in a polycrystalline high manganese content austenitic steel. *Steel Research*, 73(6-7):299–302, 2002.

151. Levente Vitos, J.-O. Nilsson, and Börje Johansson. Alloying effects on the stacking fault energy in austenitic stainless steels from first-principles theory. *Acta Mater.*, 54(14):3821–3826, 2006.

152. A.W. Ruff. Measurement of stacking fault energy from dislocation interactions. *Metallurgical Transactions*, 1(9):2391–2413, 1970.

153. T. Ericsson. The temperature and concentration dependence of the stacking fault energy in the Co-Ni system. *Acta Metall.*, 14(7):853–865, 1966.

154. L. Rémy. Temperature variation of the intrinsic stacking fault energy of a high manganese austenitic steel. *Acta Metall.*, 25(2):173–179, 1977.

155. L. Rémy, A. Pineau, and B. Thomas. Temperature dependence of stacking fault energy in close-packed metals and alloys. *Materials Science and Engineering*, 36(1):47–63, 1978.

156. H. Schumann. Einflu der stapelfehlerenergie auf den kristallographischen umgitterungsmechanismus der γ/α-umwandlung in hochlegierten sthlen. *Kristall und Technik*, 9(10):1141–1152, 1974.

157. P. Y. Volosevich, V. N. Grindnev, and Y. N. Petrov. Manganese influence on stacking-fault energy in iron-manganese alloys. *Phys. Met. Metallogr.*, 42:126, 1976.

158. Young-Kook Lee and Chongsool Choi. Driving force for γ to ϵ martensitic transformation and stacking fault energy of γ in Fe-Mn binary system. *Metallurgical and Materials Transactions A*, 31:355–360, 2000.

159. Kiyohito Ishida and Taiji Nishizawa. Effect of alloying elements on stability of epsilon iron. *Transactions of the Japan Institute of Metals*, 15:225–231, 1974.

160. R. Schramm and R. Reed. Stacking fault energies of seven commercial austenitic stainless steels. *Metallurgical and Materials Transactions A*.

161. J. P. Hirth. Thermodynamics of stacking faults. *Metallurgical Transactions*, 1(9):2367–2374, 1970.

162. G. Olson and Morris Cohen. A general mechanism of martensitic nucleation: Part III. kinetics of martensitic nucleation. *Metallurgical and Materials Transactions A*.

163. K. Ishida. Effect of alloying elements on the critical driving force of martensitic transformation in iron alloys. *Scripta Metall.*, 11(3):237 – 242, 1977.

164. O. Bouaziz and N. Guelton. Modelling of TWIP effect on work-hardening. *Mater. Sci. Eng. A*, 319-321:246 – 249, 2001.

165. J. C. Li, X. X. Lü, and Q. Jiang. Effect of alloying elements on stacking fault energy of iron-base shape memory alloys. *J. Mater. Sci. Lett.*, 18(20):1669–1670, 1999.

166. Jin Xuejun, Zhang Jihua, and T. Y. Hsu. Thermodynamic calculation of stacking fault energy in Fe-Mn-Si shape memory alloys. *Materials & Design*, 21(6):537–539, 2000.

167. A. Saeed-Akbari, J. Imlau, U. Prahl, and W. Bleck. Derivation and variation in composition-dependent stacking fault energy maps based on subregular solution model in high-manganese steels. *Metallurgical and Materials Transactions A*, 40(13):3076–3090, 2009.

168. Jinichiro Nakano and Pascal J. Jacques. Effects of the thermodynamic parameters of the hcp phase on the stacking fault energy calculations in the Fe–Mn and Fe–Mn–C systems. *Calphad*, 34(2):167–175, 2010.

169. W. S. Yang and C. M. Wan. The influence of aluminium content to the stacking fault energy in Fe-Mn-Al-C alloy system. *J. Mater. Sci.*, 25(3):1821–1823, 1990.

170. P. Gallagher. The influence of alloying, temperature, and related effects on the stacking fault energy. *Metallurgical and Materials Transactions B*, 1:2429–2461, 1970.

171. N. Saunders and A. P. Miodownik. *CALPHAD, Calculation of phase diagrams, a comprehensive guide*. Lavoisier, 1998.

172. W. Huang. An assessment of the Fe-Mn system. *Calphad*, 13(3):243–252, 1989.

173. P. Bisanti, G. Mazzone, and F. Sacchetti. Electronic structure of fcc Fe-Mn alloys. II. spin-density measurements. *J. Phys. F: Metal Phys.*, 17(6):1425, 1987.

174. Setsuro Asano and Jiro Yamashita. Band theory of antiferromagnetism in $3d$ f.c.c. transition metals. *J. Phys. Soc. Jap.*, 31(4):1000–1015, 1971.

175. J. Kübler, K.-H. Hock, J. Sticht, and A. R. Williams. Density functional theory of non-collinear magnetism. *J. Phys. F*, 18(3):469, 1988.

176. Shinpei Fujii, Shoji Ishida, and Setsuro Asano. Magnetic states in bcc manganese. *J. Phys. Soc. Jap.*, 60(4):1193–1196, 1991.

177. T. Hickel, A. Dick, B. Grabowski, and J. Neugebauer. Steel design from fully parameter-free ab initio computer simulations. *Steel Research International*, 80(1):4–8, 2003.

178. P. J. H. Denteneer and W. van Haeringen. Stacking-fault energies in semiconductors from first-principles calculations. *J. Phys. C: Solid State Phys.*, 20(32):L883, 1987.

179. Alex Zunger, S.-H. Wei, L. G. Ferreira, and James E. Bernard. Special quasirandom structures. *Phys. Rev. Lett.*, 65(3):353, 1990.

180. T. Gebhardt, D. Music, B. Hallstedt, M. Ekholm, I. A. Abrikosov, L. Vitos, and J. M. Schneider. Ab initio lattice stability of fcc and hcp Fe-Mn random alloys. *J. Phys. Condens. Matt.*, 22(29):295402, 2010.

181. T. Gebhardt, D. Music, Marcus Ekholm, I. A. Abrikosov, Levente Vitos, A. Dick, T. Hickel, J. Neugebauer, and J. M. Schneider. The influence of additions of Al and Si on the lattice stability of fcc and hcp Fe-Mn random alloys. *J. Phys: Cond. Matt.*, 23(24):246003, 2011.

182. Sarah Lintzen, Jörg von Appen, Bengt Hallstedt, and Richard Dronskowski. The Fe–Mn enthalpy phase diagram from first principles. *Journal of Alloys and Compounds*, 2013.

183. S. Akbar, Y. Kakehashi, and N. Kimura. A molecular dynamics approach to magnetic alloys with turbulent complex magnetic structures: γ-Fe-Mn alloys. *J. Phys. Condens. Matt.*, 10(9):2081, 1998.

184. V. Yamakov, D. Wolf, S. R. Phillpot, A. K. Mukherjee, and H. Gleiter. Deformation-mechanism map for nanocrystalline metals by molecular-dynamics simulation. *Nat. Mater.*, 3(1):43–47, 1994.

185. Furio Ercolessi and James B. Adams. Interatomic potentials from first-principles calculations: the force-matching method. *EPL (Europhysics Letters)*, 26(8):583, 1994.

186. Byeong-Joo Lee. A semi-empirical atomistic approach in materials research. *Journal of Phase Equilibria and Diffusion*, 30(5):509–516, 2009.

187. G. Dini, A. Najafizadeh, S. M. Monir-Vaghefi, and A. Ebnonnasir. Predicting of mechanical properties of Fe–Mn–(Al, Si) TRIP/TWIP steels using neural network modeling. *Comput. Mater. Sci.*, 45(4):959–965, 2009.

188. J. Muscat, A. Wander, and N. M. Harrison. On the prediction of band gaps from hybrid functional theory. *Chemical Physics Letters*, 342(3-4):397 – 401, 2001.

189. Max Born and Robert Oppenheimer. Zur quantentheorie der molekeln. *Annalen der Physik*, 389(20):457–484, 1927.

190. H. Hellman. *Einführung in die Quantenchemie*. Deuticke, 1937.

191. R. P. Feynman. Forces in molecules. *Phys. Rev.*, 56(4):340, 1939.

192. U. V. Barth and L. Hedin. Local exchange-correlation potential for spin polarized case. *J. Phys. C: Solid State Phys.*, 5(13):1629, 1972.

193. J. P. Perdew and A. Zunger. Self-interaction correction to density-functional approximations for many-electron systems. *Phys. Rev. B*, 23(10):5048–5079, 1981.

194. S. H. Vosko, L. Wilk, and M. Nusair. Accurate spin-dependent electron liquid correlation energies for local spin-density calculations - a criticial analysis. *Canadian Journal of Physics*, 58(8):1200–1211, 1980.

195. L. H. Thomas. The calculation of atomic fields. *Mathem. Proc. Camb. Philos. Soc.*, 23, 1927.

196. E. Fermi. Eine statistische methode zur bestimmung einiger eigenschaften des atoms und ihre anwendung auf die theorie des periodischen systems der elementet. *Zeitschrift fr Physik. A, Hadrons and nuclei*, 48(73), 1928.

197. J. Heyd, G. E. Scuseria, and M. Ernzerhof. Hybrid functionals based on a screened coulomb potential. *J. Chem. Phys.*, 118(18):8207–8215, 2003.

198. A. D. Becke. Density-functional exchange-energy approximation with correct asymptotic-behavior. *Phys. Rev. A*, 38(6):3098–3100, 1988.

199. C. T. Lee, W. T. Yang, and R. G. Parr. Development of the Colle-Salvetti correlation-energy formula into a functional of the electron-density. *Phys. Rev. B*, 37(2):785–789, 1988.

200. John P. Perdew, Kieron Burke, and Matthias Ernzerhof. Generalized gradient approximation made simple. *Phys. Rev. Lett.*, 77(18):3865–3868, 1996.

201. G. Kresse and J. Furthmüller. Efficiency of ab-initio total energy calculations for metals and semiconductors using a plane-wave basis set. *Comput. Mater. Sci.*, 6(1):15–50, 1996.

202. G. Kresse and J. Furthmüller. Efficient iterative schemes for *ab initio* total-energy calculations using a plane-wave basis set. *Phys. Rev. B*, 54:11169–11186, 1996.

203. Hendrik J. Monkhorst and James D. Pack. Special points for brillouin-zone integrations. *Phys. Rev. B*, 13(12):5188–5192, 1976.

204. P. E. Blöchl. Projector augmented-wave method. *Phys. Rev. B*, 50:17953–17979, 1994.

205. J. C. Slater and G. F. Koster. Simplified LCAO method for the periodic potential problem. *Phys. Rev.*, 94(6):1498–1524, 1954.

206. C. Kittel. *Introduction to Solid State Physics*. Wiley, New York, 1976.

207. D. G. Pettifor. Theory of energy bands and related properties of 4d transition metals. i. band parameters and their volume dependence. *J. Phys. F*, 7(4):613, 1977.

208. D. G. Pettifor. The tight-binding bond model. *Commun. Phys.*, 1:141–146, 1976.

209. A. R. Mackintosh and O. K. Andersen. *Electrons at the Fermi Surface*. Cambridge University Press, 1980.

210. A. J. Skinner and D. G. Pettifor. Transferability and the pair potential within the tight-binding bond model: an analytic study for hydrogen. *J. Phys. Cond. Matt.*, 3(13):2029, 1991.

211. M. Mrovec, D. Nguyen-Manh, D. G. Pettifor, and V. Vitek. Bond-order potential for molybdenum: Application to dislocation behavior. *Phys. Rev. B*, 69(9):094115, 2004.

212. S. Znam, D. G. Pettifor, V. Vitek, and D. Nguyen-Manh. Atomistic modelling of TiAl I. bond-order potentials with environmental dependence. *Philos. Mag.*, 83(4):415–438, 2003.

213. Marc J. Cawkwell, Duc Nguyen-Manh, Christopher Woodward, David G. Pettifor, and Vaclav Vitek. Origin of Brittle Cleavage in Iridium. *Science*, 309(5737):1059–1062, 2005.

214. C. Priester, G. Allan, and M. Lannoo. Tight-binding calculation of the band offset at the Ge-GaAs (110) interface using a local charge-neutrality condition. *Phys. Rev. B*, 33:7386–7388, May 1986.

215. O Gunnarsson. Band model for magnetism of transition metals in the spin-density-functional formalism. *J. Phys. F*, 6(4):587–606, 1976.

216. S. Asano and J. Yamashita. Ferromagnetism and antiferromagnetism in $3d$ transition metals. *Prog. Theor. Phys.*, 49:373–387, 1973.

217. J. Hubbard. Magnetism of iron. II. *Phys. Rev. B*, 20(11):4584–4595, 1979.

218. T. Hammerschmidt, B. Seiser, M. E. Ford, D. G. Pettifor, and R. Drautz. *BOPfox program for tight-binding and bond-order potential calculations*.

219. F. Cyrot-Lackmann. On the electronic structure of liquid transitional metals. *Advances in Physics*, 16(63):393–400, 1967.

220. Cornelius Lanczos. An iteration method for the solution of the eigenvalue problem of linear differential and integral operators. *J. Res. Nation. Bureau of Standards*, 45(4):255–282, October 1950.

221. Roger Haydock. The recursive solution of the schrdinger equation. *Comput. Phys. Comm.*, 20(1):11 – 16, 1980.

222. D. G. Pettifor and D. L. Weaire. *The Recursion Method and Its Applications*. Springer, Berlin, 1984.

223. Masato Aoki. Rapidly convergent bond order expansion for atomistic simulations. *Phys. Rev. Lett.*, 71(23):3842, 1993.

224. B. Seiser, D. G. Pettifor, and R. Drautz. Analytic bond-order potential expansion of recursion-based methods. *Phys. Rev. B*, 87:094105, 2013.

225. M. E. Ford. *D.Phil. Thesis, University of Oxford*. 2013.

226. M. E. Ford, Ralf Drautz, Thomas Hammerschmidt, and D. G. Pettifor. *In preparation*. 2013.

227. M. Mrovec, D. Nguyen-Manh, C. Elsässer, and P. Gumbsch. Magnetic bond-order potential for iron. *Phys. Rev. Lett.*, 106:246402, 2011.

228. B. Seiser, T. Hammerschmidt, A. N. Kolmogorov, R. Drautz, and D. G. Pettifor. Theory of structural trends within $4d$ and $5d$ transition metal topologically close-packed phases. *Phys. Rev. B*, 83:224116, 2011.

229. M. Nastar and F. Willaime. Tight-binding calculation of the elastic constants of fcc and hcp transition metals. *Phys. Rev. B*, 51(11):6896, 1995.

230. M.W. Finnis. Bond-order potentials through the ages. *Prog. Mater. Sci.*, 52(2-3):133 – 153, 2007.

231. Analytic bond-order potentials for modelling the growth of semiconductor thin films. *Prog. Mater. Sci.*, 52(2-3):196 – 229, 2007.

232. M. Abramowitz and I.A. Stegun. *Handbook of Mathematical Functions with Formulas, Graphs, and Mathematical Tables. National Bureau of Standards Applied Mathematics Series 55. Tenth Printing.* ERIC, 1972.

233. A. F. Voter, J. D. Kress, and R. N. Silver. Linear-scaling tight binding from a truncated-moment approach. *Phys. Rev. B*, 53:12733–12741, 1996.

234. R. N. Silver, H. Roeder, A. F. Voter, and J. D. Kress. Kernel polynomial approximations for densities of states and spectral functions. *J. Comput. Phys.*, 124(1):115–130, 1996.

235. M. Cák, T. Hammerschmidt, and R. Drautz. Comparison of analytic and numerical bond-order potentials for W and Mo. *J. Phys. Condens. Matt.*, 25(26):265002, 2013.

236. Alexander Weiße, Gerhard Wellein, Andreas Alvermann, and Holger Fehske. The kernel polynomial method. *Rev. Mod. Phys.*, 78(1):275, 2006.

237. R. Steadman and P. M. Nuttall. phase in a niobium-rhenium alloy. *Acta Crystallographica*, 17(1):62–63, 1964.

238. O. K. Andersen, W. Klose, and H. Nohl. Electronic structure of Chevrel-phase high-critical-field superconductors. *Phys. Rev. B*, 17:1209–1237, 1978.

239. R. Drautz, D. A. Murdick, D. Nguyen-Manh, X. Zhou, H. N. G. Wadley, and D. G. Pettifor. Analytic bond-order potential for predicting structural trends across the sp-valent elements. *Phys. Rev. B*, 72(14):144105, 2005.

240. J. C. Cressoni and D. G. Pettifor. Theory of structural trends within the sp bonded elements. *J. Phys. Condens. Matt.*, 3(5):495–511, 1991.

241. A. Urban, M. Reese, M. Mrovec, C. Elsässer, and B. Meyer. Parameterization of tight-binding models from density functional theory calculations. *Phys. Rev. B*, 84:155119, 2011.

242. D. G. Pettifor. Accurate resonance-parameter approach to transition-metal band structure. *Phys. Rev. B*, 2(8):3031, 1970.

243. M. W. Finnis, K. L. Kear, and D. G. Pettifor. Interatomic forces and phonon anomalies in bcc $3d$ transition metals. *Phys. Rev. Lett.*, 52:291–294, 1984.

244. H. Hasegawa, M. W. Finnis, and D. G. Pettifor. A calculation of elastic constants of ferromagnetic iron at finite temperatures. *J. Phys. F: Metal Phys.*, 15(1):19, 1985.

245. Gernot Stollhoff, Andrzej M. Oleś, and Volker Heine. Stoner exchange interaction in transition metals. *Phys. Rev. B*, 41:7028–7041, 1990.

246. John P. Perdew, J. A. Chevary, S. H. Vosko, Koblar A. Jackson, Mark R. Pederson, D. J. Singh, and Carlos Fiolhais. Atoms, molecules, solids, and surfaces: Applications of the generalized gradient approximation for exchange and correlation. *Phys. Rev. B*, 46(11):6671, 1992.

247. D. G. Pettifor. The structures of binary compounds. I. phenomenological structure maps. *J. Phys. C: Solid State Phys.*, 19(3):285, 1986.

248. P. J. Craievich and J. M. Sanchez. Vibrational free energy in the Ni-Cr system. *Comput. Mater. Sci.*, 8(1-2):92–99, 1997.

249. M. Sob, L. G. Wang, and V. Vitek. Local stability of higher-energy phases in metallic materials and its relation to the structure of extended defects. *Comput. Mater. Sci.*, 8(1-2):100–106, 1997.

250. F. D. Murnaghan. The compressibility of media under extreme pressures. *Proceedings of the National Academy of Sciences*, 30(9):244–247, 1944.

251. Pascal Vinet, John R. Smith, John Ferrante, and James H. Rose. Temperature effects on the universal equation of state of solids. *Phys. Rev. B*, 35:1945–1953, 1987.

252. K. Takemura, O. Shimomura, K. Hase, and T. Kikegawa. The high-pressure equation of state of α-Mn to 42 GPa. *J. Phys. F*, 18(2):197, 1988.

253. N. Mori, M. Takahashi, and G. Oomi. Magnetic contribution to the bulk modulus of $3d$-transition metal alloys. *J. Magn. Magn. Mater.*, 31-34, Part 1(0):135 – 136, 1983.

254. M. Rosen. Elastic moduli and ultrasonic attenuation of polycrystalline α-Mn from 4.2-300 $^{\circ}$K. *Phys. Rev.*, 165:357–359, 1968.

255. T. Ozaki, M. Aoki, and D. G. Pettifor. Block bond-order potential as a convergent moments-based method. *Phys. Rev. B*, 61:7972–7988, 2000.

256. E. Walker and P. Bujard. Anomalous temperature behaviour of the shear elastic constant C44 in tantalum. *Solid State Comm.*, 34(8):691 – 693, 1980.

257. Y. Ohta and M. Shimizu. Influence of shear strains on the electronic structure of vanadium. *J. Phys. F*, 13(4):761, 1983.

258. Lars Fast, J. M. Wills, Börje Johansson, and O. Eriksson. Elastic constants of hexagonal transition metals: Theory. *Phys. Rev. B*, 51(24):17431, 1995.

259. M. J. Gillan. Calculation of the vacancy formation energy in aluminium. *J. Phys. Condens. Matt.*, 1(4):689, 1989.

260. P. A. Korzhavyi, A. V. Ruban, J. Odqvist, J.-O. Nilsson, and B. Johansson. Electronic structure and effective chemical and magnetic exchange interactions in bcc Fe-Cr alloys. *Phys. Rev. B*, 79(5):054202, 2009.

261. G.P. Tiwari and R.V. Patil. A correlation between vacancy formation energy and cohesive energy. *Scripta Metall.*, 9(8):833 – 836, 1975.

262. Guoqiang Liu, D. Nguyen-Manh, Bang-Gui Liu, and D. G. Pettifor. Magnetic properties of point defects in iron within the tight-binding-bond stoner model. *Phys. Rev. B*, 71(17):174115, 2005.

263. Preetma Soin, AP Horsfield, and D Nguyen-Manh. Efficient self-consistency for magnetic tight binding. *Computer Physics Communications*, 182(6):1350–1360, 2011.

264. M. Mrovec, R. Gröger, A. G. Bailey, D. Nguyen-Manh, C. Elsässer, and V. Vitek. Bond-order potential for simulations of extended defects in tungsten. *Phys. Rev. B*, 75(10):104119, 2007.

265. M. Aoki, D. Nguyen-Manh, D. G. Pettifor, and V. Vitek. Atom-based bond-order potentials for modelling mechanical properties of metals. *Prog. Mater. Sci.*, 52(2-3):154 – 195, 2007.

266. F. Willaime, A. Satta, M. Nastar, and O. Le Bacq. Electronic structure calculations of vacancy parameters in transition metals: Impact on the bcc self-diffusion anomaly. *Inter. J. Quant. Chem.*, 77(6):927–939, 2000.

267. Georg K H Madsen, Eunan J McEniry, and Ralf Drautz. Optimized orthogonal tight-binding basis: Application to iron. *Phys. Rev. B*, 83(18):184119, 2011.

268. G. Y. Guo and H. H. Wang. Calculated elastic constants and electronic and

magnetic properties of bcc, fcc, and hcp cr crystals and thin films. *Phys. Rev. B*, 62(8):5136–5143, 2000.

269. J. A. Rayne and B. S. Chandrasekhar. Elastic constants of iron from 4.2 to 300 K. *Phys. Rev.*, 122(6):1714, 1961.

270. L. De Schepper, D. Segers, G. Knuyt, L. Dorikens-Vanpraet, M. Dorikens, Lambert Stals, and P. Moser. Determination of the ferromagnetic vacancy-formation enthalpy in α-iron by the positron method using the carbon-vacancy pair as a probe. *Physics Letters A*, 95(2):121–123, 1983.

271. G. Lucas and R. Schäublin. Vibrational contributions to the stability of point defects in bcc iron: A first-principles study. *Nuclear Instruments and Methods in Physics Research Section B: Beam Interactions with Materials and Atoms*, 267(18):3009–3012, 2009.

272. G. Kresse and D. Joubert. From ultrasoft pseudopotentials to the projector augmented-wave method. *Phys. Rev. B*, 59(3):1758, 1999.

273. S. Takaki, J. Fuss, H. Kuglers, U. Dedek, and H. Schultz. The resistivity recovery of high purity and carbon doped iron following low temperature electron irradiation. *Radiation effects*, 79(1-4):87–122, 1983.

274. C. Domain and C. S. Becquart. Ab initio calculations of defects in Fe and dilute Fe-Cu alloys. *Phys. Rev. B*, 65(2):024103, 2001.

275. Chu-Chun Fu, F. Willaime, and P. Ordejón. Stability and mobility of mono-and di-interstitials in α-Fe. *Phys. Rev. Lett.*, 92(17):175503, 2004.

276. David Vanderbilt. Soft self-consistent pseudopotentials in a generalized eigenvalue formalism. *Phys. Rev. B*, 41(11):7892, 1990.

277. D. Comtesse, H. C. Herper, A. Hucht, and P. Entel. A first-principles study aided with Monte Carlo simulations of carbon doped iron-manganese alloys. *The European Physical Journal B*, 85(10):1–13, 2012.

278. Kai Guo, Dieter Rau, Jörg von Appen, Yurii Prots, Walter Schnelle, Richard Dronskowski, Rainer Niewa, and Ulrich Schwarz. High pressure high-temperature behavior and magnetic properties of Fe_4N: experiment and theory. *High Pressure Research*, (ahead-of-print):1–13, 2013.

279. Max Hansen and K. Anderko. Constitution of binary alloys, metallurgy and metallurgical engineering series. *Mc Graw-Hill, New York*, 1958.

280. Sin Giu Kang, Hideya Onodera, Hisao Yamamoto, and Hiroshi Watanabe. Mössbauer effect study of bcc Fe-Mn alloys. *J. Phys. Soc. Japan*, 36:975, 1974.

281. Rainer Kubitz and Frederick Henry Hayes. Enthalpies of mixing in the iron-manganese system by direct reaction calorimetry. *Monatshefte für Chemie/Chemical Monthly*, 118(1):31–41, 1987.

282. M. Cankurtaran, G. A. Saunders, P. Ray, Q. Wang, U. Kawald, J. Pelzl, and H. Bach. Relationship of the elastic and nonlinear acoustic properties of the antiferromagnetic fcc $Fe_{60}Mn_{40}$ single-crystal alloy to Invar behavior. *Phys. Rev. B*, 47(6):3161, 1993.

283. Denis Music, Tetsuya Takahashi, Levente Vitos, Christian Asker, Igor A Abrikosov, and Jochen M Schneider. Elastic properties of Fe-Mn random alloys studied by ab initio calculations. *Applied Physics Letters*, 91(19):191904–191904, 2007.

284. NM Rosengaard and Hans Lomholt Skriver. Calculated stacking-fault energies of elemental metals. *Phys. Rev. B*, 47(19):12865, 1993.